KAUNAS UNIVERSITY OF TECHNOLOGY

VIKTORIJA MIMAITĖ

THEORETICAL AND EXPERIMENTAL INVESTIGATION OF CARBAZOLE- AND TRIPHENYLAMINE-BASED COMPOUNDS FOR OPTOELECTRONIC DEVICES

Doctoral dissertation
Technological Sciences, Materials Engineering (08T)

2016, Kaunas

UDK 547.759+547.551.2+621.315.592](043.3)

Doctoral dissertation was prepared in Kaunas University of Technology, Faculty of Chemical Technology, Department of Polymer Chemistry and Technology during the period of 2011-2016. The studies were supported by Research Council of Lithuania.

Scientific Supervisor:

Prof. Dr. Habil. Juozas Vidas GRAŽULEVIČIUS (Kaunas University of Technology, Technological Sciences, Materials Engineering 08T).

Scientific Advisors:

Dr. Jolita OSTRAUSKAITĖ (Kaunas University of Technology, Physical Sciences, Chemistry 03P);
Dr. Gjergji SINI (University of Cergy Pontoise, Physical Sciences, Chemistry 03P).

Doctoral dissertation has been published in:
http://ktu.edu

Editor:

Gavin James Grant Stewart

ISBN 978-609-02-1224-0

KAUNO TECHNOLOGIJOS UNIVERSITETAS

VIKTORIJA MIMAITĖ

KARBAZOLO IR TRIFENILAMINO DARINIŲ, SKIRTŲ OPTOELEKTRONIKOS PRIETAISAMS, EKSPERIMENTINIS IR TEORINIS TYRIMAS

Daktaro disertacija
Technologijos mokslai, Medžiagų inžinerija (08T)

2016, Kaunas

UDK 547.759+547.551.2+621.315.592](043.3)

Disertacija rengta 2011-2016 metais Kauno technologijos universiteto, Cheminės technologijos fakultete, Polimerų chemijos ir technologijos katedroje. Mokslinius tyrimus rėmė Lietuvos mokslo taryba.

Mokslinis vadovas:

Prof. habil. dr. Juozas Vidas GRAŽULEVIČIUS (Kauno technologijos universitetas, Technologijos mokslai, Medžiagų inžinerija 08T).

Moksliniai konsultantai:

Dr. Jolita OSTRAUSKAITĖ (Kauno technologijos universitetas, Fiziniai mokslai, Chemija 03P);
Dr. Gjergji SINI (Sergi Pontuaz universitetas, Fiziniai mokslai, Chemija 03P).

Interneto svetainės, kurioje skelbiama disertacija, adresas:
http://ktu.edu

Redagavo:

Gavin James Grant Stewart

ISBN 978-609-02-1224-0

List of Abbreviations

α	static isotropic polarizability
σ	energetic disorder parameter
σ_{dip}	dipole component
σ_{vdW}	van der Waals component
$\Delta\varepsilon_{HOMO}$	width of HOMO energy
ΔE_{ST}	energy gap between singlet and triplet excited states
λ	reorganization energy
λ_{ab}	band of absorption
λ_{ex}	excitation wavelength
λ_{fl}	maximum band of fluorescence emission
μ	charge carrier mobility
Bphen	4,7-diphenyl-1,10-phenanthroline
^{13}C NMR	carbon nuclear magnetic resonance
CV	cyclic voltamperometry
d	doublet
dd	double doublet
DFT	density functional theory
DSC	differential scanning calorimetry
DSSC	dye sensitized solar cell
EA_{CV}	electron affinity estimated by cyclic voltamperometry
E_g^{opt}	optical band gap
EL	electroluminescence
E_T	triplet energy
ETL	electron transporting layer
FIrpic	bis[2-(4,6-difluorophenyl)pyridinato-C^2,*N*](picolinato) iridium(III)
^{1}H NMR	proton nuclear magnetic resonance
HOMO	highest occupied molecular orbital
HTL	hole transporting layer
HTM	hole transporting material
ICT	intramolecular charge transfer
IE	interaction energy
IP	ionization potential calculated theoretical
IP_{CV}	ionization potential estimated by cyclic voltamperometry
IP_{PE}	ionization potential estimated by electron photoemission technique
$Ir(ppy)_3$	tris[2-phenylpyridinato-C^2,N]iridium(III)
ITO	indium tin oxide
J_{sc}	photocurrent density
LiTFSI	bis(trifluoromethane)sulfonimide lithium salt
LUMO	lowest unoccupied molecular orbital
m-MTDATA	4,4′,4″-tris[phenyl(*m*-tolyl)amino]triphenylamine

NPB	*N*,*N*′-di(1-naphthyl)-*N*,*N*′-diphenyl-(1,1′-biphenyl)-4,4′-diamine
$Os(bpftz)_2(PPh_2Me)_2$	osmium(II) bis[3-(trifluoromethyl)-5-(4-tert-butylpyridyl)-1,2,4-triazolate] diphenylmethylphosphine
$(PBi)_2Ir(acac)$	bis(2,*N*-diphenylbenzimidazolito) iridium(III) acetylacetonate
$(PPy)_2Ir(acac)$	bis(2-phenylpyridinato)iridium(III) acetylacetonate
PHOLED	phosphorescent organic light-emitting diode
s	singlet
SOMO	singly occupied molecular orbital
spiro-MeOTAD	2,2′,7,7′-tetrakis(*N*,*N*-di-*p*-methoxyphenylamine)-9,9′-spirobifluorene
t	triplet
TAPC	4,4′-cyclohexylidenebis[*N*,*N*-bis(4-methylphenyl) benzenamine]
TAS	transient absorption spectroscopy
TCTA	tris(4-carbazoyl-9-ylphenyl)amine
TDDFT	time dependent density functional theory
T_D	thermal destruction temperature
TiO_2	titanium (IV) oxide
T_g	glass transition temperature
TGA	thermogravimetric analysis
T_m	melting point
TOF	time of flight technique
UV	ultraviolet
vis	visible
V_{oc}	open-circuit photovoltage
V_{on}	turn-on voltage

Contents

1. INTRODUCTION

Organic optoelectronics is a rapidly developing research field including chemistry, physics, materials science and engineering. Optoelectronic devices, such as organic light emitting diodes (OLEDs) and organic photovoltaic cells (OPVs), have attracted the attention of many chemistry laboratories and industries due to their application potential in large area displays, lightning, and generation of green energy. OLED is one of most promising technology for flat panel displays and for lightning applications has entered into commercial uses. OPV has been interesting as a new type of energy source because of its low cost, simple manufacturing and large area capability. Despite much research, there are still scientific and technical problems remaining to be solved in organic optoelectronic devices. OLED requires to improve the power efficiency and device stability. Comparing with solar cells made from inorganic semiconductors, OPV needs improvement in power conversion efficiency, absorption wavelength scale and in the lifetime of device.

The subject of this work is the design, synthesis, and characterization of new charge transporting organic materials for dye sensitized solar cells (DSSCs) and phosphorescent organic light-emitting diodes (PHOLEDs). DSSC works in a wide range of light conditions without suffering from angular dependence of sunlight. It can be produced on a thin and flexible substrate. Therefore, DSSC is used for indoor and portable applications, starting out with chargers and wireless solar keyboards. This solar cell incorporated into the bigger installations is utilized in steel roofing, facades or semi-transparent windows. PHOLED exhibits higher efficiencies than fluorescent OLED. It is being investigated for displays and lightning panels which can be integrated into paper, wallpapers, clothing or other flexible surfaces.

Various electroactive materials have been designed over the years that transport holes and/or electrons. The derivatives of triphenylamine and carbazole received great interest because of their excellent charge transporting ability and unique optical properties. These compounds play important role in the development of new organic semiconductors. The incorporation of organic moieties into the triphenylamine and carbazole molecules may allow to obtain compounds with appropriate properties. In addition, the investigation of organic semiconductor families with the certain structural differences can provide information on structure-properties relationship, which is important for the optimization of optoelectronic devices.

The main aims of this work was synthesis and investigation of carbazole- and triphenylamine-based low-molar-mass organic semiconductors for optoelectronic devices.

The tasks proposed for the achievement of the above stated aim:

- Synthesis of carbazole derivatives with cyano groups as dyes for dye sensitized solar cells.
- Synthesis of carbazole derivatives having imidazole fragments.

- Synthesis of triphenylamine-based derivatives as hole transporting materials.
- Investigation of the properties of the synthesized compounds by experimental and computational methods.
- Estimation of the applicability of the synthesized materials in the structures of optoelectronic devices.

The main statements of doctoral thesis:

- The conjugated π-linker between carbazole and cyano units improve the performance of the derivatives of carbazole containing cyano groups in dye sensitized solar cells.
- Derivatives combining carbazole and imidazole in a donor-acceptor architecture can exhibit bipolar charge transport.
- Triphenylamine-based hydrazones and triphenylamine-twin compounds are capable of glass formation and demonstrate good hole-transporting properties.
- Formation of hydrogen bonds improve hole mobility of the methoxy and methyl substituted triphenylamine-twin compounds.

Scientific novelty of the work. A series of new structures organic semiconductors belonging to the families of carbazole and triphenylamine derivatives were designed. New materials were synthesized, characterized and their thermal, photophysical, electrochemical and photoelectrical properties were studied. Based on computational chemistry methods the interpretation of the experimental studies of structure-properties relationship of carbazole- and triphenylamine-based organic semiconductors is presented.

Practical value of the work. The complex investigation of the properties of the synthesized materials has revealed that they can be applied in organic optoelectronic devices such as solar cells and organic light-emitting diodes. The newly synthesized triphenylamine-based hydrazone was used as hole-transporting glass-forming material for the preparation of dye sensitized solar cell by melt process. New carbazole-imidazole derivatives were used as host materials for phosphorescent light emitting diodes.

Personal input of the author. The author has designed, synthesized, purified and characterized the compounds described in Chapter 4. The theoretical calculations of compounds were performed in collaboration with scientific advisor Gjergji Sini from Cergy-Pontoise University. The author also performed infrared spectroscopy, absorption, cyclic voltammetry, melting point measurements with help from corresponding technicians. Structure analysis of the obtained compounds, their thermal properties, charge mobility, ionization potential measurements and investigation of phosphorescent light emitting diodes were performed in collaboration with the colleagues from Department of Polymer Chemistry and Technology, Kaunas University of Technology. Fabrication and characterization of dye sensitized solar cells were done by Mindaugas Juozapavičius and other scientists from Imperial College London.

2. LITERATURE REVIEW

2.1. Low-molar-mass organic semiconductors

Organic semiconductors, known also as charge-transporting materials are organic materials made of π-conjugated bonds which allow charges to move via π-electron cloud overlaps. Charge-transporting materials can be *p*-type (hole transporting), *n*-type (electron transporting) and bipolar (transporting both holes and electrons). [1] Charge carriers of organic materials correspond to the cation and anion radicals. It has generally been accepted that charge transport in organic disordered systems takes place by a hopping process. [2] That is, electrons are sequentially transferred from the anion radical to the neutral molecule through the lowest unoccupied molecular orbital (LUMO) for electron transport, and electrons are sequentially transferred from neutral molecule to its cation radical through the highest occupied molecular orbital (HOMO) for hole transport. [3,4]

Low-molar-mass organic semiconductors are materials with well-defined molecular structures and molecular weights. The compounds with stable solid amorphous phase above room temperature are called molecular glasses or amorphous molecular materials. Amorphous molecular materials may exhibit isotropic properties as well as homogeneous properties. Their uniform, transparent amorphous thin films can be prepared by vapour deposition and spin-coating methods. [5,6]

2.2. Dye sensitized solar cells

The solar energy industry is one of the fastest growing industries because of the increasing demand for clean energy. Solar energy conversion into electrical energy is a major direction for solar technology development. DSSCs have attracted much attention in recent years due to their potential advantages of low cost, ease of production, flexibility and transparency as compared with crystalline silicon solar cells. [7,8,9] Dye is a key component of the DSSC, being responsible for the capture of sunlight and generation of the electric charges. [10] The efficient metal free organic sensitizers are systems composed of donor and acceptor groups linked through π-conjugated spacer. The dyes in DSSCs require one or more chemical substituents that can act as an anchor, enabling the injection of electrons from the dye into the conduction band of the metal oxide. Usually, the acceptor group is used as an anchoring unit to ensure ultrafast electron injection. [11]

Typically, the DSSC consists of dye-sensitized metal oxide photoanode, counter electrode and electrolyte with I^-/I_3^- redox couple (**Scheme 1**). The dye is excited by absorbing the incoming photon and rapidly injects an electron into the conduction band of metal oxide. Then the electron goes through an external circuit and arrives at the counter electrode, where an I_3^- ion is reduced. Finally, the dye is regenerated by I^-. [12,13]

Most highly efficient DSSCs have been constructed with liquid electrolytes with the I^-/I_3^- redox couple and volatile organic solvents. However, the evaporation of toxic solvents and the leakage of liquid electrolytes limit their practical

application. One alternative to solve the sealing problem is the replacement of the liquid redox electrolyte by a solid state hole conductor. The hole conductors typically also contain additives of salts allowing for some ionic conductivity, which is important for local charge compensation. [14,15]

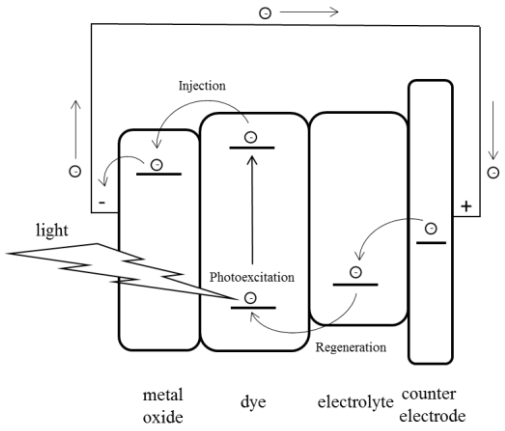

Scheme 1. Energy diagram for the electronic processes in the DSSC

Critical factors that influence performance of DSSC are energy levels of the device components. LUMO of the dye must be higher in energy than the metal oxide conduction band to ensure efficient electron injection. HOMO of dye must be lower than the redox potential of electrolyte to allow efficient regeneration of the oxidized dye. [16,17] Furthermore, the dye needs to improve light-harvesting ability, therefore, red-shift and broad UV-vis absorption spectrum is desired. [18]

2.2.1. Carbazole-based dyes for sensitized solar cells

The extension of π-linker is one of the viable tactics to improve the molar absorption coefficient and red-shift of the absorption peak, which is beneficial to light harvesting. The length of non-conjugated linkers has no significant effect on the physical properties of dyes. However, the characteristics of the DSSCs deteriorate with an increases of non-conjugated linker length. [19,20] The absorption spectra of compounds **Ia-d** illustrated that the thiophene ring is better than the benzene ring as π-linker in terms of improving the spectral extend in the visible light range. The thiophene linker ensures more efficient electronic communication between the indolo[3,2,1-jk]carbazole donor and the cyanoacrylic acid acceptor moieties. The photovoltaic conversion efficiencies of DSSCs based on the dyes were in the order of **Ib** > **Ia** > **Id** > **Ic**. Extension of conjugation by benzene ring has been found to deteriorate the characteristics of devices. The poor performance of DSSCs containing benzene rings could be attributed to the higher charge transfer resistance. The photovoltaic conversion efficiency of DSSC, without benzene units, reached 3.68%. [21]

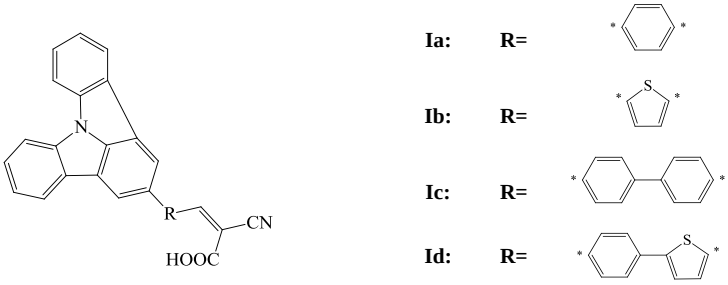

The thiophene linker is shown to be effective for the control of intramolecular charge separation and optical properties. [22] However, there are promising results due to the structural modification on the carbazole-based dye with benzene linker. Barpuzary et al. [23] reported the organic dye **II** containing phenylethene unit as π-linker. The synthesized D-π-A type compound provides intramolecular charge transfer from donor to acceptor site within the molecule. The device combination of one dimensional ZnO nanowires and dye achieved photovoltaic conversion efficiency up to 5.7% and 4.7% for cobalt- and iodide-based electrolytes, respectively.

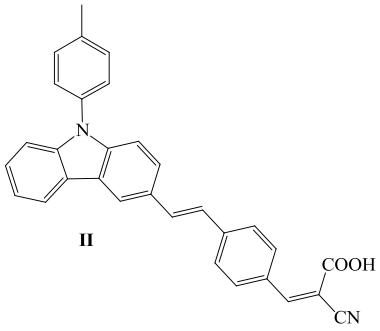

II

Dye aggregation on the TiO_2 surface generally is an undesired phenomenon in DSSC, leading in an unsuitable energetic position of the LUMO level of the dye. The aggregation results in poor electron injection from dye into the TiO_2. [24,25] Compared with the solution spectra, the absorption bands of the **IIIa** and **IIIb** dyes on the TiO_2 films were red shifted by 29 and 12 nm, respectively. **IIIb**, showing the smallest change of absorption spectrum, seemed to be more efficient in suppressing the formation of dye aggregates on the TiO_2 surface. Whereas the absorption band of the **IIIc** on the TiO_2 film was blue shifted by 31 nm, which is attributed to the formation of H-type aggregates or deprotonation of the carboxylic acid units. The three DSSCs composed of investigated dyes gave photovoltaic conversion efficiency higher than 3.2%, the DSSC with **IIIb** demonstrated the highest efficiency up to 3.8%. [26]

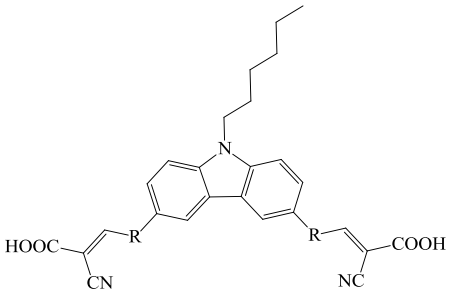

IIIa: **R=** 

IIIb: **R=** 

IIIc: **R=** 

Different link mode and substituent at N atom of the carbazole derivatives leads to the different absorption range and intensity. [27,28] **Va** bearing butyl group and **Vb** with phenyl ring compare with **IV** display the broader absorption spectrum and higher absorptivity. A significant twist of the carbazole moiety from the plane of the π-linker in **IV** can weaken the conjugation extension of the whole molecule and reduce the intramolecular charge transfer. The connection of π-linker at benzene ring instead of N atom of the carbazole unit favours improving the light harvesting and lowering the charge recombination. DSSC with **IV** provided the lowest photovoltaic parameters and exhibited conversion efficiency of 2.01%. Dyes **Va** and **Vb** with the larger conjugation system showed conversion efficiency of 4.47% and 4.72%, respectively. [29]

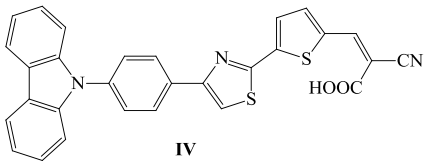

IV

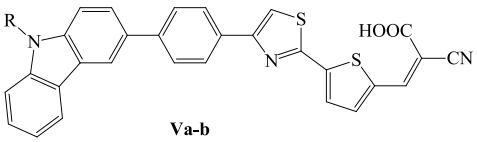

Va-b

Va: **R=** **C_4H_9**

Vb: **R=** 

Increased thiophene conjugation is found to positively shift the HOMO. [30] Dye structure in which HOMO is mainly located on the donor side while LUMO is mostly located on the acceptor group, causes a natural charge separation minimizing recombination rate and maintaining efficient electron injection from excited dye into the TiO_2. [31,32] Absorption spectra of compounds **VI-VIId** showed that the lower energy transition bands were progressively red-shifted and exhibited enhancement in the molar extinction coefficient on introduction of additional thiophene unit in the conjugation pathway. The theoretical calculations revealed good HOMO and LUMO separation of the compounds **VIIa-d**. HOMO was mainly contributed by carbazole fragments and LUMO was precisely located on the segment of thiophene cyanoacrylic acid. However, for the dye **VI**, HOMO and LUMO were found to be overlapping and suggested a poor charge transfer. The photovoltaic conversion efficiencies of the DSSCs based on the synthesized dyes **VI-VIId** are in range from 4.22% to 6.04%. The incorporation of *tert*-butyl groups in the dyes structure was

found to suppress the recombination of injected electrons which contributed to the increment in the photocurrent generation and open-circuit photovoltage. [33]

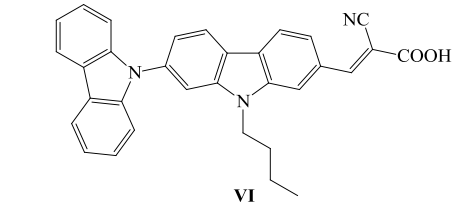

VI

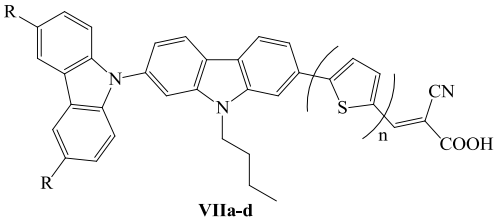

VIIa-d

VIIa: **R=H, n=1**
VIIb: **R=*t*-butyl, n=1**
VIIc: **R=H, n=2**
VIId: **R=*t*-butyl, n=2**

Dye **VIII** has a rigid/coplanar 5,7-dihydroindolo[2,3-b]carbazole core and two anchor groups attached to bithiophene bridges. The results of FT-IR spectroscopy clearly revealed that both carboxylic acid moieties in **VIII** were anchored on the TiO_2 surface. A computational approach indicated that HOMO of **VIII** /(TiO_2)70 was mainly populated on the electron-rich dyes core, whereas LUMO was localized on the (TiO_2)70 nanocluster. The efficient electron transfer from HOMO to LUMO lead to the successful development of DSSC with photovoltaic conversion efficiency of 6.02%. [34]

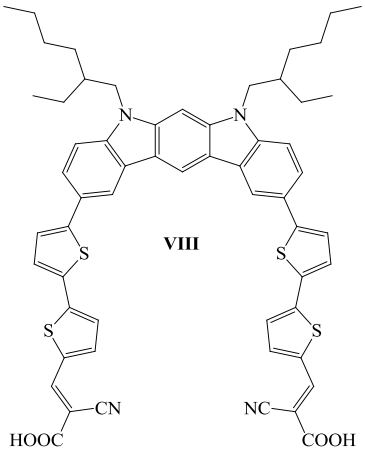

VIII

Gupta et al. [35] investigated the new dye-sensitizers in which carbazole and phenothiazine units were linked by an alkyl-chain and different anchoring groups were employed. The DSSCs sensitized by **VIIIa**, having cyanoacrylic acid moiety, and **VIIId**, bearing rhodanine acetic acid moiety, showed the best performances with power conversion efficiencies of 5.8% and 5.6%, respectively. The dye **VIIIc**,

bearing one carboxylic group, demonstrated an appreciable blue shift when it was adsorbed on the TiO_2 substrate. That is possibly associated to an unfavourable energy level alignment for electron injection, which determines low photocurrent and reduced efficiency (2.4%) of the device. The carbazole moiety in the dyes provided extra electron portion on the phenothiazine fragment, collecting photons and, through long-range energy transfer, redirecting the captured energy to the dye-sensitizer [36].

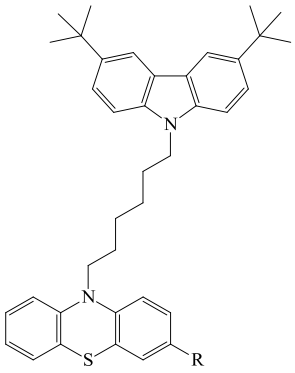

VIIIa: **R=** 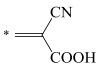

VIIIb: **R=** 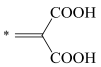

VIIIc: **R=** 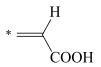

VIIId: **R=** 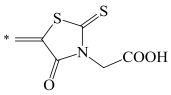

The rhodanine acetic acid acceptor has stronger electron-withdrawing nature than the cyanoacrylic acid. Therefore, the absorption and emission peaks of the dyes with rhodanine moieties are red-shifted compared to those of the compounds with cyanoacrylic acid moieties. [37,38] However, DSSC with **IXa** exhibited higher power conversion efficiency of 2.37% under AM1.5G solar illumination compared to DSSC having **IXb** as dye. The spectral measurements indicated that cyanoacrylic acid group adsorbed better on TiO_2 surface compared to rhodanine acetic acid moiety. In addition, rhodanine acetic acid showed a lower tendency to inject electrons from the LUMO to TiO_2 conduction band due to the presence of the methyl group. [39]

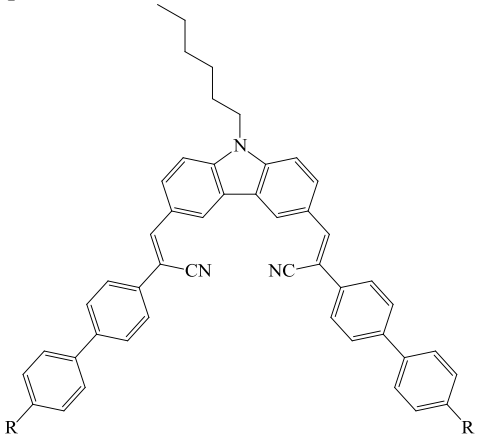

IXa: **R=** 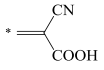

IXb: **R=** 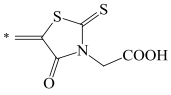

The efficient retardation of electron-hole recombination in DSSC can be achieved by the application of alkyl-chains attached to the dye-sensitizer, resulting in a significantly improved device performance. The alkyl-chains act as an electrically insulating barrier, thereby reducing interfacial charge recombination losses. [40] The influence on the number of hexyl-chains on the thiophene units of the dyes was investigated by Huang et al. [41]. Incorporation of hexyl-chains into the structure of the dye enhances the molar extinction coefficients of the absorption. Thus increasing the number of hexyl-chains in dye structure was highly effective in enhancing power conversion efficiency of the DSSCs, which arrange in the order **Xa** < **Xb** < **XIa** < **XIb** with the values of 3.59% < 4.54% < 5.15% < 5.51%.

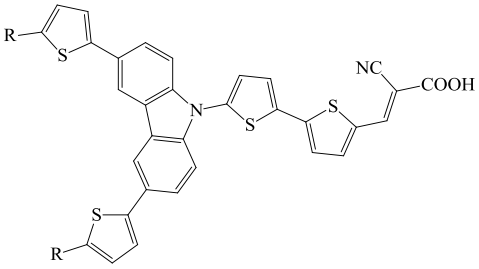

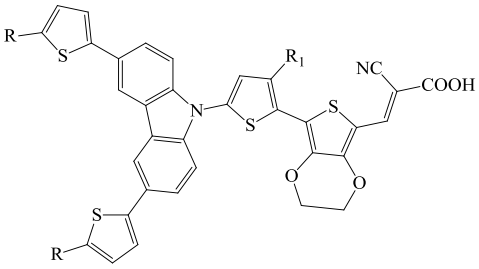

Xa: **R= H**
Xb: **R=hexyl**

XIa: **R=hexyl** **R_1=H**
XIb: **R= hexyl** **R_1=hexyl**

The length of the alkyl-chain did not affect the absorption and fluorescence emission spectra. However, the longer alkyl-chains decrease the aggregation on TiO_2 surface. The aggregation on the TiO_2 surface increases the intermolecular charge transfer between dye molecules and decreases the charge transfer from dye molecules to TiO_2 electrode. [42] The higher efficiency of **XIIb** containing DSSC (3.18%) compared to that containing **XIIa** (2.49%) can be attributed to higher electron injection yield and slower charge recombination rate due to longer alkyl-chain. [43]

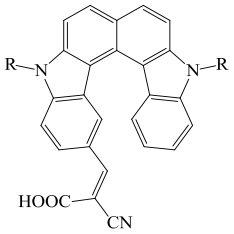

XIIa: **R= methyl**
XIIb: **R=octyl**

The introduction of alkyl-chain into dyes has a positive effect on the photon-to-current conversion efficiency. The higher conversion efficiency value means a higher electron transfer yield. [44] Maximum photon-to-current conversion efficiency values of the dyes are in the order of **XIIIa** > **XIIIb** > **XIIIc**. Moreover, photocurrent density of DSSCs increases with the increase of chain length. This

observation was explained by the self-assembling of alkyl-chains on TiO_2 and by longer distance between the TiO_2 and electrolyte. The alkyl-chains block the recapture of the photo injected electrons by I_3^-. A similar trend was also observed in power conversion efficiency of the DSSCs. DSSC based on **XIIIa** with the two different electrolytes demonstrated the highest conversion efficiencies of 6.68% and 6.02%. [45]

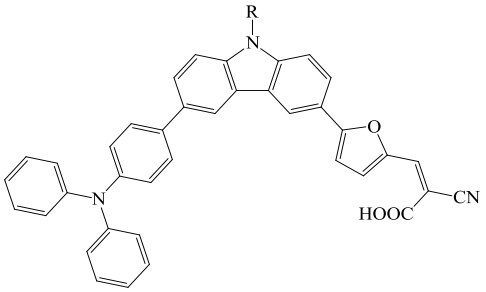

XIIIa: **R=octyl**
XIIIb: **R=hexyl**
XIIIc: **R=methylpentyl**

2.2.2. Hole-transporting triphenylamine derivatives for dye sensitized solar cells

Compared with inorganic, organic hole conductors possess the advantages of having plentiful sources, easy film formation and low cost. [46] The organic hole-transporting material (HTM) should be a transparent and form stable amorphous thin film, as crystallization will prevent effective pore filling and thereby reduce its thermal and photochemical stability as well as carrier mobility. [47] Triarylamine-based compounds, such as 2,2',7,7'-tetrakis(*N*,*N*-di-*p*-methoxyphenylamino)-9,9'-spirobifluorene (spiro-MeOTAD), are the most popular molecular hole-transporting materials used in solid state DSSCs. The devices made with spiro-MeOTAD show power conversion efficiency up to 4.5% and 7.2% for metal free- and cobalt-based dyes respectively, under standard solar conditions AM 1.5G illumination. [48,49,50]

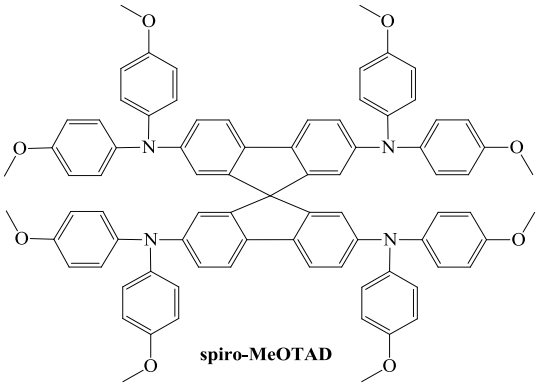

The molecular structure of spiro-OMeTAD based on the twisted center of the spiro-carbon significantly inhibits the intra- and intermolecular π-π conjugation, which results in a fairly low hole mobility. In addition, spiro-OMeTAD is limited of

infiltration into the mesoporous electrodes. [51,52] Higher solubility and higher hole mobility of HTM can outperforms the dominating spiro-OMeTAD in DSSC. **XIVa** and **XIVb** have similar functional groups and energy levels to spiro-OMeTAD, but differ in molecular size, solubility, T_g (glass transition temperature) and T_m (melting point). The DSSC fabricated with **XIVb** showed higher power conversion efficiency (2.3%) than that produced with spiro-OMeTAD (2.1%). The low performance of spiro-OMeTAD is explained to the low degree of pore filling. The higher solubility of **XIVa** and **XIVb** than that of spiro-OMeTAD leads to the higher solution concentration, which can increase the filling fraction. T_g and T_m of spiro-OMeTAD are 125 °C and 248 °C, respectively. **XIVa** and **XIVb** exhibited two times lower T_g and T_m compared that with spiro-OMeTAD. Heating at temperatures above T_g, should increase pore filling and can lead to the better performance of DSSCs. [53]

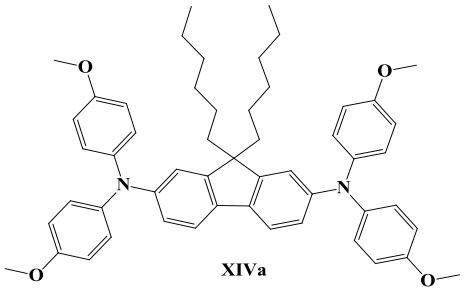

XIVa

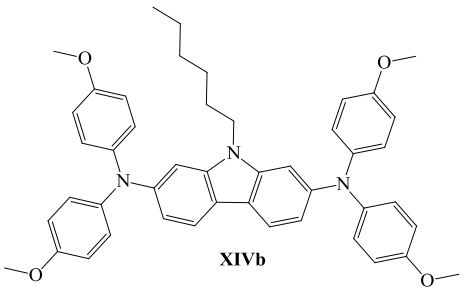

XIVb

Additives maximize the performance and the long-term stability of DSSCs. [54] The DSSC with **XV** provides conversion efficiency of 1.1%, but after light soaking treatment with bis(trifluoromethane)sulfonimide lithium salt (LiTFSI) the efficiency of the device is increased more than 4 times (4.9%). The power conversion efficiency remains impressively stable after the initial light soaking treatment with only 0.2% drop over 580 h at room temperature in dark. The light soaking effect is attributed to the Li^+ ion migration by the electric field built in the solar cell during illumination as driving force. [55]

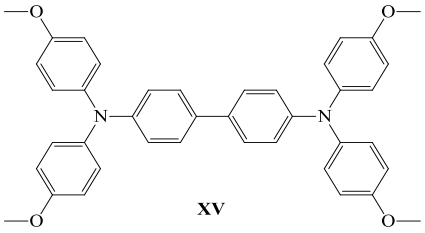

XV

Planells et al. [56] reported on the derivatives of triphenylamine **XVIa-d** with different electron donating groups. These molecules are comprised of two triphenylamine moieties bridged with a diethynyl group. The oxidation potentials of the compounds were shifted to less positive potentials by increasing the electron donating ability of the groups (-H < -Me < -SMe < -OMe). The compounds **XVIa-d**

showed charge mobilities by ca. two orders of magnitude lower than spiro-OMeTAD. However, the conductivity values after the addition of *p*-dopant for the HTM infiltrated in a mesoporous TiO_2 film, were found to be in the same range. The DSSCs employing organic dye showed increase of power conversion efficiency as the oxidation potentials of HTM decreased. The efficiency of the devices made fabricated using **XVIa**, **XVIb** and **XVId** are 0.15%, 0.34% and 1.16%, respectively.

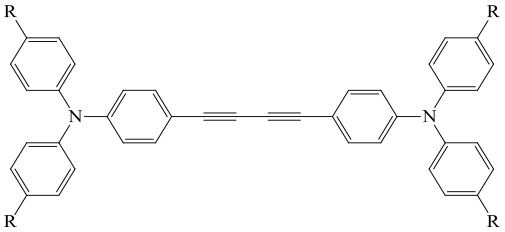

XVIa: **R=H**
XVIb: **R=Me**
XVIc: **R=SMe**
XVId: **R=OMe**

Solvent evaporation acts as a driving force to aid HTM infiltration in nanoporous film of semiconductor. However, solvent evaporation and fully drying of the film results in voids or air in place of the solvent. [57] Organic semiconductor in the liquid phase may offer the ideal solution, enabling infiltration without solvent uses. The first application of organic semiconductor in the liquid phase was demonstrated by Snaith et al. [58]. They used HTM **XVII** with 2-methoxy-ethoxy groups for the DSSC fabrication. The device based on this concept exhibited up to 3% power conversion efficiency under simulated sunlight and quantum efficiency exceed 50%.

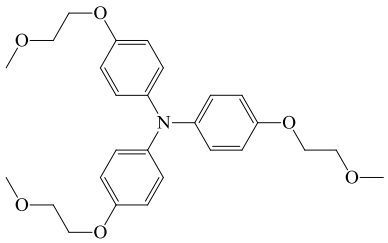

XVII

The DSSC made with triphenylamine-based compound **XVIIIa** containing silyl ethers groups showed high photovoltage (0.9 V) due to large ionization potential of compound and the power conversion efficiency up to 1.9% was obtained using ruthenium based dye. When the analogous **XVIIIb** was used no photo conversion was observed. The authors suggest that the presence of bulky triisopropylsilyl ether groups may afford appropriate spacing between the sensitized surface and the HTM to give rise to good regeneration while slowing down recombination. [59]

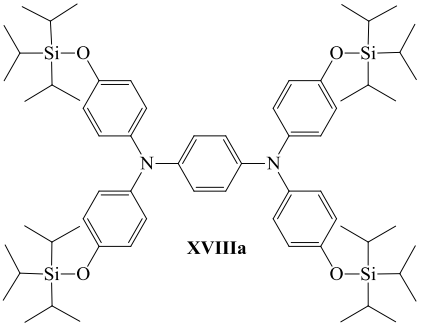

XVIIIa

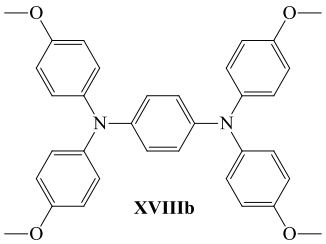

XVIIIb

Zhou et al. [60] used cross-linkable triphenylamine-based organosilane as HTM for DSSC. The low-molecular-weight and highly soluble **XIX** can penetrate deep into the mesoporous TiO_2 filling up the empty space. The Si-Cl bonds are very stable when stored under an inert atmosphere but they are readily hydrolysed in the presence of moisture. The reaction of $SiCl_3$ groups with OH covered metal oxide surfaces which resulted in chemisorption to form strong covalent metal-O-Si bonds, whereas hydrolysis enabled cross-linking via the formation of very strong Si-O-Si bonds. The covalently cross-linked **XIX** film could efficiently transport holes from the oxidized dye to the anode. The DSSC fabricated using **XIX** demonstrated the power conversion efficiency of 0.64%. The efficiency of DSSC with additives increased to 2.05%, because HOMO level of **XIX** film with additives is more favourable for hole extraction from the dye.

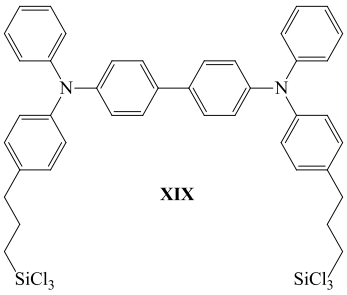

XIX

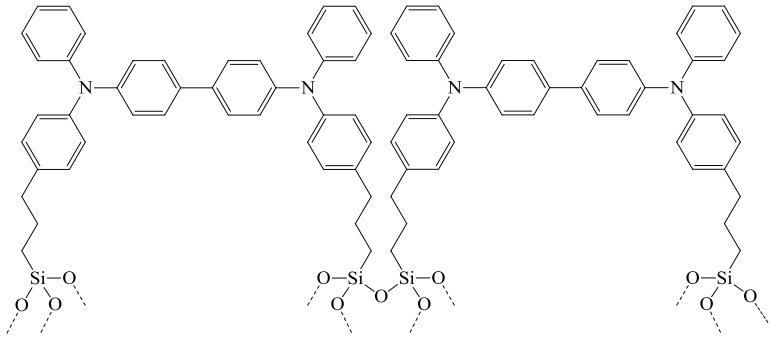

cross-linked XIX

2.3. Organic semiconductors for phosphorescent light emitting diodes

Organic light emitting diodes (OLEDs) are strong candidates for integration with flexible electronics to achieve flexible color displays. They are also widely used for organic lightning. [61] Generally, electrons and holes are injected from the respective electrodes move through charge injection/transport layers into the emitter layer of the device. There electrons and holes recombine and form singlet and triplet excitons. Compared with fluorescent OLEDs, which use only singlet excitons for light emission, phosphorescent PHOLEDs can utilize both singlet and triplet excitons for light emission, which increases the quantum efficiency of the devices. Theoretically, the quantum efficiency of PHOLEDs can be four times higher than that of OLEDs. [62] Phosphorescent guest emitters normally have to be doped in a suitable charge transporting host matrix due to their typically poor carrier mobility. [63] The system host/guest can lead to emitter emission in three routes (**Scheme 2**): (i) the singlet excitons formed in the host can be transferred to guest singlet excited-state and converted to triplet excitons by efficient intersystem crossing; (ii) the triplet excitons formed in the host can be forwarded to guest triplet excited-state; (iii) the holes and electrons can directly recombine in guest molecules and generated triplet excitons. The relaxation of emitter molecule from triplet exited-state to neutral ground-state leads to phosphoresce. [64,65]

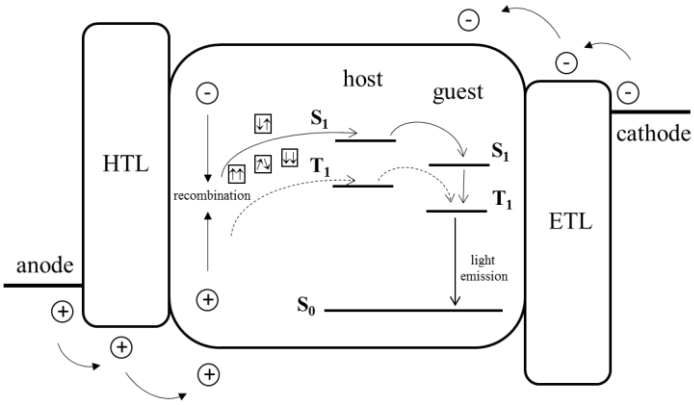

Scheme 2. Mechanisms of emission in host/guest system of PHOLED

To maximize PHOLED efficiency, a high performance host molecule needs to follow certain criteria: (i) the triplet energy of the host molecule should be higher than the corresponding energy of the guest emitter to prevent exothermic reverse energy transfer and thus effectively confine triplet excitons within the emitting layer; [66] (ii) the balanced charge injection from neighboring layers should occur; (iii) HOMO and LUMO levels of the host molecules should be appropriately aligned with the hole- and electron-transporting layers to reduce the driving voltage for charge injection. [67]

2.3.1. Carbazole-based hosts for phosphorescent light emitting diodes

Bipolar host materials can enable to achieve balanced charge injection/transport in PHOLEDs and consequently obtain excellent device performance. [68,69,70] The different linkages modes tune photophysical and electrochemical properties, and consequently modulate charge mobility and energy levels of bipolar materials. [71] The values of hole and electron mobility for **XXa** and **XXb** are very close and indicate that the bipolar charge-transport properties are balanced. In contrast, for **XXc** the hole mobility is by an order of magnitude higher than the electron mobility. The triplet energies determined from the phosphorescence spectra at 77 K follow the trend: **XXa** (2.62 eV) > **XXb** (2.58 eV) > **XXc** (2.48 eV). The PHOLEDs were fabricated by using a green emitter of $Ir(ppy)_3$ as the guest. The efficiencies of the optimized devices with different host materials were in the same order as triplet energies. The device based on **XXa** achieved the best characteristics with current efficiency of 92.3 cd/A, power efficiency of 78.8 lm/W and external quantum efficiency of 26.1%. The reasons why the **XXa** based device showed the best efficiencies can be elucidated to the higher triplet energy and higher charge mobility. The high triplet energy could efficiently suppress adverse energy back-transfer from the guest to the host, consequently resulting in good performances of the device. [72]

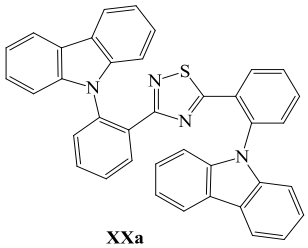

XXa

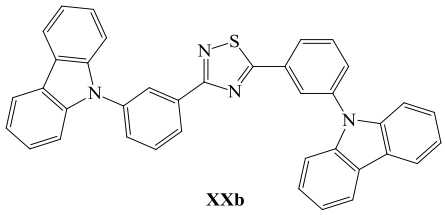

XXb

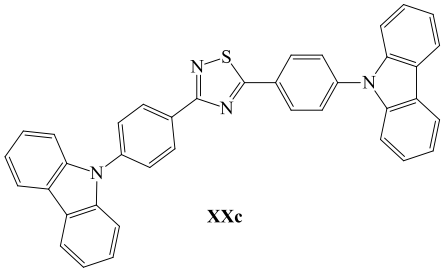

XXc

Cho et al. [73] synthesized **XXIa** and **XXIb**, containing pyrido[2,3-b]indole at the different positions of pyridine linking unit. The HOMO of the two host molecules was found to be localized on the carbazole unit and the LUMO was found to be distributed over the pyrido[2,3-b]indole fragment, according to DFT calculations. In particular, the **XXIb** host exhibited better separation of orbital distribution in the HOMO and LUMO states, compared with the **XXIa** host. Although the substitution position of pyrido[2,3-b]indole on the pyridine linking unit was different, the two host molecules demonstrated almost identical

photophysical, thermal and electrochemical properties. The identical triplet energies were determined to be 2.92 eV for **XXIa** and **XXIb**. The external quantum efficiencies values at the practically useful luminance of 1000 cd/m^2 for the **XXIa**- and **XXIb**-based devices were 21.0% and 23.7%, respectively.

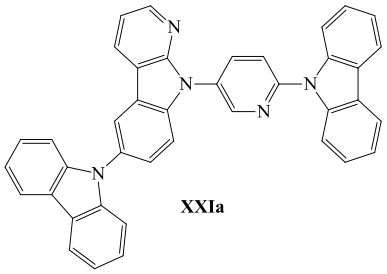

XXIa

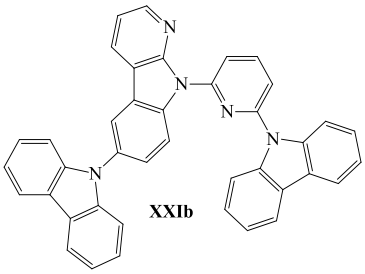

XXIb

The benzimidazole fragment in bipolar host materials is usually used as a functional unit that facilitates electron injection and transport. [74] The bipolar transporting charge properties of **XXII** were confirmed using TOF technique. The hole mobility was measured to be $4.32 \cdot 10^5$ cm^2/V, which was close to the value of the electron mobility $6.12 \cdot 10^5$ cm^2/V, under an electric field of $5.0 \cdot 10^5$ V/cm. The spatial distribution of electron density of HOMO was mainly localized on the carbazole unit and the LUMO orbital was dispersed in the benzimidazole moiety. The separation of HOMO and LUMO can be rationalized by the broken conjugation at the nitrogen atom of benzimidazole and the phenyl ring. The triplet energy of **XXII** was found to be 2.78 eV, obtained from the first phosphorescent emission peak. Compound **XXII** was evaluated as the host material for blue PHOLED. The device showed high quantum efficiency of 26.2%, power efficiency of 52.2 lm/W and current efficiency of 54.5 cd/A. [75]

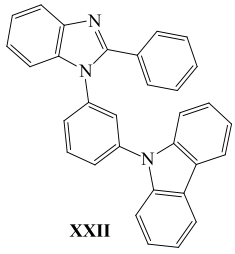

XXII

The extension of conjugation of the host molecule can be minimized, altering the linkage group between two entities. [76] Substitutions at C-2 and C-2' positions of biphenyl moiety caused twisting of the phenyl rings. Due to this electronic decoupling, the conjugation length in the molecules was limited which caused an increase of the triplet energy to 2.95–2.97 eV for **XXIIIa-e**. The introduction of the substituents at C-3 and C-6 positions of the carbazole units lead to fully reversible oxidation and electrochemical stability. Compounds formed glasses with T_g ranging from 94 °C to 121 °C. Derivatives **XXIIIb** and **XXIIIe** bearing 3,6-dimethylcarbazole unit showed T_g of 121 C° and 119 C°, respectively. [77]

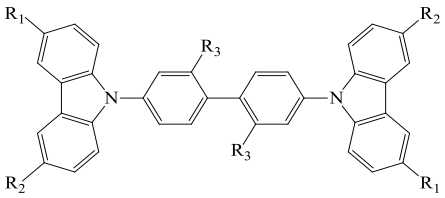

	XXIIIa	XXIIIb	XXIIIc	XXIIId	XXIIIe
R_1	CH_3	CH_3	H	CH_3	CH_3
R_2	H	CH_3	H	H	CH_3
R_3	CH_3	CH_3	CF_3	CF_3	CF_3

Wagner et al. [78] synthesized and studied bipolar host materials **XXIVa** and **XXIVb** in which hole transporting carbazole and electron transporting triazine moiety were linked by a fully aromatic but non-conjugated biphenyl linker. The theoretical calculations demonstrated that in both compounds the central triazine ring formed an approximately planar system with two adjacent carbazole moieties and one phenyl ring. Two phenyl rings in biphenyl unit of compounds **XXIVa** and **XXIVb** were twisted, respectively by 35° and 90°. Therefore, the HOMO was localized on the third separated by torsion carbazole fragment and the LUMO was localized on the triazine ring. The additional twist at the biphenyl linker in **XXIVb**, which was achieved by methyl-substitutions, lead to a higher triplet energy of 2.81 eV compared to 2.70 eV observed for **XXIVa**. These molecules were used as host materials for blue phosphorescent emitter FIrpic in PHOLED structures. The device with **XXIVa** exhibited a maximum external quantum efficiency of 6.2% and a power efficiency of 4.6 lm/W, whereas the device with **XXIVb** reached 7.0% and 6.3 lm/W, respectively.

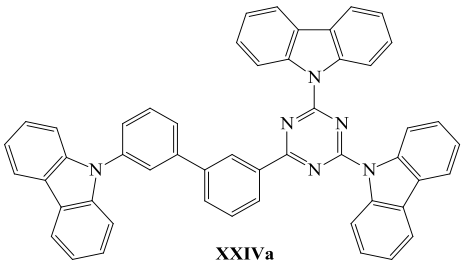

XXIVa

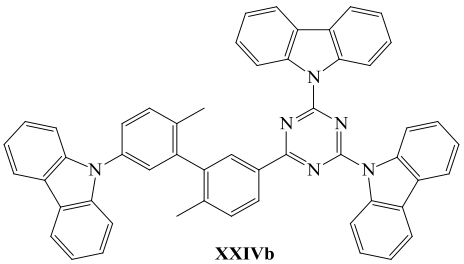

XXIVb

The HOMO of **XXVa** and **XXVb** was localized on the carbazole fragment, whereas the LUMO was dispersed over electron deficient benzofuro[2,3-b]pyridine unit. The phenyl linkage did not extend the conjugation in **XXVb**. For this reason, the triplet energies of **XXVa** and **XXVb** estimated from the first phosphorescent emission peaks were almost identical, i.e. 2.90 eV and 2.91 eV, respectively. **XXVb** showed higher electron current density than hole current density, while **XXVa** exhibited the similar hole and electron current densities. This observation indicates

that the incorporation of linkers between hole transporting and electron transporting moieties is effective to improve the electron transport properties of the host materials. The blue PHOLED having **XXVb** demonstrated higher quantum efficiency (24.3%) than the device with **XXVa** (19.1%). In the case of the device containing **XXVa** the balance of holes and electrons in the emitting layer was disrupted by the electron trapping effect of FIrpic. Therefore, the hole density in the emitting layer was higher than the electron density. This resulted in lower quantum efficiency. The electron current density in the emissive layer of the device containing **XXVb** was higher than hole current density, but it was reduced by the electron trapping of FIrpic, which lead to the better charge balance in the emitting layer. [79]

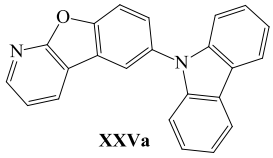

XXVa

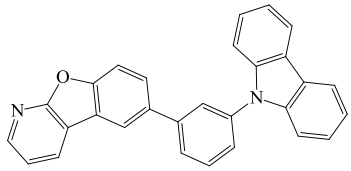

XXVb

The LUMO of the compounds **XXVIa-e** synthesized by Sun et al. [80] was localized on the carbazole units, while the HOMO of **XXVIa**, **XXVIb** and **XXVId** cover the whole molecular structure, and the HOMO of **XXVIc** and **XXVIe** was localized on the phenoxazine and phenothiazine-S,S-dioxide units. Obvious intramolecular charge transfer in compounds **XXVIc** and **XXVIe** might exists**,** and these compounds showed relatively high triplet energy of 2.57 eV and 2.79 eV, respectively. The green PHOLEDs were fabricated using **XXVIc** as host material and $Ir(ppy)_3$ as guest. The best device achieved maximum luminance of 10270 cd/m^2, current efficiency of 34.8 cd/A and power efficiency of 26.0 lm/W.

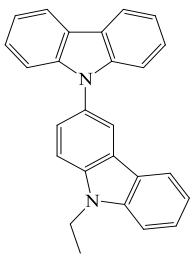

XXVIa

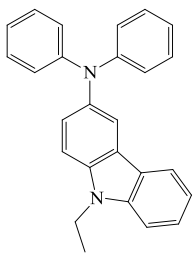

XXVIb

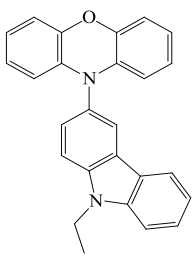

XXVIc

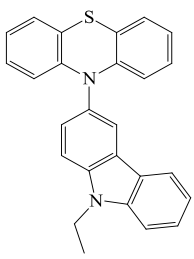

XXVId

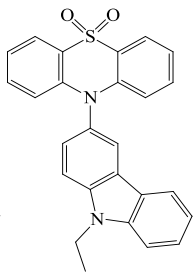

XXVIe

Investigations of coupling between carbazole units in the 3(6),9'-linked topology revealed that hosts exhibit large values of triplet energies and morphological stability of the glasses. [81] The coupling of carbazole units via C-N linkages provides rise to an ambipolar character compared that with the derivatives linked via C-C. [82] Compounds **XXVIIa-e** showed high T_D over 300°. Compounds **XXVIId** and **XXVIIe** had higher T_g values than dimers **XXVIIa-c**, presumably

because of their larger molecular weight. **XXVIIe** showed the most impressive and the highest T_g of 150 °C. Compounds **XXVIIa** and **XXVIIc** showed nearly the same triplet energies in the range of 2.98-3.00 eV and slightly lower values of 2.92-2.94 eV were recorded for **XXVIId-e**. 3,3′-Linked **XXVIIb**, having more extended π-conjugation, showed a significant red-shift in absorption, fluorescence and phosphorescence and consequently substantially lower triplet energy of 2.77 eV. PHOLEDs with these hosts exhibited turn-on voltages of 2.8-3.6 V, high external quantum efficiencies of 12-15% and maximum power efficiencies of 13-28 lm/W. The device fabricated using **XXVIId** as the host exhibited the best overall performance, including a turn-on voltage of 2.8 V, maximum external quantum efficiency of 14.7% and a maximum power efficiency of 28.4 lm/W. [83]

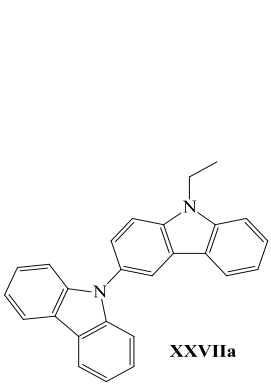

XXVIIa

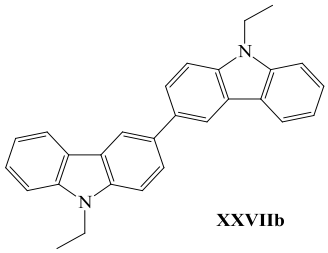

XXVIIb

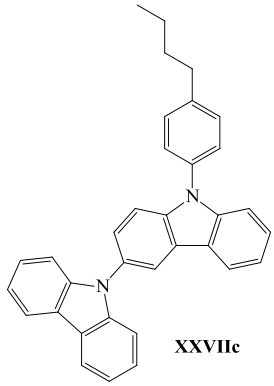

XXVIIc

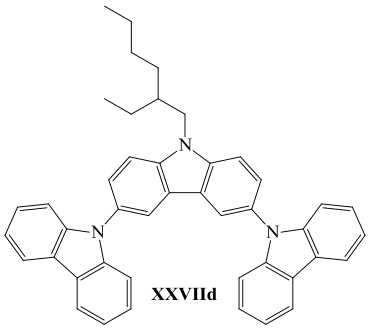

XXVIId

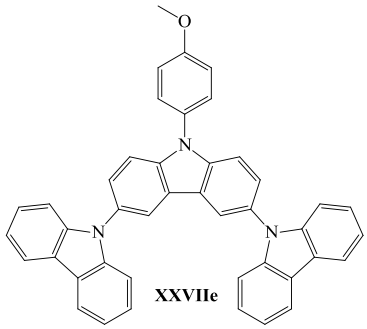

XXVIIe

As in the case of carbazole, using C- or N-connectivity of the imidazole moiety the effective conjugation length of compounds can be changed as it was demonstrated on the example of compounds **XXVIIIa-XXIXb** The N-linked compounds **XXIXa-b** possessed higher triplet energies than their C-linked analogues **XXVIIIa-b** by 0.23 eV. These bipolar compounds exhibited high thermal stability. Their molecular glasses showed high morphological stability blue PHOLED with Flrpic doped in **XXIXb** achieved a maximum external quantum efficiency, current efficiency and power efficiency of 16.3%, 35.7 cd/A and 23.3 lm/W, respectively. The characteristics of the device confirmed the suitability of N-connected bipolar hosts for the blue emitters. The C-linked analogue showed lower

triplet energy, which made it suitable as a bipolar host for green emitters. A green PHOLED having **XXVIIIa** as the host doped with $(PBi)_2Ir(acac)$ achieved a maximum external quantum efficiency, current efficiency and power efficiency of 20.1%, 70.4 cd/A and 63.2 lm/W, respectively. [84]

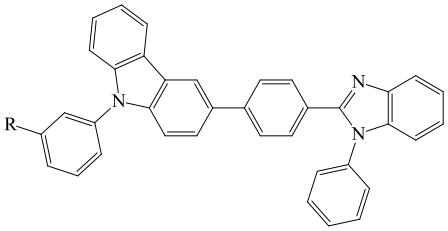

XXVIIIa: **R=** **H**

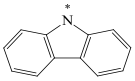

XXVIIIb: **R=**

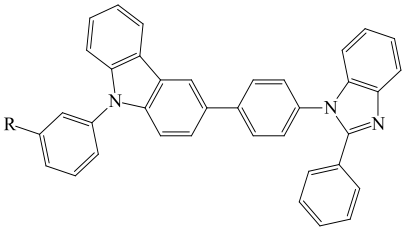

XXIXa: **R=** **H**

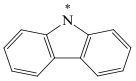

XXIXb: **R=**

Bipolar molecule **XXX** consisting of electron-donating carbazole and electron-accepting phenylbenzimidazole (linked via N atom) exhibited high triplet energy (2.71 eV), balanced charge transport and high morphological stability of the molecular glass. **XXX** doped with $Os(bpftz)_2(PPh_2Me)_2$, $(PPy)_2Ir(acac)$ and FIrpic under the same PHOLED structure showed excellent performance with external quantum efficiencies of 19.1% for red, 17.8% for green and 12.7% for blue. [85]

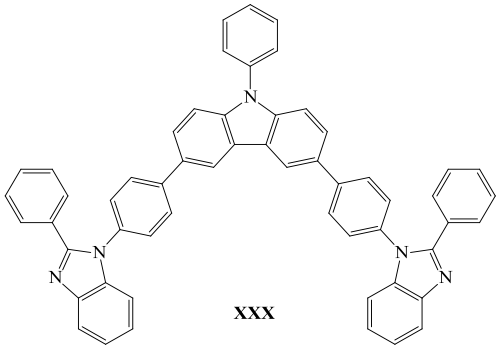

XXX

A carbazole-carboline core was used by Byeon et al. [86] as a backbone structure of high triplet energy host materials **XXXIa-c**. The HOMO of the three host materials **XXXIa-c** were found to be similarly localized on the carbazole and indole units of carboline because of the electron rich character of these moieties. The LUMO distribution affected by the substituents of the carbazole-carboline core were different for the three compounds. Therefore, the host materials have similar HOMO levels, but different LUMO levels. This trend agrees with the experimental results, ionization potential of the compounds were found to be 5.90 eV and electron affinities ranged from 2.67 eV to 2.79 eV. Triplet energies of **XXXIa**, **XXXIb** and **XXXIc** established from the phosphorescence spectra were 2.88 eV, 2.88 eV and

2.85 eV, respectively. Compounds **XXXIa** and **XXXIc** demonstrated poor electron and hole transport properties while **XXXIb** exhibited enhanced charge mobilities of both holes and electrons. Maximum external quantum efficiencies of PHOLEDs with **XXXIa**, **XXXIb** and **XXXIc** as host materials were 23.4%, 19.6% and 17.4%, respectively.

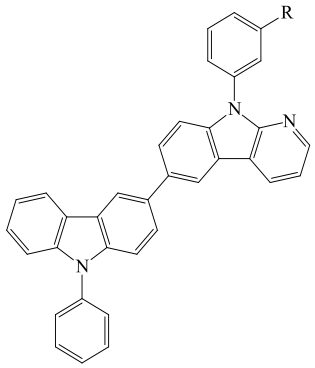

XXXIa: R= H

XXXIb: R= CN

XXXIc: R=

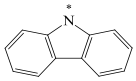

Energy levels and properties of host materials can be effectively modified by inserting strong electron withdrawing groups. *N*-Heterocycles are generally electron withdrawing in nature and can transport electrons better than holes. [87,88] It was shown that energy levels of compounds **XXXIIa-f** can be tuned by the change of heterocyclic cores and their nitrogen atom orientations. The decrease of energy gap between singlet and triplet excited states (ΔE_{ST}) was achieved with introducing one or two nitrogen atoms into the central ring. Replacing benzene ring by pyridine, a decrease of ΔE_{ST} by 0.10-0.16 eV was observed for compounds **XXXIIb-d**. In addition, with introducing one more nitrogen atom into the central heterocyclic core, further decreases in ΔE_{ST} by 0.20 and 0.18 eV were achieved for **XXXIIe** and **XXXIIf**, respectively. Their charge carrier mobilities can also be tuned by the choice of heterocyclic cores. Generally, electron mobility of organic materials is several orders of magnitude lower than hole mobility. The increased electron mobility may facilitate electron injection and transport into the emitter layer to give a balanced charge carrier transport and thus higher recombination efficiency. FIrpic doped into **XXXIIa-d** and **XXXIIf** exhibited monoexponential decay curves with relatively long lifetimes between 1.51 μs and 1.73 μs and demonstrated high photoluminescence quantum efficiency over 70%, which can be attributed to good confinement of triplet energy on the FIrpic molecules and efficient energy transfer from the host to the guest. PHOLEDs were fabricated by doping FIrpic, into the developed host materials. For the blue PHOLEDs, the highest efficiency was achieved for the device with the host **XXXIIb**, giving quantum efficiency of 24.3% and power efficiency of 46.1 lm/W at 100 cd/m^2. [89,90,91]

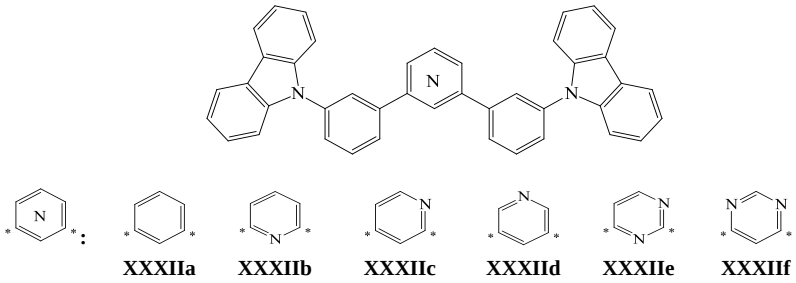

XXXIIa XXXIIb XXXIIc XXXIId XXXIIe XXXIIf

2.3.2. Triphenylamine-based hole transporting materials for phosphorescent organic light emitting diodes

HTMs should have good hole transport properties, appropriate HOMO and LUMO levels and high triplet energy for triplet exciton blocking. [92] The most common triphenylamine-based HTMs for PHOLED fabrication are *N*,*N*′-di(1-naphthyl)-*N*,*N*′-diphenyl-(1,1′-biphenyl)-4,4′-diamine (NPB) [93,94,95],tris(4-carbazoyl-9-ylphenyl)amine (TCTA) [96,97,98] and 4,4′-cyclohexylidenebis[*N*,*N*-bis(4-methylphenyl) benzenamine] (TAPC) [99,100,101]. These compounds are often used for improvement of PHOLED performance. The superior PHOLED characteristics can be achieved due to the utilization of mixture of HTM and bipolar host in the emissive layer. The blending of TCTA and host material in the emissive layer greatly improved the efficiency of device. The same materials were used for HTL and ETL adjacent to the emissive layer. The PHOLED reached maximum external quantum and power efficiencies of 20.4% and 55.4 lm/W, respectively. [102] In addition, PHOLED characteristics can be enhanced by the incorporation of interlayer between the HTL and ETL. Devices with TCTA as interlayer between NPB and ETL with FIrpic were investigated by Lee et al. [103]. The performance of blue PHOLEDs without interlayer was inefficient, external quantum efficiencies were less than 1%. The triplet energy of FIrpic (2.62 eV) is higher than that of NPB (2.3eV), therefore energy transfer from the excited state of the FIrpic blue emitter to the triplet state of NPB could occur. The device with TCTA interlayer exhibited significantly improved performances with maximum external quantum efficiencies of 10%. TCTA has large triplet energy 2.85 eV and thus act as exciton blocking layer that confine excitons within the emissive layer.

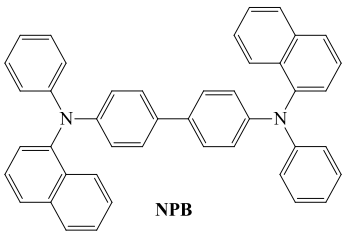

NPB

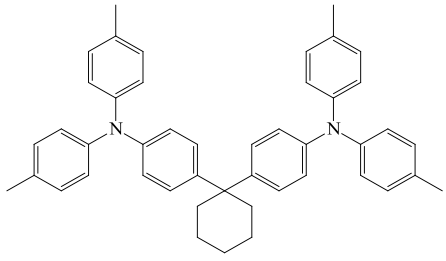

TAPC

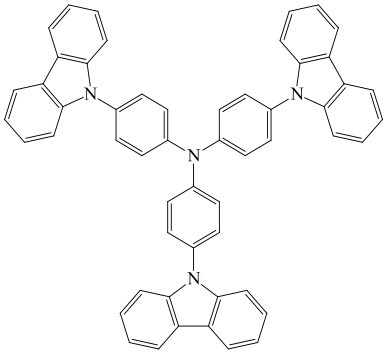

TCTA

Frequently, NPB, TAPC and TCTA serve as standards to compare the characteristics of new HTM for PHOLED. The synthesis of effective HTMs and optimization of PHOLEDs structures are actively investigated by many researchers. Two PHOLEDs with TCTA and **XXXIII** as the HTMs were compared by Cho et al. [104]. The device with **XXXIII** showed the similar current density to the device having TCTA. **XXXIII** has similar energy barrier to TCTA because of similar HOMO level of 5.72 eV and 5.70 eV, respectively. This indicates that hole-transporting properties of both compounds are comparable. The quantum efficiency of the device containing **XXXIII** was higher than that of the device containing TCTA over all luminance range. The quantum efficiency was mainly affected by the charge balance and charge leakage in the emitting layer. Blue host material used in PHOLED structures has the LUMO level of 2.55 eV, while the LUMO of **XXXIII** is 2.10 eV. The energy barrier of 0.45 eV is estimated for electron injection from emitting layer to HTL. However, there is only 0.15 eV energy barrier for electron injection from host material to TCTA, leading to less effective charge confinement inside the emitting layer.

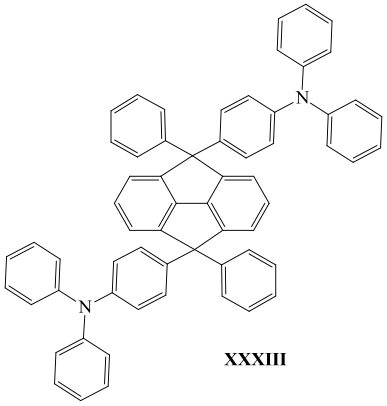

XXXIII

Compound **XXXIV** demonstrated T_g above 140 °C and good hole-transporting properties, hole mobility reached $1.4 \cdot 10^{-3}$ $cm^2/(Vs)$. This compound has appropriate

HOMO level of -5.78 eV for hole injection to host material (-6.13 eV) and high triplet energy over 2.90 eV for triplet exciton blocking. Compound **XXXIV** was used as HTM in PHOLEDs. The external quantum efficiency at 1000 cd/m^2 of the deep-blue and green devices was 19.7% and 24.2%, respectively. [105]

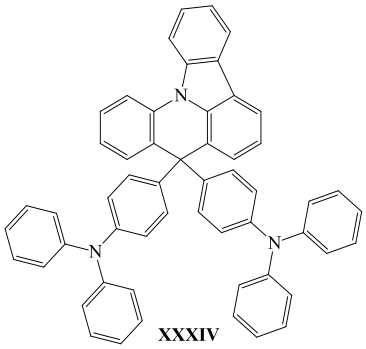

XXXIV

Deep-blue PHOLEDs with **XXXIV**, TAPC and **XXXV** as a HTMs were fabricated and investigated by Kim et al. [106]. The current density and luminance of the device containing **XXXV** were found to be much higher than those of the devices containing TAPC and **XXXIV** at the same driving voltage. This observation indicates that **XXXV** is much better than TAPC and **XXXIV** with respect of injection of holes into emitting layer. The quantum efficiency and power efficiency of the device containing **XXXV** were slightly higher than those of TAPC-containing device and similar to those of the device containing **XXXIV**. The maximum quantum efficiency of the device containing **XXXV** was found to be 17.3% and the power efficiency reached 21.1 lm/W.

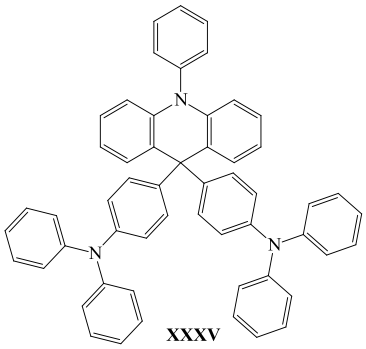

XXXV

The hole current densities were found to be **XXXVIa** < TAPC < **XXXVIb** [107]. Di-*p*-tolylamine is a better hole transport unit than diphenylamine which explains the higher hole current density observed in **XXXVIb**. Hole mobility of this compound is even higher than that of TAPC which is well known as a HTM with high hole mobility [108]. The quantum efficiency of blue PHOLED was the highest when **XXXVIa** was used as HTM . It showed maximum quantum efficiency of 21.8%. The triplet energy of **XXXVIa** is much higher than that of FIrpic and there is

a high energy barrier of 0.6 eV to prevent electron leakage from the emitting layer to the HTL. In the case of the device containing **XXXVIb**, the quantum efficiency was rather low due to the high hole current density in the device, which disrupted the balance of holes and electrons in the emitting layer. PHOLED with TAPC showed lower maximum quantum efficiency of 18.5%, because of the higher energy barrier for hole injection.

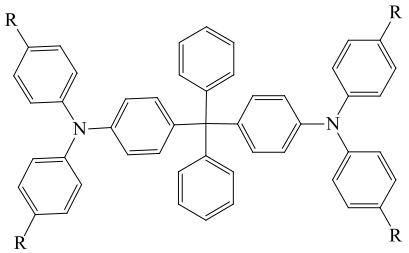

XXXVIa: **R=H**
XXXVIb: **R=Me**

Compound **XXVII** demonstrates high thermal stability with 5% weight loss at 438 °C. The use of the *ortho*-linked terphenyl-core improved the thermal stability of **XXVII** compared with that of TAPC having cyclohexyl-core. IP_{CV} corresponding to the HOMO and EA_{CV} corresponding to LUMO for **XXVII** were estimated to be 5.70 eV and 2.44 eV. The hole mobility of **XXVII** was found to be $9.7 \cdot 10^{-3}$ cm^2/Vs, i.e. similar to $9.4 \cdot 10^{-3}$ cm^2/V s recorded for TAPC at same electric field. Blue PHOLEDs were fabricated using **XXVII** as HTM and performance of device was compared with that of the device containing TAPC. Good hole transport and injection properties of **XXVII** improved the characteristics of the blue PHOLED. The maximum quantum efficiency of device with **XXVII** was 22.7%. In the case of the device having TAPC, the maximum quantum efficiency was less than 20%. The power efficiency of the device containing **XXVII** was 26.8 lm/W, which was higher than of the TAPC-containing device. [109]

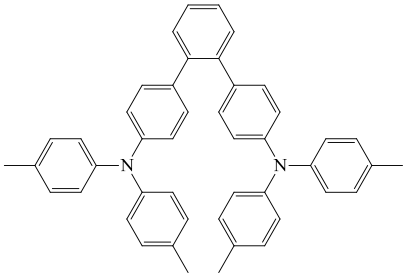

XXXVII

Compound **XXXVIII** was reported by Hung et al. [110] to have high thermal stability. The molecular glass of the compounds also showed high morphological stability with T_g at 124 °C. The molecular design of **XXXVIII** ensured appropriate HOMO energy level (-5.22 eV) to provide low hole injection barrier from the anode and LUMO energy level (-1.75 eV) to block electrons injected from the cathode.

This compound showed good hole transport properties with hole mobility higher than 10^{-3} cm^2/Vs and appropriate triplet energy of 2.87 eV. The blue PHOLED with guest/host system FIrpic/SiCa and HTM of **XXXVIII** was fabricated. This device exhibited maximum quantum efficiency of 18.3% and power efficiency of 31 lm/W.

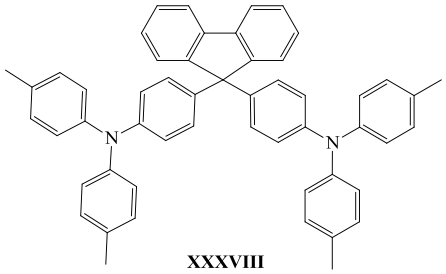

XXXVIII

2.4. Conclusions from literature review

Various organic semiconductors have been designed and synthesized over the past decade. Carbazole- and triphenylamine-based derivatives represent one of the most widely investigated families of charge transporting materials. These materials contain systems of conjugated π bonds. The holes and/or electrons move within the π-conjugated system of these materials. In order to obtain the desirable properties of compounds, various groups and substituents are attached to carbazole or triphenylamine molecules. The charge transporting materials described in the literature review demonstrate that even a slight change in their structure affects the efficiency of the device. As an example, extended π-conjugated linker in the dyes can increase conversion efficiency of DSSC. On the contrary, a reduced level of π-conjugation in the host materials leads to higher quantum efficiency of PHOLED. Investigation of charge transporting materials with structural differences can give information about dependence of structure on thermal, optical, electrochemical and photoelectrical properties. The received information is important for the synthesis of new compounds for effective organic optoelectronic devices. In this work, the new charge transporting compounds were described and their structure-properties relationship investigated. Computational chemistry was used to analyse experimental results of synthesized compounds. Theoretical calculations help to better understand charge transport processes which take place in optically or electrically active compounds.

3. EXPERIMENTAL

3.1. Instrumentation

The course of the reactions was monitored by thin layer chromatography (TLC) on Silica gel 60 F254 plates under UV light.

The compounds were purified by column chromatography using silica gel (grade 60, 70–230 mesh, particle size 0.063–0.2 mm, Fluka and grade 60, 230–400 mesh, particle size 0.04–0.063 mm, Fluka).

^{1}H NMR and ^{13}C NMR spectra were obtained of the solutions in deuterated chloroform or dimethyl sulfoxide with a Varian Unity Inova or a Bruker Avance III spectrometers. The data are given as chemical shifts in δ (ppm) and tetramethylsilane was used as an internal standart.

Infrared (IR) spectroscopy was performed with Perkin Elmer Spectrum GX II FT-IR System or Vertex 70 Bruker using KBr pallets or pure materials.

Mass spectra were obtained on a Waters ZQ 2000 mass spectrometer.

Melting point (mp) were determined using Electrothermal Mel-Temp melting point apparatus.

Thermogravimetric analysis (TGA) was performed on Mettler TGA/SDTA851e/LF/1100 apparatus at a heating rate of 20 ºC/min under nitrogen atmosphere.

Differential scanning calorimetry (DSC) measurements were performed on DSC Q 100 TA Instrument thermal analyser at a heating/cooling rate of 10 ºC/min under nitrogen atmosphere.

Optical and photophysical properties of 10^{-4} M solutions in tetrahydrofuran and pure layers of the synthesized compounds were recorded using a Perkin Elmer Lambda 35 and an Edinburgh Instruments FLS980 spectrometers.

Cyclic voltammetry (CV) measurements were carried out using Autolab potentiostat PGSTAT20 in a three electrode cell using platinum rod as a counter electrode, glassy carbon as working electrode and $Ag/AgNO_3$ as the reference electrode. The experiments were carried out in dry dichloromethane solution containing 0.1 M tetrabutylammonium perchlorate as electrolyte at room temperature under nitrogen atmosphere at a scan rate 50 mV/s. The measurements were calibrated using the internal standard ferrocene/ferrocenium (Fc/Fc^{+}).

The ionization potentials (IP_{PE}) of the films of the synthesized compounds were measured by the electron photoemission in air method [111]. The samples for the ionization potential measurements were prepared by dissolving compounds in solvents and coated onto Al plates pre-coated with 0.5 μm thick adhesive layer of the copolymer of methylmethacrylate and methacrylic acid (MKM). The function of this layer was not only to improve adhesion but also to eliminate electron photoemission from Al.

Hole drift mobility of the materials was estimated by a time-of-flight (TOF) method. The samples were fabricated with structures of ITO/compound/Al. Commercial indium tin oxide (ITO) coated glass was used as a substrate, which was first cleaned chemically using a bath of distilled water and acetone. Organic and Al

films were sequentially vacuum-deposited onto precleaned ITO-coated glass substrates under the vacuum of 2-5·10^{-6} mBar using vacuum equipment from Kurt J. Lesker in-built in an MB EcoVap4G glove box. In the TOF experiments, charges were generated by a pulsed third-harmonic Nd:YAG laser EKSPLA NL300 working at a pulse duration of 3-6 ns and the wavelength of 355 nm. Electric fields were applied by a Keithley 6517B electrometer. A digital storage oscilloscope Tektronix TDS 3032C was used to record TOF transients. The drift mobility was calculated by using the formula $\mu=d^2/U\cdot t_t$, where d is the layer thickness, and U the surface potential at the moment of illumination, and t_t is the transit time which was taken from the TOF transients.

Current-voltage curves were recorded using a Keithley 2400 Source Meter. A xenon lamp fitted with an AM1.5 global filter was used for illumination. Silicon photodiode was used to calibrate the light source to give 1 sun light intensity. Voltage was cyclically changed from 0 to 1 V and to -1 V under illumination or in the dark.

Transient absorption spectroscopy (TAS) was conducted using a pump–probe system. Probe light was Bentham IL1 lamp output attenuated with neutral density filters to give roughly 1 sun light intensity. Light was focused onto the sample and subsequently onto a monochromator. The photodetector had a rise time of 100 ns and was connected to a Costronics 2008 amplifier which was further connected to an oscilloscope with a time resolution of 4 ns. At least 20 laser pulse repeats per probe wavelength were used for averaging. The pump signal was supplied by an Nd:YAG 1064 nm light pumped Opotek Opolette 355 with 10 Hz repetition rate, 6 ns pulse duration. A waveguide was used to direct and decollimate the laser light.

A Keithley source meter 2400-C was utilized for recoding of the current density-voltage characteristics. The current density–luminance characteristics were estimated using a calibrated silicon photodiode with the 6517B Keithley electrometer. Electroluminescence (EL) spectra were recorded by an Avantes AvaSpec-2048XL spectrometer. The current, power and external quantum efficiencies were estimated utilizing the current density, luminance, and EL spectra as reported earlier [112].

3.2. Computational methodology

The computations of synthesized compounds were performed with the Gaussian 09 program [113]. The density functional (DFT) [114] method employing B3LYP [115,116] and ωB97X-D [117] functionals were used in conjunction with the 6-31G(d,p) basis set.

The spectroscopic properties of the molecules were calculated by mean of time dependent density functional theory method (TDDFT) [118,119,120]. Up to 20 excited states were calculated and the theoretical absorption bands were obtained by considering a band half-width at half-maximum of 0.1-0.3 eV.

The adiabatic ionization potentials (IP) were calculated at the B3LYP/6-31G(d,p) level as energy difference between neutral and cation radical species at the neutral state geometry.

Calculations of the cations of compounds were also performed by using the restricted open-shell Hartree-Fock (ROHF) method with the 6-31G* basis set. ROHF calculations can result in structural symmetry breaking, and thus localized charges, even in cases where DFT methods suggest delocalized charges.[121]

The intermolecular interaction energies of the optimized model dimers of compounds were calculated with respect to the isolated monomers at the ωB97XD/6-31G(d,p) level, including corrections for the basis set superposition error (BSSE) computed by the counterpoise correction method. [122] The zero point energy (ZPE) correction has been also taken into account.

The electronic couplings between the HOMO orbitals of two adjacent molecules were calculated at the B3LYP/ 6-31G(d,p) level, according to the approach described by Valeev et al. [123].

3.3. Dye sensitized solar cells fabrication

A glass plate covered with a thin film of SnO_2:F was washed with a detergent, rinsed with deionized water and isopropyl alcohol, dried and heated at 450 °C in air for 30 min. A thin film of TiO_2 blocking layer was deposited by spray pyrolysis of 0.4 M Ti(acetoacetonate) solution in ethanol at 450 °C with air flow. After cooling down to room temperature, TiO_2 paste was applied by doctor blading using 50 μm scotch tape as a spacer. After drying in air for 30 min, the films were sintered at 450 °C for 30 min, giving 5 μm thick TiO_2 films as determined by profilometry. A $TiCl_4$ post-treatment was then carried out by immersing the films into a solution of 0.84 g $TiCl_4 \cdot 2THF$ in 80 mL of deionized water for 30 min at 70 °C. Substrates were then washed with deionized water and sintered for 30 min at 450 °C and cut into 1.5×2.5 cm pieces. Surrounding TiO_2 was scraped off to give 1 cm^2 active area, then heated again at 450 °C for 30 min and while still hot (100 °C) immersed into a 0.3 mM solution of cis–bis(isothiocyanato)bis(2,2'-bipyridyl-4,4'-dicarboxylato)ruthenium (II) (N719) dye in 1:1 mixture of acetonitrile:tert-butyl alcohol for 16 h. Then HTM was melt on the TiO_2 film. In some cases LiTFSI in acetonitrile was drop-cast on top of dye-sensitized TiO_2 prior to melting the HTM. In order to *p*-dope the hole conductor, iodine crystals and the vial was sealed. After doping, a pressed graphite electrode was applied to complete the solar cell.

3.4. Phosphorescent light emitting diodes fabrication

Devices with the structures: ITO/m-MTDATA/host:$Ir(ppy)_3$/Bphen/Ca:Al were fabricates by deposition of different organic layers and metal electrodes onto precleaned indium tin oxide (ITO) coated glass substrate under the vacuum higher than $3 \cdot 10^{-6}$ mBar. 4,4′,4″-Tris[phenyl(*m*-tolyl)amino]triphenylamine (*m*-MTDATA) and 4,7-diphenyl-1,10-phenanthroline (Bphen) were used for the preparation of hole- and electron-transporting layers, respectively. Since calcium (Ca) is highly reactive and corrodes quickly in the ambient atmosphere, Ca layer was topped with aluminium (Al). Ca:Al layer was used as the cathode. The emission layer was prepared by co-deposition of host (m/m 90%) and $Ir(ppy)_3$ (m/m 10%) from two

different sources. The deposition rate of $Ir(ppy)_3$ was of 0.1 Å/s, while the deposition rate of host was set 1.0 Å/s.

3.5. Materials

9*H*-carbazole (95%, Reakhim), 1-bromohexane (98%, Aldrich), potassium-*tert*-butoxide (98%, Aldrich), phosphorus(V) oxychloride ($POCl_3$, 99%, Aldrich), malononitrile (99%, Aldrich), zinc acetate hydrate ($Zn(OAc)_2 \cdot 2H_2O$, 98%, Aldrich), anhydrous sodium sulfate (Na_2SO_4, 99%, Reachem), iron(III) chloride ($FeCl_3$, 98%, Aldrich), *N*-bromosuccinimide (99%, Aldrich), acrolein diethyl acetal (96%, Aldrich), tetrabutylammonium acetate (97%, Aldrich), palladium(II)acetate (98%, Aldrich), anhydrous *N*,*N*'-dimethylformamide (99.8%, Aldrich), 4-iodoanisole (98%, Aldrich), aniline (98%, Aldrich), 18-crown-6 (98%, Aldrich), copper powder (Cu, 99%, Aldrich), *o*-dichlorobenzene (99%, Aldrich), phenylhydrazine (97%, Fluka), *N*-methyl-*N*-phenylhydrazine (97%, Aldrich), *N*,*N*-diphenylhydrazine hydrochloride (97%, Aldrich), 1-(chloromethyl)-4-vinylbenzene (98%, Aldrich), tetrabutylamonium hydrosulphate (98%, Aldrich), benzil (98%, Aldrich), 9-ethyl-9*H*-carbazole-3-carbaldehyde (98%, Aldrich), 9-ethyl-9*H*-carbazol-3-amine (98%, Aldrich) *tert*-butyl chloride (99%, Aldrich), 2-ethylhexyl bromide (95%, Aldrich), tin(II) chloride ($SnCl_2$, 98%, Aldrich), 4,4'-diaminobenzophenone (97%, Aldrich), iodobenzene (98%, Aldrich), 4-iodotoluene (99%, Aldrich), diethyl benzylphosphonate (99%, Aldrich), anhydrous tetrahydrofuran (99.9%, Aldrich), diethyl-4-methylbenzylphosphonate (97%, Aldrich), diethyl 4-methoxybenzylphosphonate (95%, TCI) were purchased as reagent grade chemicals and used as received.

9-Hexyl-9*H*-carbazole (1)

Compound was synthesized according to the procedure described in literature [124].

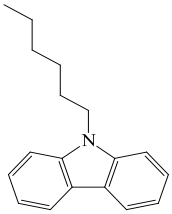

9-Hexyl-9*H*-carbazole-3-carbaldehyde (2)

Compound was synthesized from compound **1** according to the procedure outlined in the literature [124].

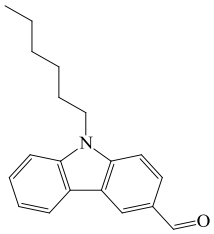

2-((9-Hexyl-9*H*-carbazol-3-yl)methylene)malononitrile (3)

To a solution of aldehyde **2** (1 g, 3.6 mmol) and malononitrile (0.28 g, 4.3 mmol) in *N*,*N*-dimethylformamide (20 ml) $Zn(OAc)_2 \cdot 2H_2O$ (0.94 g, 4.3 mmol) was added. The reaction mixture was stirred at room temperature for 1 h. then poured into water and extracted with chloroform. The organic layer was dried with anhydrous Na_2SO_4, filtered and distilled. The product was purified by column chromatography using the mixture of ethyl acetate and hexane in a volume ratio of 1:10 as an eluent. The compound **3** was crystallized from the eluent. The yield of yellow crystals was 0.83 g (71%), mp = 120-121 °C.

IR, cm^{-1}: 3064 (ar. C-H), 2962, 2931, 2857 (aliph. C-H), 2220 (CN), 1629 (aliph. C=C), 1597, 1501, 1468 (ar. C=C), 1320, 1234 (C-N).

^{1}H NMR (400 MHz, $CDCl_3$-d_6, δ): 0.87 (t, 3H, *J*=7.1 Hz, CH_3), 1.24-142 (m, 6H, CH_2), 1.88 (p, 2H, *J*=7.3 Hz, CH_2), 4.32 (t, 2H, *J*=7.3 Hz, CH_2), 7.35 (t, 1H, *J*=7.0 Hz, ar.), 7.44-7.48 (m, 2H, ar.), 7.54-7.58 (m, 1H, ar.),7,82 (s, 1H, CH), 8.07 (dd, 1H, *J*=1.8, *J*=8.8, Hz, ar.), 8.12 (d, 1H, *J*=7.7, Hz, ar.), 8.60 (d, 1H, *J*=1.8, Hz, ar.).

^{13}C NMR (101 MHz, $CDCl_3$-d_6, δ): 13.97, 22.50, 26.89, 28.91, 31.47, 43.59, 76.41, 109.67, 109.74, 114.20, 115.15, 120.95, 121.03, 122.35, 122.59, 123.69, 125.11, 127.39, 128.57, 141.22, 143.90, 160.10.

MS ($APCl^+$), *m/z* = 328 $[M+H]^+$.

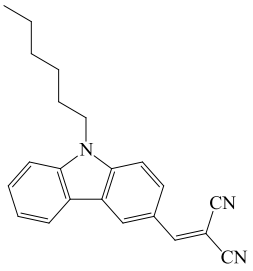

2,2'-((9,9'-dihexyl-9*H*,9'*H*-[3,3'-bicarbazole]-6,6'diyl)bis (methanylylidene)) dimalononitrile (4)

$FeCl_3$ (0.5 g, 3 mmol) was added to the solution of compound **3** (0.5 g, 1.5 mmol) in dichloromethane (10 ml). The reaction mixture was stirred at room temperature for 2 h. then filtered and washed several times with water. The organic layer was dried with anhydrous Na_2SO_4, filtered and distilled. The product was purified by column chromatography using the mixture of acetone and hexane in a

volume ratio of 1:4 as an eluent. The compound **4** was crystallized from the eluent. The yield of orange crystals was 0.27 g (56%), mp = 246-247 °C.

IR, cm^{-1}: 3038 (ar. C-H), 2953, 2925, 2851 (aliph. C-H), 2217 (CN), 1633 (aliph. C=C), 1557, 1491, 1468 (ar. C=C), 1240 (C-N).

^{1}H NMR (400 MHz, $CDCl_3$-d_6, δ): 0.89 (t, 6H, *J*=7.1 Hz, CH_3), 1.25-145 (m, 12H, CH_2), 1.94 (p, 4H, *J*=7.3 Hz, CH_2), 4.39 (t, 4H, *J*=7.3 Hz, CH_2), 7.50 (d, 2H, *J*=8.8 Hz, ar.), 7.55 (d, 2H, *J*=8.9 Hz, ar.), 7.87-7.91 (m, 4H, ar., CH), 8.08 (d, 2H, *J*=8.7 Hz, ar.), 8.39 (s, 2H, ar.), 8.76 (s, 2H, ar.)

^{13}C NMR (101 MHz, $CDCl_3$-d_6, δ): 14.28, 22.62, 26.92, 28.93, 31.28, 43.56, 109.82, 114.20, 115.36, 119.82, 122.52, 123.34, 123.91, 124.99, 127.25, 129.05, 134.82, 140.45, 144.33, 159.99.

MS (APCl$^+$), *m/z* = 654 $[M+H]^+$.

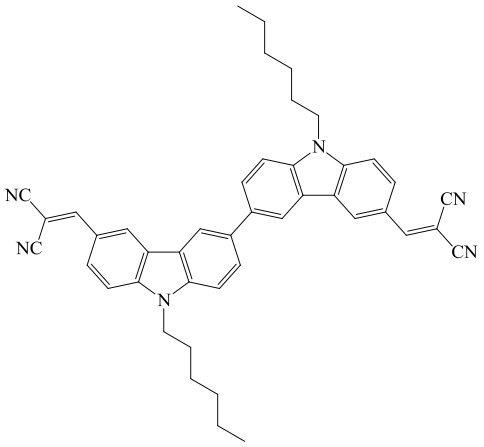

3-Bromo-9-hexyl-9*H*-carbazole (5) was synthesized from compound **1** according to the procedure described in literature [125].

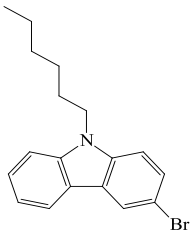

(*E*)-3-(9-Hexyl-9*H*-carbazol-3-yl)acrylaldehyde (6)

Acrolein diethyl acetal (2.8 ml, 18 mmol), tetrabutylammonium acetate (3.65 g, 12 mmol), K_2CO_3 (1.25 g, 9 mmol), KCl (0.45 g, 6 mmol) and palladium(II)acetate (0.04 g, 0.18 mmol) were added to the solution of compound **5** (2 g, 6 mmol) in anhydrous *N*,*N*'-dimethylformamide (20 ml) under argon atmosphere. The reaction mixture was stirred at 80°C for 5 h. After cooling 2M HCl was added drop wise to reaction mixture up to pH ~5. The reaction mixture was

stirred for 0.5 h then extracted with chloroform. The organic layer was dried with anhydrous Na_2SO_4, filtered and distilled. The product was purified by column chromatography using the mixture of ethyl acetate and hexane in a volume ratio of 1:6 as an eluent. The yield of yellow solid was 1.48 g (82%).

IR, cm^{-1}: 3052 (ar. C-H), 2957, 2928, 2856, 2745 (aliph. C-H), 1663 (C=O), 1612, 1596, 1490 (ar. C=C).

^{1}H NMR (400 MHz, $CDCl_3$-d_6, δ): 0.86 (t, 3H, *J*=7.1 Hz, CH_3), 1.25-1.42 (m, 6H, CH_2), 1.86 (p, 2H, *J*=7.2 Hz, CH_2), 4.29 (t, 2H, *J*=7.2 Hz, CH_2), 6.78 (dd, 1H, *J*=7.8 Hz, *J*=15.7 Hz, CH=CH), 7.29 (t, 1H, *J*=7.9 Hz, ar.), 7.39-7.44 (m, 2H, ar.), 7.49-7.53 (m, 1H, ar.), 7.63-7.70 (m, 2H, ar., CH=CH) 8.11 (d, 1H, *J*=7.7 Hz, ar.), 8.27 (s, 1H, ar.), 9.70 (d, 1H, *J*=7.8 Hz, CHO).

^{13}C NMR (101 MHz, $CDCl_3$-d_6, δ): 14.03, 22.55, 26.95, 28.95, 31.55, 43.36, 109.28, 109.31, 119.90, 120.589, 212.97, 122.67, 123.39, 125.02, 125.85, 126.08, 126.53, 140.98, 142.29, 154.71, 193.86.

MS ($APCl^+$), *m/z* = 306 $[M+H]^+$.

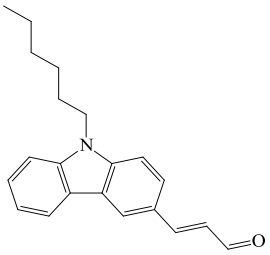

(*E*)-2-(3-(9-Hexyl-9*H*-carbazol-3-yl)allylidene)malononitrile (7)

Compound **7** was obtained from aldehyde **6** (1 g, 3 mmol), malononitrile (0.26 g, 3.9 mmol) and $Zn(OAc)_2 \cdot 2H_2O$ (0.86 g, 3.9 mmol) by the similar method as compound **3**. The product was purified by column chromatography using the mixture of acetone and hexane in a volume ratio of 1:6 as an eluent. The compound **7** was crystallized from the eluent. The yield of red crystals was 0.90 g (85%), mp = 126-127 °C.

IR, cm^{-1}: 3054 (ar. C-H), 2955, 2925, 2858 (aliph. C-H), 2211 (CN), 1562, 1547, 1492 (ar. C=C), 1325, 1243 (C-N).

^{1}H NMR (400 MHz, $CDCl_3$-d_6, δ): 0.86 (t, 3H, *J*=7.1 Hz, CH_3), 1.24-142 (m, 6H, CH_2), 1.87 (p, 2H, *J*=7.3 Hz, CH_2), 4.33 (t, 2H, *J*=7.3 Hz, CH_2), 7.23-7.27 (m, 1H, CH=CH), 7.30-7.33 (m, 1H, ar.), 7.39-7.45 (m, 3H, ar., CH), 7.50-7.54 (m, 1H, ar.), 7.57 (d, 1H, *J*=11.6 Hz, ar.), 7.74 (dd, 1H, *J*=1.7 Hz, *J*=8.6 Hz, CH=CH) 8.12 (d, 1H, *J*=7.7 Hz, ar.), 8.28 (d, 1H, *J*=1.6 Hz ar.).

^{13}C NMR (101 MHz, $CDCl_3$-d_6, δ): 13.98, 22.52, 26.92, 28.94, 31.51, 43.45, 79.01, 109.48, 109.63, 112.60, 114.42, 119.39, 120.10, 120.39, 120.76, 122.64, 122.71, 122.98, 123.79, 125.10, 126.88, 126.91, 141.10, 142.90, 149.57, 152.34, 157.50, 160.55.

MS ($APCl^+$), *m/z* = 354 $[M+H]^+$.

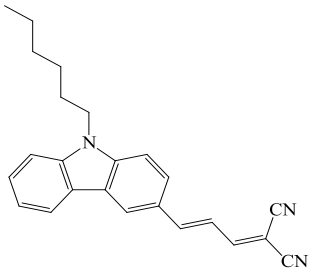

2,2'-((2*E*,2'*E*)-(9,9'-dihexyl-9H,9'H-[3,3'-bicarbazol]-6,6'-diyl)bis(prop-2-en-3-yl-1-ylidene))dimalononitrile (8)

Compound **8** was synthesized from compound **7** (0.5 g, 1.4 mmol) and $FeCl_3$ (0.46 g, 2.8 mmol) by the similar method as compound **4**. The product was purified by column chromatography using the mixture of acetone and hexane in a volume ratio of 1:3 as an eluent. The compound **8** was crystallized from the eluent. The yield of red crystals was 0.30 g (61%), mp = 265-266 °C.

IR, cm^{-1}: 3054 (ar. C-H), 2955, 2925, 2858 (aliph. C-H), 2211 (CN), 1562, 1547, 1492 (ar. C=C), 1244 (C-N).

^{1}H NMR (400 MHz, $CDCl_3$-d_6, δ): 0.88 (t, 6H, *J*=7.0 Hz, CH_3), 1.28-144 (m, 12H, CH_2), 1.92 (p, 4H, *J*=7.1 Hz, CH_2), 4.34 (t, 4H, *J*=7.1 Hz, CH_2), 7.30 (dd, 2H, *J*=11.5 Hz, *J*=14.6 Hz, CH=CH), 7.41-7.49 (m, 4H, ar., CH), 7.52-7.59 (m, 4H, ar., CH=CH), 7.68 (d, 2H, *J*=8.5 Hz, ar.), 7.91 (d, 2H, *J*=8.3 Hz, ar.), 8.41 (s, 2H, ar.), 8.44 (s, 2H, ar.).

^{13}C NMR (101 MHz, $CDCl_3$-d_6, δ): 14.01, 22.54, 26.94, 29.01, 31.53, 43.61, 78.98, 109.72, 109.89, 112.68, 114.37, 119.28, 119.42, 122.33, 123.34, 123.99, 125.20, 126.62, 127.59, 134.22, 140.32, 143.33, 152.27, 160.55.

MS ($APCl^+$), *m/z* = 706 $[M+H]^+$.

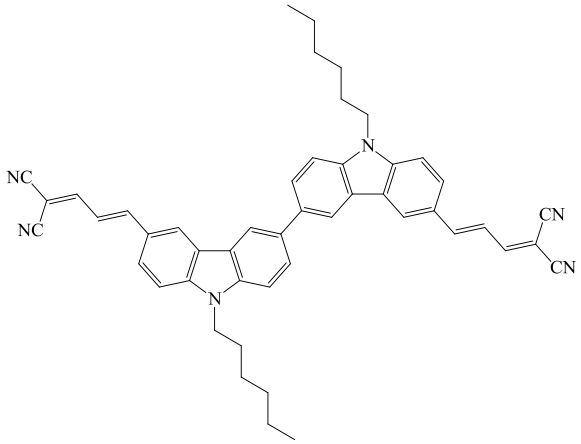

4-Methoxy-*N*-(4-methoxyphenyl)-*N*-phenylamine (9)

Compound **9** was synthesized according to the procedure described in literature [126].

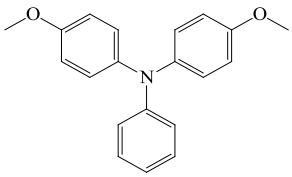

4-(Bis(4-methoxyphenyl)amino)benzaldehyde (10)

Compound **10** was obtained from compound **9** according to the procedure described in literature [127].

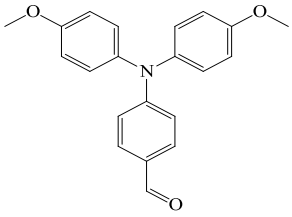

4-(Bis(4-metoxyphenyl)amino)benzaldehyde *N*-phenylhydrazone (11)

Phenylhydrazine (1 ml, 10.4 mmol) was added to the solution of aldehyde **10** (1.7 g, 5.2 mmol) in 10 ml of methanol. The reaction mixture was refluxed at 65 ºC with stirring for ca. 0.5 h until no aldehyde was left. After cooling, a yellowish precipitate was filtered, washed with large amount of methanol and dried. The yield of **11** was 1.9 g (85%).

IR (KBr), cm^{-1}: 3319 (N-H), 3027, 3000 (ar. C-H), 2956, 2932, 2908 (aliph. C-H), 2837 (O-CH_3), 1599, 1505 (ar. C=C), 1296 (C-N), 1241 (C-O-C).

^{1}H NMR (300 MHz, $CDCl_3$-d_6, δ): 3.84 (s, 6H, OCH_3), 3.85 (s, 1H, NH), 6.88 (d, 5H, *J*=9 Hz, ar.), 6.94 (d, 2H, *J*=9 Hz, ar.), 7.11 (d, 5H, *J*=9.3 Hz, ar.), 7.17 (d, 1H, *J*=9 Hz, ar.), 7.29 (t, 2H, *J*=7.8 Hz, ar.), 7.49 (d, 2H, *J*=8.4 Hz, ar.), 7.67 (s, 1H, *J*=8.7 Hz, CH).

MS (APCl$^+$), *m/z* = 501 $[M+H]^+$.

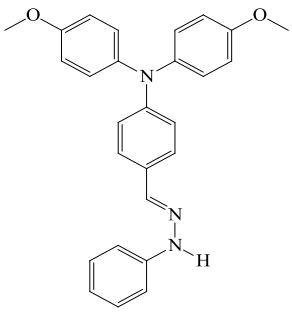

4-(Bis(4-methoxyphenyl)amino)benzaldehyde bis(*N*-methyl-*N*-phenylhydrazone) (12)

Compound **12** was synthesized from *N*-methyl-*N*-phenylhydrazine (0.35 ml, 3 mmol) and aldehyde **10** (0.5 g, 1.5 mmol) by the same procedure as compound **11**. The product was purified by column chromatography using the mixture of ethyl acetate and hexane in a volume ratio of 1:4 as an eluent. The compound **12** was crystallized from the eluent. The yield of yellow crystals was 0.51 g (78%), mp = 133-134 °C.

IR (KBr), cm^{-1}: 3060, 3037 (ar. C-H), 2995, 2956, 2934, 2911 (aliph. C-H), 2835 (O-CH_3), 1606, 1587, 1505 (ar. C=C), 1373 (C=N-N), 1325, 1289 (C-N), 1240 (C-O-C).

^{1}H NMR (300 MHz, $CDCl_3$-d_6, δ): 3,44 (s, 3H, CH3), 3,85 (s, 6H, OCH_3), 6,88 (d, 4H, *J*=8,7 Hz, ar.), 6,94 (s, 1H, ar.), 6,98 (d, 2H, *J*=8,7 Hz, ar.), 7,12 (d, 4H, *J*=9,3 Hz, ar.), 7,30-7,42 (m, 4H, ar.), 7,51 (s, 1H, CH), 7,56 (d, 2H, *J*=9 Hz, ar.).

^{13}C NMR (75 MHz, $CDCl_3$-d_6, δ): 33.27, 55.75, 114.93, 115.22, 120.30, 120.79, 126.85, 127.07, 129.24, 129.41, 132.48, 141.07, 156.13.

MS ($APCl^+$), *m/z* = 439 $[M+H]^+$.

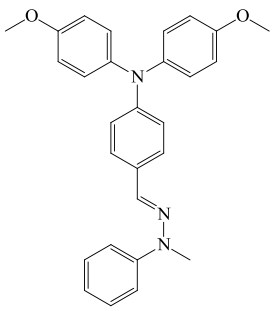

4-(Bis(4-methoxyphenyl)amino)benzaldehyde bis(*N*,*N*-diphenylhydrazone) (13)

Compound **13** was synthesized from *N*,*N*-diphenylhydrazine hydrochloride (0.66 g, 3 mmol) and aldehyde **10** (0.5 g, 1.5 mmol) by the same procedure as compound **11**. The product was purified by column chromatography using the mixture of acetone and hexane in a volume ratio of 1:3 as an eluent. The product **13** was crystallized from the eluent. The yield of yellow crystals was 0.24 g (32%), mp = 17-178 °C.

IR (KBr), cm^{-1}: 3064, 3028, 3005 (ar. C-H), 2958, 2928 (aliph. C-H), 2834 (O-CH_3), 1598, 1504 (ar. C=C), 1386 (C=N-N), 1326, 1294 (C-N), 1240 (C-O-C).

^{1}H NMR (300 MHz, $CDCl_3$-d_6, δ): 3.83 (s, 6H, OCH3), 6.86 (d, 4H, *J*=9 Hz, ar.), 6.92 (d, 2H, *J*=8.7 Hz, ar.), 7.09 (d, 4H, *J*=9.3 Hz, ar.), 7.21 (d, 6H, *J*=7.8 Hz, ar.), 7.29 (s, 1H, CH), 7.45 (t, 6H, *J*=8.1 Hz, ar.).

^{13}C NMR (75 MHz, $CDCl_3$-d_6, δ): 55.75, 114.92, 120.56, 122.73, 124.45, 126.88, 127.33, 128.56, 129.99, 136.24, 140.94, 144.18, 149.07, 156.19.

MS ($APCl^+$), *m/z* = 501 $[M+H]^+$.

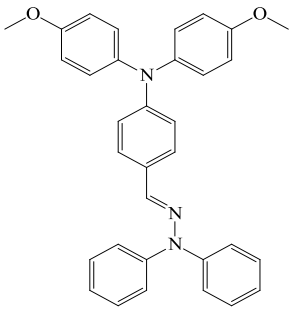

4-(Bis(4-metoxyphenyl)amino)benzaldehyde *N*-4-vinylbenzyl-*N*-phenyl-hydrazone (14)

Hydrazone **11** (1 g, 2.4 mmol) was dissolved in 5 ml of acetone and 1-(chloromethyl)-4-vinylbenzene (0.7 ml, 4.8 mmol) was added dropwise. The reaction mixture was heated to the reflux temperature and tetrabutylamonium hydrosulphate (0.008 g, 0.024 mmol) as well as KOH (0.81 g, 19.5 mmol) were added to the reaction mixture. The later was added in three portions with the interval of 5 minutes. After 30 minutes inorganic components were filtered off and the solvent was removed by distillation. The product was purified by column chromatography at the reduced pressure. The mixture of ethyl acetate and hexane in a volume ratio of 1:5 was used as an eluent. The resin-like crude product was dissolved in diethyl ether and precipitated into methanol. Product **14** was crystallized from methanol. The yield of yellow crystals was 0.6 g (46%), mp 64-66 °C.

IR (KBr), cm^{-1}: 3039 (ar. C-H), 2970, 2933 (aliph. C-H), 2836 (O-CH_3), 1585, 1516, 1484 (ar. C=C), 1387 (C=N-N), 1338 (C-N), 1258 (C-O-C), 1630, 992, 910 (CH=CH_2).

^{1}H NMR (300 MHz, $CDCl_3$-d_6, δ): 3.79 (s, 6H, OCH_3), 5.13 (s, 2H, CH_2), 5.22 (dd, 1H AMX of system CH=$\underline{CH_2}$ proton H^X cis J_{AX}=10.9 Hz), 5.72 (dd, 1H AMX of system CH=$\underline{CH_2}$ proton H^M trans J_{AM}=17.6 Hz ir gem J_{MX}=0.7 Hz), 6.69 (dd, 1H AMX of system $\underline{CH}$=CH_2 proton H^A), 6.81 (d, 4H, *J*=9.1 Hz, ar.), 6.86-6.93 (m, 3H, ar.), 7.04 (d, 4H, *J*=8.7 Hz, ar.), 7.18 (d, 2H, *J*=8.1 Hz, ar.), 7.27 (d, 2H, *J*=9.9 Hz, ar.), 7.31-7.38 (m, 5H, Ar, CH), 7.43 (d, 2H, *J*=8.8 Hz, ar.).

MS ($APCl^+$), *m/z* = 540 $[M+H]^+$.

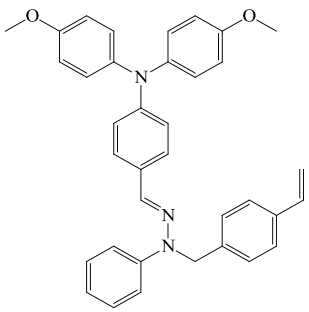

3,3'-(4,5-Diphenyl-1*H*-imidazole-1,2-diyl)bis(9-ethyl-9*H*-carbazole) (15)

A mixture of benzil (1 g, 4.8 mmol), 9-ethyl-9*H*-carbazole-3-carbaldehyde (**CrC**) (1.1 g, 4.8 mmol), 9-ethyl-9*H*-carbazol-3-amine (**CrA**) (1.2 g, 5.7 mmol) and ammonium acetate (3.7 g, 47.6 mmol) in acetic acid (5 ml) was heated at the reflux temperature for 1 h. The mixture was poured into cold water and extracted with chloroform. The organic layer was dried with anhydrous Na_2SO_4, filtered and distilled. The product was purified by column chromatography using the mixture of acetone and hexane in a volume ratio of 1:3 as an eluent. The compound **15** was crystallized from the acetone. The yield of pale yellow crystals was 2.38 g (82%), mp = 264-265 °C.

IR, cm^{-1}: 3055 (ar. C-H), 2978 (aliph. C-H), 1599, 1470, 1444 (ar. C=C), 1332, 1230 (C-N).

^{1}H NMR (400 MHz, $CDCl_3$-d_6, δ): 1.26 (t, *J*=7.2 Hz, 3H, CH_3), 1.34 (t, *J*=7.2 Hz, 3H, CH_3), 4.17 (q, *J*=7.2 Hz, 2H, CH_2), 4.25 (q, *J*=7.2 Hz, 2H, CH_2), 7.02-7.10 (m, 5H, ar.), 7.12-7.18 (m, 5H, ar.), 7.20-7.26 (m, 4H, ar.), 7.30-7.33 (m 2H, ar.), 7.37-7.44 (m, 2H, ar.), 7.62 (d, *J*=7.3 Hz, 2H, ar.), 7.76-7.78 (m, 2H, ar.), 7.84 (d, *J*=7.8 Hz, 1H, ar.), 8.28 (d, *J*=1.3 Hz, 1H, ar.).

MS ($APCl^+$), *m/z* = 608 $[M+H]^+$.

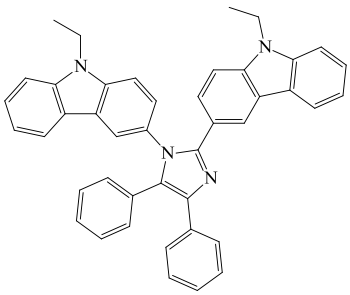

6,6'-(4,5-Diphenyl-1*H*-imidazole-1,2-diyl)bis(3-(tert-butyl)-9-ethyl-9*H*-carbazole) (16)

A solution of compound **15** (1 g, 1.7 mmol) and $AlCl_3$ (0.8 g, 6.6 mmol) in dichloromethane (10 ml) was cooled down using ice-bath. To the reaction mixture solution of *tert*-butyl chloride (0.4 ml, 3.6 mmol) in dichloromethane (5ml) was added dropwise. The mixture was stirred at room temperature for 1 h then poured into water and extracted with chloroform. The organic layer was dried with anhydrous Na_2SO_4, filtered and distilled. Product was purified by column chromatography using the mixture of acetone and hexane in a volume ratio of 1:6 as an eluent. The yield of pale yellow solid was 0.82 g (69%).

IR, cm^{-1}: 3053 (ar. C-H), 2963 (aliph. C-H), 1604, 1481 (ar. C=C), 1301, 1232 (C-N).

^{1}H NMR (400 MHz, DMSO-d_6, δ): 1.18-1.38 (m, 24H, CH_3), 4.25-4.43 (m, 4H, CH_2), 7.16-7.31 (m, 6H, ar.), 7.33-7.42 (m, 4H, ar.), 7.45-7.49 (m 2H, ar.), 7.50-7.56 (m, 3H, ar.), 7.57-7.60 (m, 2H, ar.), 7.68-7.76 (m, 1H, ar.), 7.94-8.05 (m, 1H, ar.), 8.10-8.13 (m, 1H, ar.), 8.20-8.34 (m, 2H, ar.).

MS (APCl$^+$), *m/z* = 720 [M+H]$^+$.

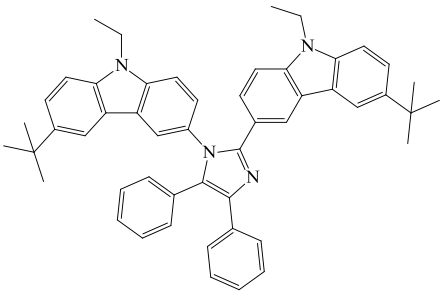

9-(2-Ethylhexyl)-9*H*-carbazole (17)

Compound **17** was synthesized according to the procedure described in literature [128].

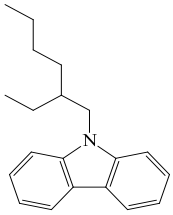

9-(2-Ethylhexyl)-9*H*-carbazole-3,6-diamine (18)

Compound was synthesized from compound **17** according to the procedure described in literature [129].

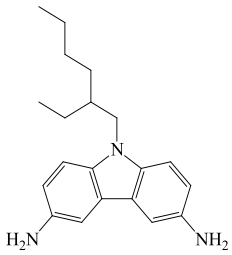

3,3'-(1,1'-(9-(2-Ethylhexyl)-9*H*-carbazole-3,6-diyl)bis(4,5-diphenyl-1*H*-imidazole-2,1-diyl))bis(9-ethyl-9*H*-carbazole) (19)

Compound **19** was synthesized from benzil (1.35 g, 6.4 mmol), 9-ethyl-9*H*-carbazole-3-carbaldehyde (**CrC**) (1.59 g, 7.1 mmol), diaminocarbazole **18** (1 g, 3.2 mmol) and ammonium acetate (4.98 g, 64.6 mmol) by the same procedure as compound **15**. The product was purified by column chromatography using the mixture of acetone and hexane in a volume ratio of 1:4 as an eluent. The yield of white solid was 2.63 g (74%).

IR, cm^{-1}: 3054 (ar. C-H), 2932 (aliph. C-H), 1602, 1475 (ar. C=C), 1333, 1231 (C-N).

^{1}H NMR (400 MHz, DMSO-d_6, δ): 0.58 (t, *J*=7.0 Hz, 3H, CH_3), 0.74 (t, *J*=7.4 Hz, 3H, CH_3), 0.91-0.97 (m, 3H, CH_3), 1.13-1.25 (m, 11H, CH_2, CH_3), 1.86-1.88 (m, 1H, CH), 4.19 (d, *J*=7.2 Hz, 2H, CH_2), 4.25-4.40 (m, 4H, CH_2), 6.97-7.11 (m, 4H, Ar), 7.16-7.20 (m, 3H, ar.), 7.24-7.28 (m, 10H, ar.), 7.40-7.41 (m, 6H, ar.), 7.50-7.56 (m, 11H, ar.), 7.75 (d, *J*=6.3 Hz, 2H, ar.), 8.18 (d, *J*=16.4 Hz, 4H, ar.).

MS (APCl$^+$), *m/z* = 1103 $[M+H]^+$.

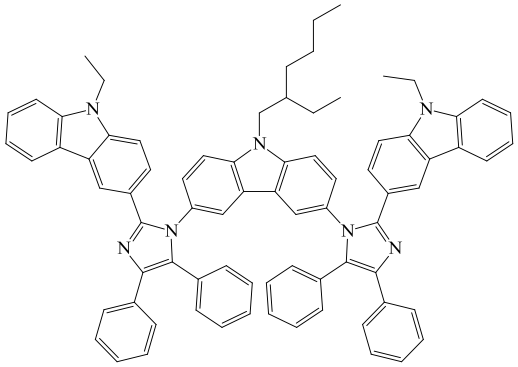

6,6'-(1,1'-(9-(2-Ethylhexyl)-9*H*-carbazole-3,6-diyl)bis(4,5-diphenyl-1*H*-imidazole-2,1-diyl))bis(3-(tert-butyl)-9-ethyl-9*H*-carbazole) (20)

Compound **20** was synthesized from compound **19** (1 g, 0.9 mmol), $AlCl_3$ (0.48 g, 3.6 mmol) and *tert*-butyl chloride (0.22 ml, 2 mmol) by the same procedure as compound **16**. The product was purified by column chromatography using the mixture of acetone and hexane in a volume ratio of 1:5 as an eluent. The yield of pale yellow solid was 0.62 g (57%).

IR, cm^{-1}: 3052 (ar. C-H), 2958 (aliph. C-H), 1605, 1480 (ar. C=C), 1300, 1234 (C-N).

^{1}H NMR (400 MHz, DMSO-d_6, δ): 0.54 (t, *J*=7.0 Hz, 3H, CH_3), 0.77 (t, *J*=7.4 Hz, 3H, CH_3), 0.93-0.96 (m, 3H, CH_3), 1.10-1.27 (m, 29 H, CH_2, CH_3), 1.82-1.88 (m, 1H, CH), 4.19 (d, *J*=7.2 Hz, 2H, CH_2), 4.25-4.40 (m, 4H, CH_2), 6.88-7.07 (m, 2H, ar.), 7.16-7.35 (m, 18H, ar.), 7.41-7.55 (m, 14H, ar.), 7.83 (s, 2H, ar.), 8.12 (d, 2H, *J*=1.6 Hz, ar.).

MS (APCl$^+$), *m/z* = 1216 $[M+H]^+$.

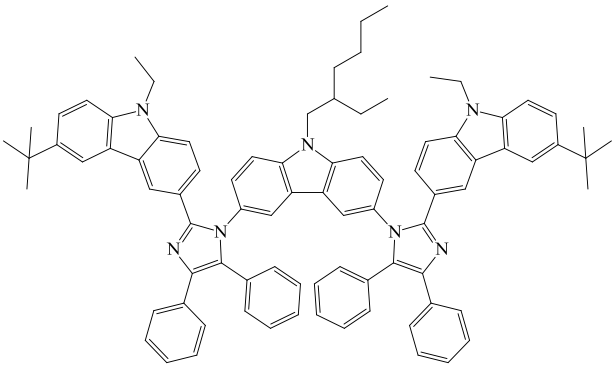

Bis(4-(diphenylamino)phenyl)methanone (21)

Compound **21** was synthesized according to the procedure described in literature [130].

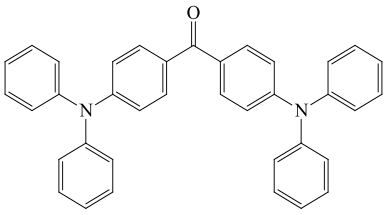

Bis(4-(bis(4-methoxyphenyl)amino)phenyl)methanone (22)

4,4'-Diaminobenzophenone (2 g, 9.4 mmol) was dissolved in *o*-dichlorbenzene (20 ml) with 4-iodanisole (13.2 g, 56.5 mmol). Cu powder (2.4 g, 37.7 mmol), 18-crown-6 (0.5 g, 1.9 mmol) and K_2CO_3 (10.4 g, 75.4 mmol) were added to the solution. The reaction mixture was stirred at 180 ºC under argon atmosphere. After 24 h the inorganic components were removed by filtration of the hot mixture. The solvent was removed by distillation under reduced pressure. The compound was purified by column chromatography using ethyl acetate and hexane in a volume ratio of 1:3 as an eluent. The yield of yellow solid was 4.8 g (81%).

IR (KBr), cm^{-1}: 3040 (ar. C-H), 2997, 2952, 2931 (aliph. C-H), 2833 (O-CH_3), 1593, 1505, 1440 (ar. C=C), 1643 (C=O), 1286, 1272, 1271 (C-N), 1243 (C-O-C).

^{1}H NMR (300 MHz, $CDCl_3$-d_6, δ): 3.81 (s, 12H, OCH_3), 6.83-6.88 (m, 12H, ar.), 7.12 (d, 8H, *J*=9.16, ar.), 7.63 (d, 4H, *J*=9.16, ar.).

^{13}C NMR (75 MHz, $CDCl_3$-d_6, δ): 55.47, 114.87, 117.04, 127.66, 129.09, 131.65, 139.53, 151.98, 152.00, 156.74, 193.76.

MS ($APCl^+$), *m/z* =637 $[M]^+$.

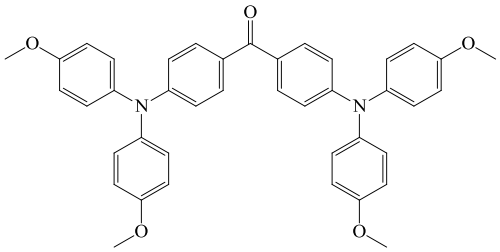

Bis(4-(bis(4-methylphenyl)amino)phenyl)methanone (23)

Compound **23** was synthesized from 4,4'-diaminobenzophenone (2 g, 9.4 mmol), 4-iodotoluene (12.3 g, 56.5 mmol), Cu powder (2.4 g, 37.7 mmol), 18-crown-6 (0.5 g, 1.9 mmol) and K_2CO_3 (10.4 g, 75.4 mmol) by the same procedure as compound **22**. The product was purified by column chromatography using tetrahydrofuran and hexane in a volume ratio of 1:6 as an eluent. The yield of yellow solid was 3.8 g (72%).

IR (KBr), cm^{-1}: 3058, 3025 (ar. C-H), 2945, 2919, 2860 (aliph. C-H), 1594, 1507 (ar. C=C), 1647 (C=O), 1318, 1294, 1276 (C-N).

^{1}H NMR (300 MHz, $CDCl_3$-*d*$_6$, δ): 2.33 (s, 12H, CH_3), 6.94 (d, 4H, *J*=8.74, ar.), 7.04-7.13 (m, 16H, ar.), 7.64 (d, 4H, *J*=8.73, ar.).

^{13}C NMR (75 MHz, $CDCl_3$-*d*$_6$, δ): 21.18, 118.99, 126.17, 130.11, 130.42, 131.82, 134.42, 144.38, 151.90, 194.13.

MS (APCl$^+$), *m/z* =573 $[M]^+$.

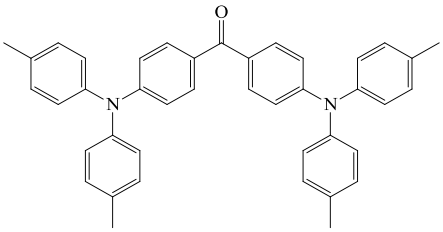

4,4'-(2-Phenylethene-1,1-diyl)bis(*N*,*N*-diphenylaniline) (24)

Compound was synthesized from ketone **21** according to the procedure described in the literature [130], mp = 154-155 °C.

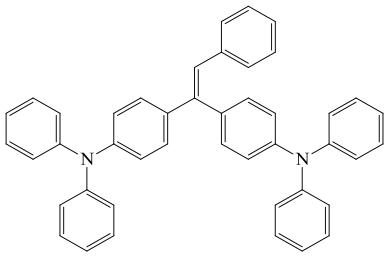

4,4'-(2-Phenylethene-1,1-diyl)bis(*N*,*N*-bis(4-methoxyphenyl)aniline) (25)

Ketone **22** (1 g, 1.8 mmol) and diethyl benzylphosphonate (0.75 ml, 3.6 mmol) were dissolved in anhydrous tetrahydrofuran. Potassium *tert*-butoxide (0.81 g, 7.2 mmol) was added slowly to the solution at room temperature under argon atmosphere. The reaction mixture was stirred for 1 h. After the reaction the mixture was diluted with water and extracted with ethyl acetate. The organic layer was dried over anhydrous Na_2SO_4. The solvent was removed by distillation. The product was purified by column chromatography using acetone and hexane in a volume ratio of 1:8 as an eluent. The compound **25** was crystallized from eluent. The yield of yellow crystals was 0.6 g (55%), mp = 176-177 °C.

IR (KBr), cm^{-1}: 3038, 3007 (ar. C-H), 2943, 2929, 2900 (aliph. C-H), 2832 (O-CH_3), 1598, 1505, 1461, 1442 (ar. C=C), 1319, 1278 (C-N), 1239 (C-O-C).

^{1}H NMR (300 MHz, $CDCl_3$-*d*$_6$, δ): 3.79 (s, 12H, OCH_3), 6.81-6.88 (m, 13H, Ar), 6.99 (d, 2H, *J*=8.71, ar.), 7.05-7.08 (m, 10H, ar.), 7.13-7.20 (m, 5H, ar.).

^{13}C NMR (75 MHz, $CDCl_3$-*d*$_6$, δ): 55.75, 114.90, 114.92, 120.08, 120.80, 125.65, 126.36, 126.71, 126.89, 128.08, 128.44, 129.66, 131.13, 132.61, 135.67, 138.42, 141.07, 141.23, 148.06, 155.96, 156.12.

MS (APCl$^+$), *m/z* =711 $[M]^+$.

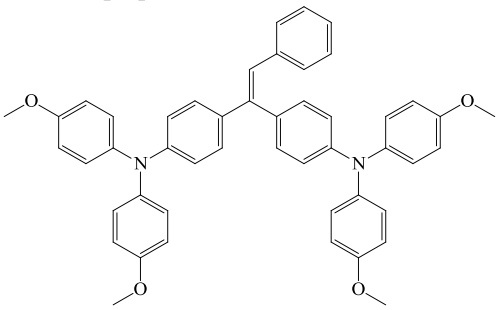

4,4'-(2-(4-Methoxyphenyl)ethene-1,1-diyl)bis(*N*,*N*-bis(4-methoxyphenyl) aniline) (26)

Compound **26** was synthesized from ketone **22** (1 g, 1.8 mmol) and diethyl 4-methoxybenzylphosphonate (0.55 ml, 3.6 mmol) and potassium *tert*-butoxide (0.81 g, 7.2 mmol) by the same procedure as compound **25**. The product was purified by column chromatography using ethyl acetate and hexane in a volume ratio of 1:8 as an eluent. The yield of yellow solid was 0.6 g (52 %).

IR (KBr), cm^{-1}: 3035 (ar. C-H), 2997, 2950, 2931, 2905 (aliph. C-H), 2833 (O-CH_3), 1605, 1505, 1463, 1440 (ar. C=C), 1318, 1283 (C-N), 1240 (C-O-C).

^{1}H NMR (400 MHz, $CDCl_3$-*d*$_6$, δ): 3.81 (s, 3H, OCH_3), 3.82 (s, 12H, OCH_3), 6.73 (d, 2H, *J*=8.77, ar.), 6.80 (s, 1H, CH), 6.84-6.92 (m, 12H, ar.), 7.02-7.05 (m, 4H, ar.), 7.08-7.11 (m, 8H, ar.), 7.19 (d, 2H, *J*=8.72, ar.).

^{13}C NMR (101 MHz, $CDCl_3$-*d*$_6$, δ): 55.21, 55.51, 113.31, 114.65, 120.00, 120.67, 125.02, 126.46, 126.58, 127.97, 130.61, 130.88, 131.08, 135.72, 140.23, 140.90, 141.01, 147.67, 147.92, 155.70, 155.81, 157.93.

MS (APCl$^+$), *m/z* =741 $[M]^+$.

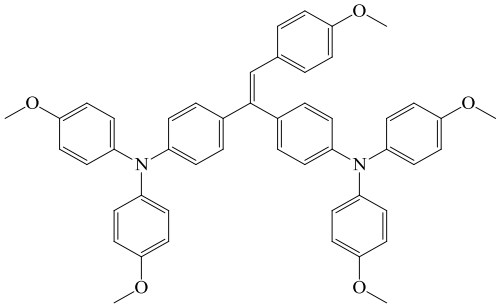

4,4'-(2-Phenylethene-1,1-diyl)bis(*N*,*N*-bis(4-methylphenyl)aniline) (27)

Compound **27** was synthesized from ketone **23** (1 g, 1.6 mmol) and diethyl benzylphosphonate (0.67 ml, 3.2 mmol) and potassium *tert*-butoxide (0.72 g, 6.4 mmol) by the same procedure as compound **25**. The product was purified by column chromatography using ethyl acetate and hexane in a volume ratio of 1:20 as an eluent. The yield of yellow solid was 0.4 g (39%).

IR (KBr), cm^{-1}: 3059, 3027 (ar. C-H), 2952, 2920, 2855 (aliph. C-H), 1594, 1502 (ar. C=C), 1322, 1275 (C-N).

^{1}H NMR (300 MHz, $CDCl_3$-d_6, δ): 2.32 (s, 12H, CH_3), 6.86 (s, 1H, CH), 6.95-7.10 (m, 22H, ar.), 7.12-7.25 (m, 7H, ar.).

^{13}C NMR (101 MHz, $CDCl_3$-d_6, δ): 20.81, 121.74, 122.61, 124.55, 124.78, 125.93, 126.25, 127.83, 128.19, 129.46, 129.84, 129.88, 131.16, 132.65, 133.48, 136.28, 138.04, 142.05, 145.16, 145.28, 147.26, 147.70.

MS ($APCl^+$), *m/z* =647 $[M]^+$.

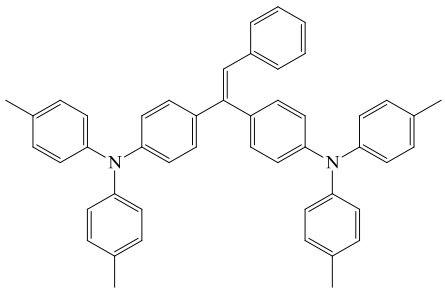

4,4'-(2-(4-Methylphenyl)ethene-1,1-diyl)bis(*N*,*N*-bis(4-methylphenyl) aniline) (28)

Compound **28** was synthesized from ketone **23** (1 g, 1.6 mmol), diethyl 4-methylbenzylphosphonate (0.72 ml, 3.2 mmol) and potassium *tert*-butoxide (0.72 g, 6.4 mmol) by the same procedure as compound **25**. The product was purified by column chromatography using ethyl acetate and hexane in a volume ratio of 1:20 as an eluent. The yield of yellow solid was 0.5 g (40 %).

IR (KBr), cm^{-1}: 3078, 3058, 3026 (ar. C-H), 2951, 2919, 2856 (aliph. C-H), 1592, 1506 (ar. C=C), 1321, 1272 (C-N).

^{1}H NMR (300 MHz, $CDCl_3$-*d_6*, δ): 2.29, (s, 3H, CH_3), 2.31 (s, 12H, CH_3), 6.82 (s, 1H, CH), 6.93-7.08 (m, 26H, ar.), 7.21 (d, 2H, *J*=8.73 Hz, ar).

^{13}C NMR (75 MHz, $CDCl_3$-*d_6*, δ):.21.08, 21.46, 122.09, 122.95, 124.78, 124.98, 126.19, 128.33, 128.86, 129.62, 130.10, 130.12, 131.38, 132.63, 132.83, 135.98, 135.37, 136.29, 136.72, 141.36, 145.43, 145.56, 147.48, 147.78. MS ($APCl^+$), *m/z* =661 $[M]^+$.

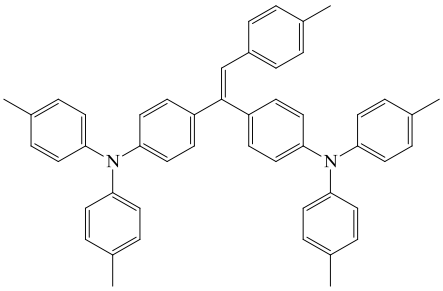

4. RESULTS AND DISCUSSION

4.1. Carbazole dyes with cyano groups

The anchor group in organic sensitizers often consist of a cyano-acrylic acid unit. The acrylic acid group allows the dye to chemically bind to the TiO_2 surface. However, several investigations reveal that dye-TiO_2 complex can be formed by nucleophilic reaction of cyano group of dye molecule with hydroxyl group of the TiO_2 nanoparticles. [131,132,133] Carbazole-based compounds having two or four cyano groups were synthesized, because of a lack of information about dyes containing this type of anchor groups. Conjugated double bond linker was chosen to improve electronic communication between carbazole and cyano moieties. [134] Based on compounds described in literature review, hexyl group was used to decrease the dye aggregation on TiO_2 surface and reduce interfacial charge recombination losses.

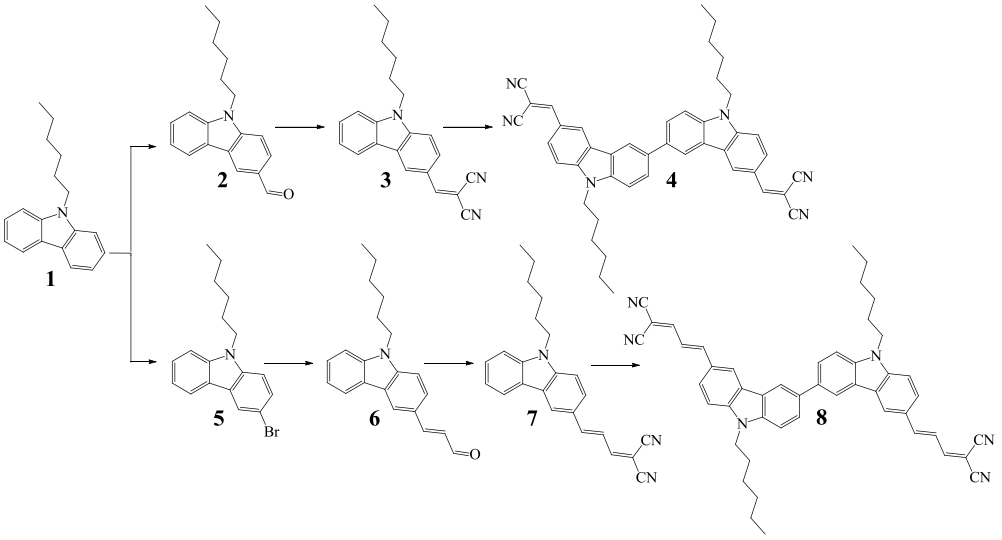

Scheme 3. Synthesis of carbazole derivatives with cyano groups

The synthetic routes to carbazole derivatives having cyano groups are shown in **Scheme 3**. Synthesized compounds **3**,**4** differ from **7**,**8** in π-conjugation length of linker between carbazole unit and cyano groups. At first step carbazole was alkylated with bromohexane to give compound 9-hexyl-9*H*-carbazole (**1**). Compound **1** was used for formylation by Vilsmeier-Haack method [135] to obtain aldehyde **2** and bromination to get compound **5**. At next step palladium catalyzed coupling [136] of carbazole derivative **5** with acrolein diethyl acetal resulted in formation of compound **6**. Condensation of the aldehydes **2** and **6** with malononitrile yield compounds **3** and **7**, respectively. Derivatives **4** and **8** with two carbazole units were prepared by oxidative dimerization of compounds **3** and **7** by $FeCl_3$ [137].

4.1.1. Thermal properties

The thermal behaviour of synthesized dyes **3**,**4** and **7**,**8** was investigated by DSC, results are presented in **Table 1**. Compounds were isolated as crystalline materials. They showed endothermic melting signals during the first heating scans.

Table 1. Thermal characteristics of carbazole dyes **3**,**4**, and **7**,**8**

Compound	T_m	T_g	T_{cr}
3	122	-	52
4	251, 242[a]	90	183
7	128	18	94
8	273	109	215

[a] second heating scan

Dyes **3** and **7** having one carbazole moiety don't form amorphous layers, their T_g are lower than room temperature. Furthermore, these compounds have tendency to crystalize under low temperature. During the second heating scans T_{cr} at 52 °C and 94 °C was observed for **3** and **7**, respectively. In case of compounds **4** and **8**, the temperatures studied in DSC experiment significantly increase. (**Figure 1a,b**) During first heating scan dyes **4** and **8** reveal T_m at 251 °C and 273 °C, respectively. In the cooling scans no crystallization were observed and the second heating revealed glass transition. The extension of length of π-linker increases T_g from 90 °C (**4)** to 109 °C (**8)**. The further heating of the samples revealed crystallization and melting. Compound **4** showed tendency to form different crystal structures. In the second heating it showed lower T_m at 242 °C.

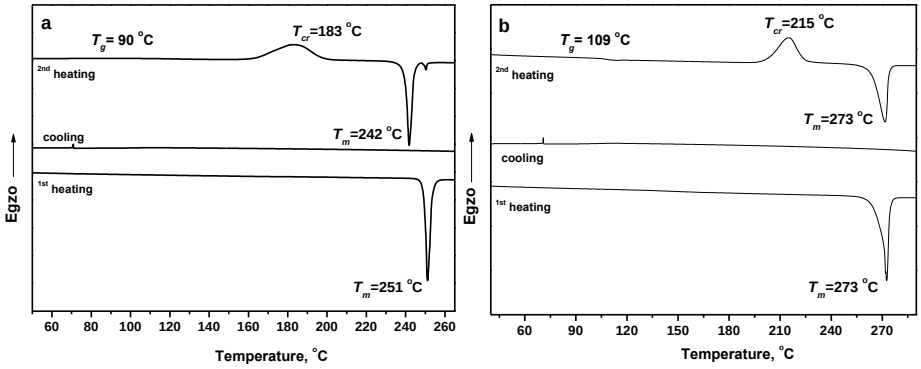

Figure 1. DSC curves of compounds **4** (**a**) and **8** (**b**)

4.1.2. Geometrical structures and frontier orbitals

The theoretical calculations of the geometry of dyes **3**,**4** and **7**,**8** showed that the carbazole fragment and the cyano groups are in one plane, while dihedral angle

between two carbazole moieties in compounds **4** and **8** is 39°. The theoretical geometry of compound **8** is presented in **Figure 2**.

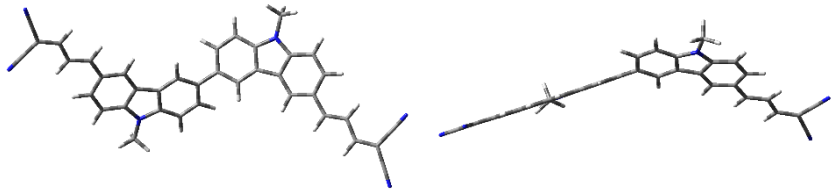

Figure 2. The theoretical geometrical structure of compound **8** calculated at B3LYP/6-31G(d,p) level

The calculated HOMO and LUMO energies of optimized structures of synthesized dyes are shown in **Figure 3**. The HOMO of all dyes are distributed on the whole molecular backbones. However, the LUMO is localized essentially on the acceptor group and π-linker, with less contribution from the carbazole unit. In DSSC devices, the LUMO level of the dye must be located above the semiconductor conduction band for effective electron injection, while the HOMO should be located under the oxidation potential of HTM for efficient regeneration of the oxidized dye. The LUMO of synthesized compounds **3**,**4** and **7**,**8** are ranging from -2.81 eV to -2.45 eV and HOMO of dyes are located in the range from -6.00 eV to -5.72 eV. The theoretical valence and conduction band values of TiO_2 [138], calculated ionization potential of spiro-MeOTAD [139] are shown in **Figure 3**.

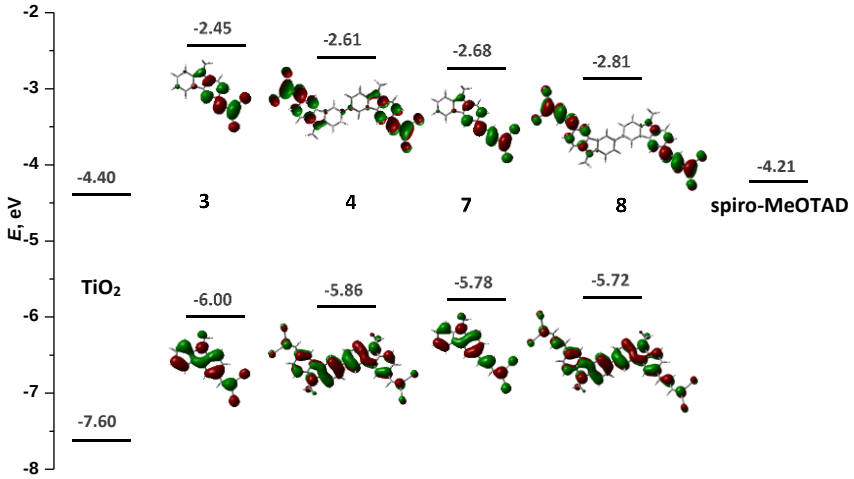

Figure 3. The energy levels distribution of DSSC components and molecular orbital of synthesized dyes **3**,**4**, and **7**,**8** (B3LYP/6-31G(d,p) level)

4.1.3. Optical properties and geometry

The absorption and fluorescence emission spectra recorded for the solid films of the synthesized dyes **3**,**4** and **7**,**8** are shown in **Figure 4a,b**.

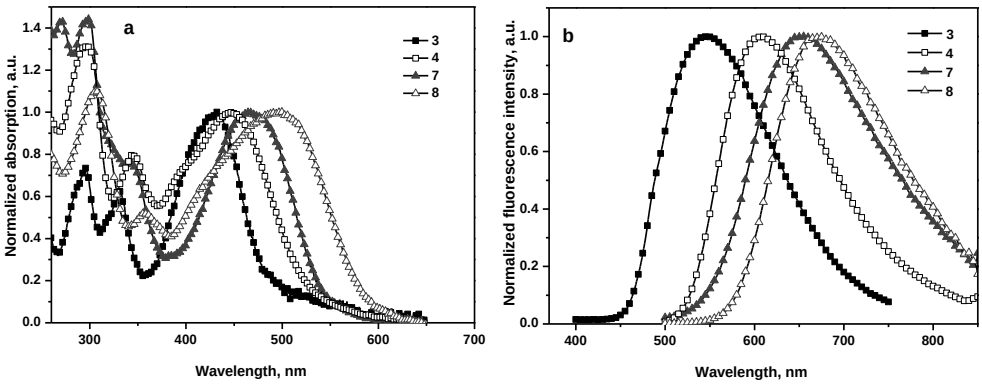

Figure 4. Absorption (**a**) and steady-state fluorescence emission (**b**) spectra of films of dyes **3**,**4**, and **7**,**8** (λ_{ex}=330 nm)

The structure of dyes ensures absorption in visible region up to 650 nm. The absorption peaks in the range from 296 nm to 359 nm can be attributed to the transitions between various molecular orbitals except transition from HOMO to LUMO. Most intensive transitions in the theoretical absorption spectra of compounds **3**,**4** and **7**,**8** are presented in **Figure 5**.

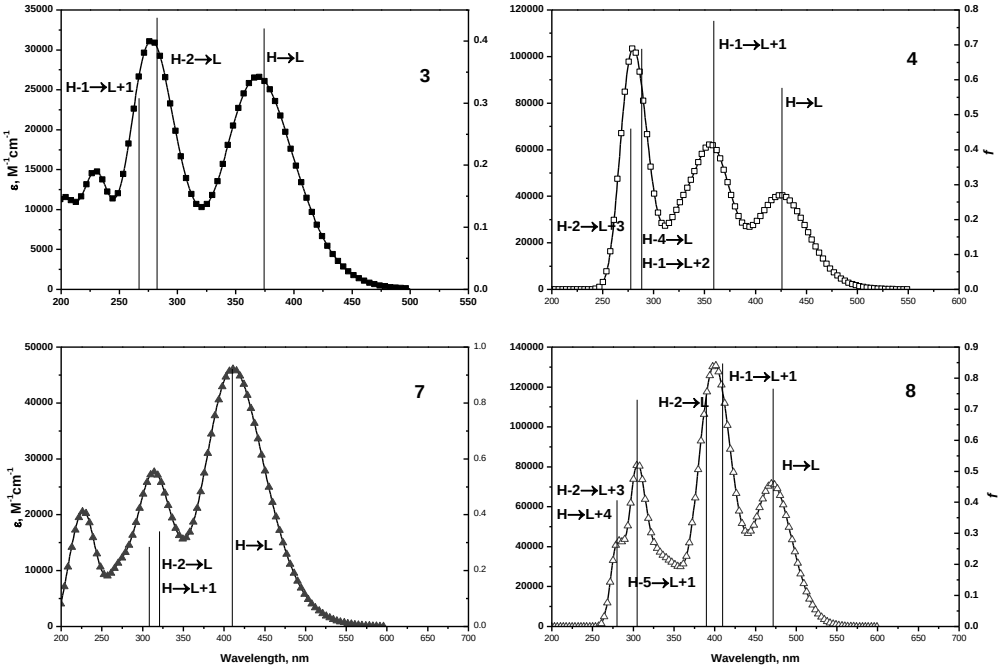

Figure 5. Theoretical absorption spectra of dyes **3**,**4**, and **7**,**8** in gas phase

The experimental and theoretical optical results of the dyes are summarized in **Table 2**. The lowest transition from ground state to first excited state ($S_0 \rightarrow S_1$) in dyes correspond to transition from HOMO to LUMO which can be characterized as

intramolecular charge transfer (ICT) between the carbazole donor part of the molecule and the cyano acceptor group.

Table 2. Optical characteristics of compounds **3**, **4**, and **7**,**8**

Compound	Electron transition	λ [a], nm	*f* [b]	*p* [c], D	Main transition configuration (%)	λ_{ab} [d], nm	λ_{fl} [e], nm	Stokes shift [f], nm
3	$S_0 \rightarrow S_1$	374	0.4203	9.9	H→L (79%)	432	546	114
4	$S_0 \rightarrow S_1$	425	0.5775	6.2	H→L (97%)	446	607	161
7	$S_0 \rightarrow S_1$	410	0.9218	11.4	H→L (91%)	468	652	184
8	$S_0 \rightarrow S_1$	471	0.7666	6.9	H→L (97%)	499	673	174

[a] theoretical lowest energy band of absorption and [b] oscillator strength (gas phase); [c] theoretical dipole moment in the ground state; [d] experimental lowest energy band of absorption; [e] experimental maximum band of fluorescence emission; [d] difference between λ_{fl} and λ_{ab}.

The lowest energy absorption bands of compounds **7** and **8** are red shifted in comparison with that of **3** and **4** due to the expansion of π-conjugated system by introducing the methine moiety into the π-linker. This effect is also visible from the evolution of the HOMO and LUMO levels in **Figure 3**. It has been noticed that the experimental and theoretical lowest energy bands of dyes **4** and **7** have different trend. This could be due the band gaps, *i.e.*, the difference between HOMO and LUMO energy levels, of compounds. The band gaps decrease consistently in the order **3** > **4** > **7** > **8** (3.55 eV > 3.25 eV > 3.10 eV > 2.91 eV). The lower band gap value of dye **7** comparing that with dye **4** leads to the bathochromic shift of the experimental lowest energy absorption band of compound **7** (**Figure 4a**).

Charge injection or photoexcitation process is usually followed by geometry relaxation of π-conjugated systems and solvent (medium) relaxation. [140] After relaxation, the molecular geometry of the optimized first singlet excited state (S_1) may be remarkably different from the optimized ground state geometry (S_0). The medium relaxation in the films of these compounds depends on the medium polarity in correlation with the difference between the dipole moments in the ground state and in the excited state. The cumulated effect of intramolecular and solvent relaxations can be characterized by Stokes shift, which corresponds to the difference between positions of band maxima of the absorption and fluorescence emission spectra. [141,142] Fluorescence emission spectra (**Figure 4b**) of the synthesized **3**,**4** and **7**,**8** are broad and considerably red-shifted with respect to the corresponding absorption spectra. Synthesized dyes exhibit yellow, orange and red fluorescence when are excited with UV irradiation. The large Stokes shifts ranging from 114 to 184 nm may originate from the ICT occurring in these compounds and effective π-conjugation [143]. These factors cause large geometry relaxation of molecules upon photoexcitation. ICT from carbazole moiety to cyano groups show Stokes shift of 114 nm for **3**. In the case of compound **7**, expansion of π-conjugated system in the linker leads to increased dipole moment at ground state (from 9.9 to 11.4 respectively), therefore resulting in increased medium polarity and relaxation. The collective effect of the intramolecular and medium relaxations may explain the strong increase in Stokes shift by 70 nm. In the dimers **4** and **8** the HOMO is mainly

localized on the carbazole moieties, therefore, the length of π-linker has lower influence on the Stoke shifts, suggesting smaller evolution of intramolecular relaxation between **4** and **8** as compared to that between **3** and **7**. Additionally, the dipole moment at ground state difference between **4** and **8** (0.7 D) is two times smaller than between **3** and **7** (1.5 D). This last effect in conjunction with the smaller polarity in these compounds suggest smaller contribution from the medium relaxation in the case of compounds **4** and **8**. Indeed, spectra of dyes **4** and **8** reveal Stokes shifts of 161 nm and 174 nm, respectively, exhibiting consequently smaller evolution (13 nm).

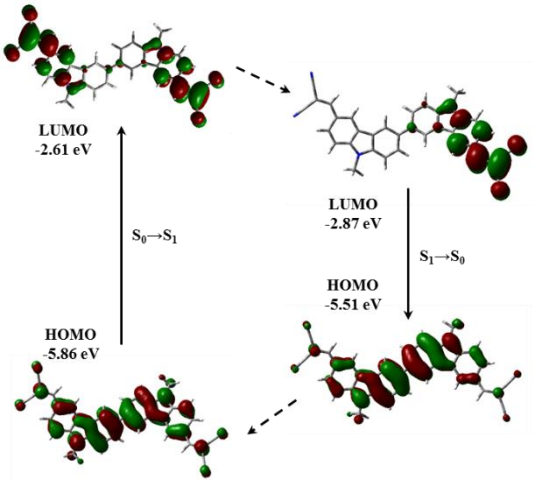

Figure 6. Molecular orbitals of compound **4** at ground and excited states (B3LYP/6-31G(d,p) level)

The cyano groups and π-linker in all synthesized dyes are arranged coplanar with carbazole moiety indicating a strong conjugation effect and favourable electron transition from donor to acceptor. However, two carbazole moieties of dyes **4** and **8** are rotated relative to each other with dihedral angle of 39°. Noticeable changes in geometry at S_1 compare with S_0 state can be observed in dye molecules upon photoexcitation. The dihedral angle between two carbazole units of **4** and **8** decrease to 23° and the single bond length between them reduces from 1.49 Å to 1.45 Å. The important impact of these geometrical modifications can be seen in **Figure 6** showing the frontier orbitals of compound **4** in the ground- and excited states. The energy gap between HOMO and LUMO is shown to decrease with geometry relaxation at the S_1 state compared to that at S_0 state geometry, which is mainly due to the increased conjugation efficiency (reduced dihedral angle) between two carbazole moieties. This effect is absent in the case of compound **3**, which can explain the smallest Stokes shift (114 nm) exhibited by this compound. However, a similar comment does not apply in the case of compound **7** exhibiting the largest Stokes shift (184 nm), thus pointing to the impact of medium relaxations.

4.1.4. Electrochemical and photoelectrical properties

Electrochemical investigation of the solutions of compounds **3**,**4** and **7**,**8** in dichloromethane were carried out in order to elucidate the values of EA_{CV} and IP_{CV}. All the synthesized dyes exhibit irreversible reduction processes corresponding to the reduction of cyano groups and quasi-reversible oxidation of carbazole fragments (**Figure 7**).

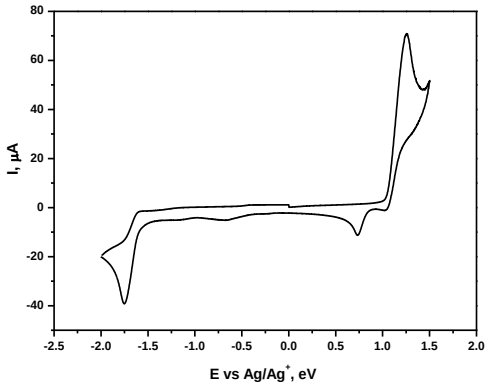

Figure 7. Cyclic voltammogram of compound **3**

The CV results, theoretical adiabatic IP, HOMO, LUMO and IP_{PE} determined from layers of compounds are presented in **Table 3**.

Table 3. Values of electron affinity, ionization potentials and HOMO/LUMO energies of dyes **3**,**4** and **7**,**8**

Compound	EA_{CV} [a], eV	IP_{CV} [a], eV	LUMO [c], eV	HOMO [c], eV	IP [b], eV	IP_{PE} [c], eV
3	3.03	5.69	-2.45	-6.00	7.37	5.80
4	3.12	5.43	-2.61	-5.86	6.80	5.50
7	3.29	5.57	-2.68	-5.78	7.01	5.63
8	3.33	5.38	-2.81	-5.72	6.60	5.25

[a] determined by cyclic voltamperometry; [b] calculated theoretical at B3LYP/6-31G(d,p) level; [c] measured by photoemission in air method.

EA_{CV} and IP_{CV} were calculated from onset values of first reduction and oxidation processes after calibration against Fc/Fc^+. The EA_{CV} values are ranging from 3.03 eV to 3.33 eV. Compound **3** exhibits largest EA_{CV} and **8** shows smallest one. The IP_{CV} are in range 5.38-5.69 eV. The dimers **4** and **8** present smaller IP_{CV} values comparing those with their counterparts **3** and **7**. Incorporation of methine unit in to the π-linker leads to a decrease of IP_{CV}. The trends of EA_{CV} and IP_{CV} are globally consistent with the trend of LUMO and HOMO energies, respectively, except for a discontinuity in the case of experimental values for compound **7**. The globally decreasing ionization potentials and increasing electron affinities could be explained by the increases of π-conjugated system in molecules, whereas the

difference between IP_{CV} and IP_{PE} is apparently due to the different environments in dilute solution and solid layers of synthesized dyes.

4.1.5. Intermolecular charge transfer

The basic working scheme of a DSSC device is shown in **Scheme 4**. Firstly, the dye is excited by absorbing the photon and rapidly injects an electron in to the conduction band of semiconductor. The next dye is regenerated by electron transfer from the HTM.

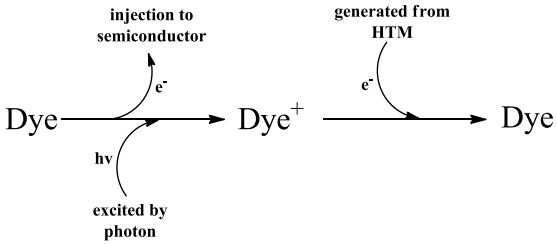

Scheme 4. Schematic illustration of electron transfer processes in DSSC

The intermolecular charge transfer HTM→dye can be treated theoretically within the context of the Marcus theory [144,145,146]:

$$k_{CT} = \frac{4\pi}{\hbar}\frac{1}{\sqrt{4\pi\lambda k_B T}}t^2 exp\left(-\frac{(\Delta G°+\lambda)^2}{4\lambda k_B T}\right); \quad (1)$$

Where k_B - the Boltzmann constant, ħ - Planck's constant, T - the temperature, ΔG° is the Gibbs free enthalpy of reaction, and λ is reorganization energy. The λ consist of two components λ_D and λ_{HTM}, which are associated with change in molecular geometry of dye and HTM, respectively, caused by charge transfer. According to **Equation 1** and assuming that the system corresponds to the normal Marcus region, smaller λ values will enhance intermolecular charge transfer rate. While working in the normal Marcus region seems a reasonable assumption for the charge transport between like molecules, caution should be paid in the case of HTM→Dye electron transfer. In this case, knowledge of ΔG° is necessary, as it is the sum (ΔG°+λ) that needs to be minimized in order to achieve maximum dye regeneration rate.

In the following section we will focus on the trends of the intramolecular reorganization energy only. The λ_D for synthesized dyes was calculated at the potential surface of the neutral species as shown in **Equation 2**.

$$\lambda_D = E_M^{geom(M^+)} - E_M^{geom(M)}; \quad (2)$$

In this equation the components correspond to the energy of neutral molecule species (E_M) in cationic (M^+) and neutral (M) state geometry. The calculated values of λ_D are presented in **Table 4**.

Table 4. Reorganization energies and hole mobilities of compounds **3**,**4** and **7**,**8**

Compound	**3**	**4**	**7**	**8**
λ_D, eV	0.044	0.145	0.081	0.080
μ_h[a], cm^2/Vs	-	$3.44\cdot10^{-6}$	$1.72\cdot10^{-5}$	$1.84\cdot10^{-5}$

[a] hole mobility at an electric field of $6.4\cdot10^5$ cm^2/Vs

In order to understand the trend of these values, we try to point out the geometrical parameters which variations dominate the λ_D values. Indeed, the geometrical structures of the oxidized dyes **3**,**4** and **7**,**8** are strongly affected when an electron is added to their singly occupied molecular orbital (SOMO). The reorganization energy upon regeneration of the dye is thus correlated with the amount of geometrical modifications. As a means to evaluate these geometrical deformations for each compound, the difference between the bonds length in π-conjugated backbone of neutral molecule and cation is calculated and is presented in **Figure 8.**

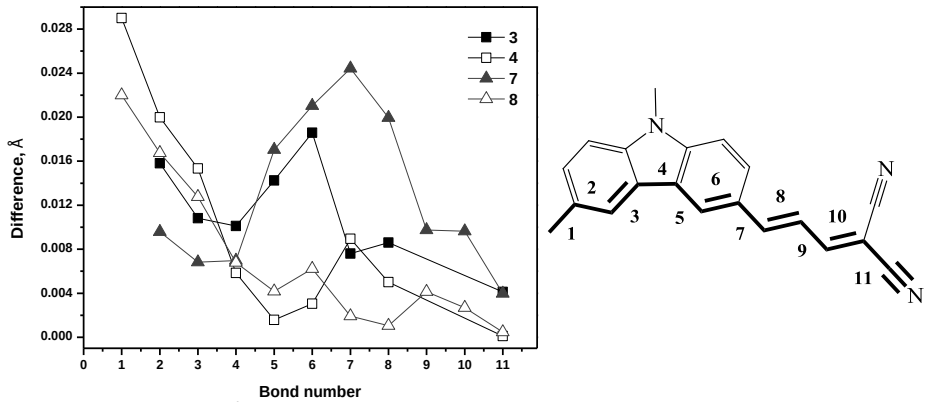

Figure 8. Differences (Å) between neutral- and cationic state bond-lengths in π-conjugated backbones of dyes **3**,**4** and **7**,**8**

In the case of compounds **4** and **8**, the larger geometrical modifications are found at the junction between the two carbazole units (bond numbers 1 and 2). This is because of the significant difference of dihedral angle and bond length in the cationic state of compounds **4** and **8** as compared to the neutral states (**Table 5**). On the contrary, in the case of compounds **3** and **7**, the larger geometrical modifications are found around the π-linker (bond numbers 5-8). In all cases, small geometrical modifications can be observed on the cyano groups.

The smallest λ_D (**Table 4**) for compound **3** stems from the global HOMO localization in the rigid carbazole moiety, exhibiting only small contributions coming from the ethenyl part. The addition of a methine moiety (compound **7**) allows for additional HOMO distribution over less rigid molecular moieties, resulting in increased λ_D. Going from **3** to **4** induces a very smooth dihedral angle in the molecular position presenting the largest contribution to HOMO. The large

variation of bond number 1 in **Figure 8** witnesses for this effect, and explains the large increase in λ_D between **3** and **4** (0.044 eV and 0.145 eV, respectively). Comparison of the geometrical parameters at neutral and cationic states shows that the additional methine unit in the π-linker has only a small effect on the structure of compound **8** as compared to **4**. However, λ_D of **8** is much smaller than λ_D of **4**, which is due to the larger HOMO distribution on the peripheral parts in **8** at the expense of the central (Cz-Cz junction) part. In view of the largest contribution of this junction on the λ_D values, this larger HOMO delocalization in **8** reduces importantly λ_D **8** as compared to **4**. Based only on λ_D values of all synthesized dyes and with the precautions mentioned on the Marcus region, it can be assumed that the compound **3** with the smallest λ_D should have the fastest dye regeneration, while dye **4** with highest λ_D value will show slowest.

Table 5. Cz-Cz junction dihedral angles and bond lengths in the neutral and cationic states of dyes **4** and **8**

Compound	Neutral		Cation	
	Dihedral angle, °	Bond length, Å	Dihedral angle, °	Bond length, Å
4	39	1.486	25	1.457
8	39	1.486	28	1.464

As an indirect indication on the charge-transport properties of these dyes, we have measured the hole mobility (μ_h) of the dyes. The dependency of μ_h on the square root of the electric field for the layers of compounds **4** and **7**,**8** is shown in **Figure 9**. The μ_h in vapor deposited layers of dyes was established using TOF method. Unfortunately, it was not possible to measure μ_h in the layer of dye **3**. Compounds show μ_h values at an electric field of $6.4 \cdot 10^5$ cm^2/Vs in the order **8** < **7** < **4**. Compounds **7** and **8** demonstrate rather close μ_h values which reach $1.72 \cdot 10^{-5}$ and $1.84 \cdot 10^{-5}$ cm^2/Vs, respectively, whereas dye **4** demonstrates the worse charge transporting properties.

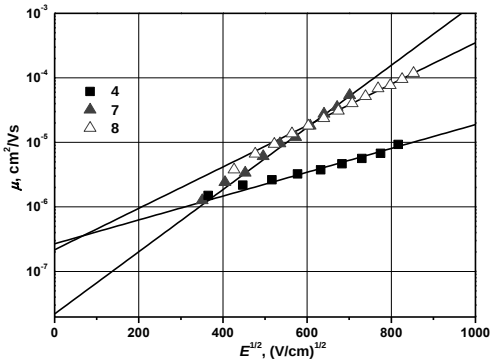

Figure 9. Electric field dependencies of hole drift mobility of the layers of **4**, **7** and **8**

The trends in hole mobilities appear to be supported by the theoretical calculations. Considering the μ_h and λ_D values of these compounds, it can be assumed that dyes **7** and **8**, having extended conjugated π-linker, will have the fastest intermolecular charge transfer rates. Both smaller λ_D and the more extended π-linker in compounds **7** and **8** are consistent with the larger hole mobility found for these compounds as compared to **4**. We conclude that, limited to these two properties and ignoring the differences in the driving force, the above trend should also hold true during the dye regeneration process in DSSCs using these compounds.

4.1.6. Photovoltaic characteristics

The power conversion efficiency (η) of DSSCs is determined from fill factor (*FF*), open-circuit photovoltage (V_{OC}), short-circuit current density (J_{SC}) and intensity of the incident light (I_S), as shown in the following equation [147]:

$$\eta = FF\frac{V_{OC}\,J_{SC}}{I_S}. \quad (3)$$

We focus here on the impact of J_{SC} on the performance of DSSCs. The J_{SC} is defined as [148]:

$$J_{SC} = e\int_{\lambda} LHE(\lambda)\phi_{inj}(\lambda)\eta_{coll}\eta_{reg}I_s(\lambda)d\lambda; \quad (4)$$

Where $LHE(\lambda)$ is the light harvesting efficiency at wavelength λ, ϕ_{inj} means electron injection efficiency from the photo-excited dye into semiconductor, η_{coll} describes the charge collection efficiency and η_{reg} is regeneration efficiency of oxidized dye. The ϕ_{inj} is in direct proportion to the injection driving force (ΔG_{inj}). The ΔG_{inj} can be described as difference between the oxidation potential of the excited dye and the conduction band edge of TiO_2 semiconductor (-4.26 eV [149]). While η_{reg} is related to the regeneration driving force (ΔG_{reg}) defined as the difference between the oxidation potential of the ground state of the dye and oxidation potential of HTM. $I_S(\lambda)$ is the incident light intensity at wavelength λ.

The values of ΔG_{inj} and ΔG_{reg} were calculated according to the experimental results:

$$\Delta G_{inj} = \mathrm{IP}^{*}_{\mathrm{PE}} - 4.26, \quad (5)$$

The ionization potentials (IP_{PE}^{*}) of excited dyes were obtained by:

$$\mathrm{IP}^{*}_{\mathrm{PE}} = \mathrm{IP}_{\mathrm{PE}} - \lambda_{\mathrm{ab}}, \quad (6)$$

For the ΔG_{reg} calculation oxidation potential of the popular spiro-OMeTAD (5.22 eV [139,150]) was used:

$$\Delta G_{reg} = 5.22 - \mathrm{IP}_{\mathrm{PE}}. \quad (7)$$

Simultaneously theoretical ΔG_{inj}^{theor} and $LHE(\lambda)$ were determined based on results of theoretical calculations:

$$\Delta G_{inj}^{theor} = \text{IP} - 4.26. \quad (8)$$

$$\Delta G_{reg}^{theor} = 5.22 - \text{IP}. \quad (9)$$

$$LHE(\lambda) = 1 - 10^{-f}. \quad (10)$$

Here f is the oscillator strength. Calculated experimental ant theoretical characteristics are given in **Table 6**.

Table 6. Experimental ant theoretical photovoltaic characteristics of dyes **3**,**4** and **7**,**8**

Compound	IP_{PE}, eV	IP_{PE}^{*}, eV	ΔG_{inj}, eV	ΔG_{inj}^{thoer}, eV	ΔG_{reg}, eV	ΔG_{reg}^{thoer}, eV	$LHE(\lambda)$
3	5.80	2.93	-1.33	-0.21	-0.58	-2.15	0.62
4	5.50	2.72	-1.54	-0.48	-0.28	-1.58	0.74
7	5.63	2.98	-1.28	-0.15	-0.41	-1.79	0.88
8	5.25	277	-1.49	-0.29	-0.03	-1.38	0.83

The calculated ΔG_{inj} have negative values ranging from -1.28 eV to -1.54 eV which means that states of excited dyes **3**,**4** and **7**,**8** lie above the conduction band of TiO_2. Compounds **3** and **7** have more positive ΔG_{inj} values compare with dyes **4** and **8**. This suggests that dyes with larger value of ΔG_{inj} will exhibit higher electron injection efficiency from excited state to semiconductor. The ΔG_{reg} values in range from -0.03 eV to -0.58 eV are below the oxidation potential of spiro-OMeTAD. However, ΔG_{reg} of compound **8** is very small and there is no driving force for dye regeneration. The ΔG_{inj}^{theor} and ΔG_{reg}^{thoer} have the same trend as ΔG_{inj} and ΔG_{reg}, respectively, only values of theoretical values are much lower than experimental. This difference can be explained by the absence of environmental effect. The theoretical calculations were performed in gas phase while experimental measurements were taken from layers of dyes. The high $LHE(\lambda)$ is important to enhance the *Jsc* and finally results in increasing η of DSSCs. Compounds **7** and **8** with additional methine unit in π-linker exhibit larger $LHE(\lambda)$ values.

Based on these results, it can be seen that the DSSC efficiency is determined by a combination of different effects. Comparing experimental photovoltaic characteristics and charge transfer rates can suggest that dye **7**, having most appropriate oxidation potential, intensive light harvesting and high charge transfer rate, is more suitable for DSSC than the other synthesized dyes.

4.2. Triphenylamine-based hydrazones

In the present chapter synthesis and characterization of triphenylamine-based hydrazones is reported. Aromatic hydrazones are among the most attractive organic HTMs due to relatively good charge transporting properties, simple synthesis and low cost. [151] In some fields of application, such as DSSCs, HTMs with low ionization potentials are required. Methoxy groups are known to be related to the mesomeric effect and the possibility to establish hydrogen bonds. These factors enhance Stokes shifts, decrease ionization potentials and establish considerable electronic coupling. [152]

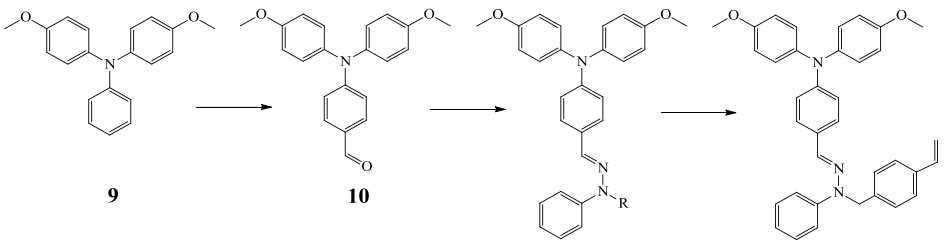

	11	12	13
R	H	CH_3	

Scheme 5. Synthesis of triphenylamine-based hydrazones

The synthetic routes to triphenylamine-based hydrazones with different substituents **12-14** are shown in **Scheme 5**. The first step was Ullmann coupling [153] reaction to get triphenylamine derivative **9** with methoxy groups at para position. The second step was formylation of compound **9** by the method of Vilsmeier-Haack [135]. The next step was the condensation of aldehyde **10** with differently substituted hydrazines. In the last step monomer **14** was obtained by interaction of compound **11** with 1-(chloromethyl)-4-vinylbenzene.

4.2.1. Thermal properties

Thermal properties of hydrazones **12-14** are given in **Table 7**, while DSC curves of compounds **12** and **14** are shown in **Figure 10a,b**.

Table 7. Thermal characteristics of compounds **12-14**

Compound	T_m, °C	T_g, °C	T_D, °C
12	134	32	293
13	179	56	259
14	65	52	307

All compounds were isolated as crystalline materials. The first DSC heating scans of these compounds revealed endothermic melting signals. No signals of

crystallization were observed in the cooling scans. The following heating scans showed only glass transition. The melting points of crystalline materials depend on the nature of hydrazine moiety. The compounds **12** and **13** showed T_m at 134 °C and 179 °C, respectively. While compound **14** having 1-methyl-4-vinylbenzene substituent revealed much lower T_m at 65 °C. Continuing heating self-polymerization of monomer **14** was recorded. Two exothermic peaks were observed with maxima at 161 °C and 209 °C (**Figure 10b**). These results are comparable with the earlier reported observation. Huang at al. [154] observed self-polymerization of aromatic amine with reactive vinyl groups in the range of 150-180 °C. The T_g of compounds depends on molecular weight. Methylphenyl-substituted hydrazone **12** demonstrate T_g at 32 °C. Compounds **13** and **14** showed T_g higher than 50 °C. While the T_g of the product of polymerization of compound **14** was found to be 97 °C which is considerably higher than that of the monomer.

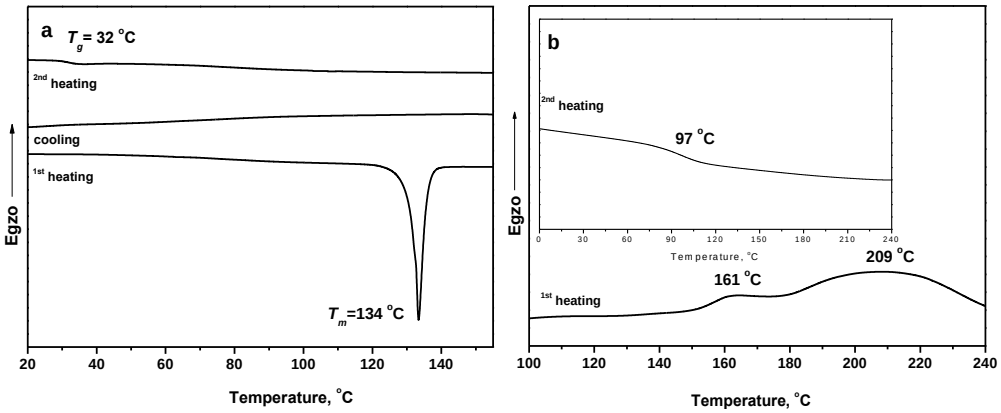

Figure 10. DSC curves of hydrazones **12** (**a**) and **14** (**b**)

The thermal stability of aromatic hydrazones is predetermined by the degradation of hydrazine moiety. Compound **12** show 5% weight loss T_D at 293 °C. Diphenyl-substituted hydrazone **13** reveal lower thermal stability temperature than methyl-phenyl-substituted compound **12**. The 5% weight loss T_D of monomer **14** at 307 °C can be attributed to thermal degradation of self-polymerization product.

4.2.2. Geometrical structure and frontier orbitals

The theoretical calculations agree with the experimental data in showing that three phenyl rings of TPA assume a propeller-like structure. The dihedral angles between phenyl ring planes and C-N-C bond are slightly more than 40°. [155, 156] The geometrical structures of compounds **12-14** are presented in **Figure 11**. Substitutions and spatial effects influence on the dihedral angles of TPA. The hydrazine moiety and methoxy groups in compounds **12-14** changed dihedral angles of TPA units in the range from 35.96° to 47.78°. The phenyl ring of hydrazine fragment of compound **12** has dihedral angle of 59.45° with respect to N-N bond. In case of compounds **13** and **14** the phenyl and the 1-methyl-4-vinylbenzene

substituents, effected by second phenyl ring, are more twisted with dihedral angles of 81.66° and 83.19°, respectively.

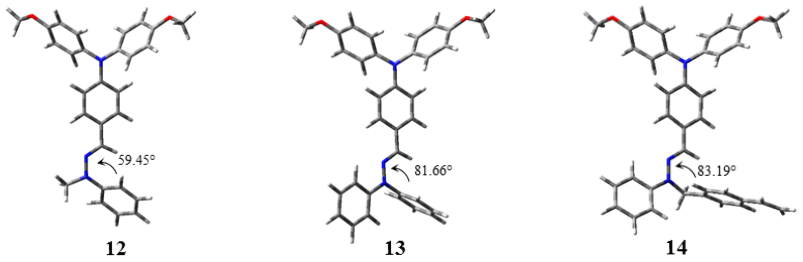

Figure 11. The theoretical geometrical structures of hydrazones **12-14** calculated at B3LYP/6-31G(d,p) level

HOMO of compounds **12-14** is distributed in whole molecule extending from oxygen atom of methoxy groups to nitrogen atoms of hydrazine fragment are related with π-donor effect. These atoms extend conjugated π-electron system of compounds. LUMO of **12** and **13** is located predominantly on the one phenyl ring of TPA and hydrazine moiety (**Figure 12**). What is interesting is that electronic cloud distribution of HOMO and LUMO of monomer **14** is almost separated, the LUMO is mainly centralized on 1-methyl-4-vinylbenzene. The broad distribution of HOMO of compounds **12-14** suggests good hole transport through the molecules when they are used as donor materials in the optoelectronic devices.

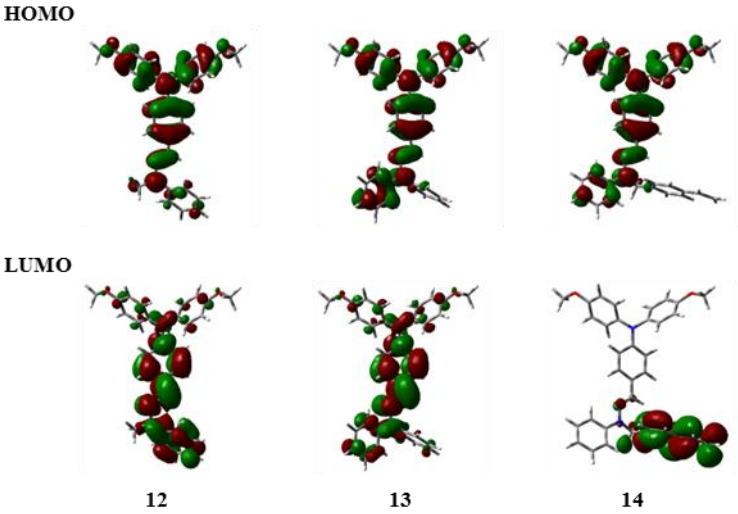

Figure 12. HOMO and LUMO distribution of hydrazones **12-14** (B3LYP/6-31G(d,p) level)

4.2.3. Optical properties

The experimental and theoretical absorption spectra of **12-14** are shown in **Figure 13a,b**, while optical characteristics are presented in **Table 8**.

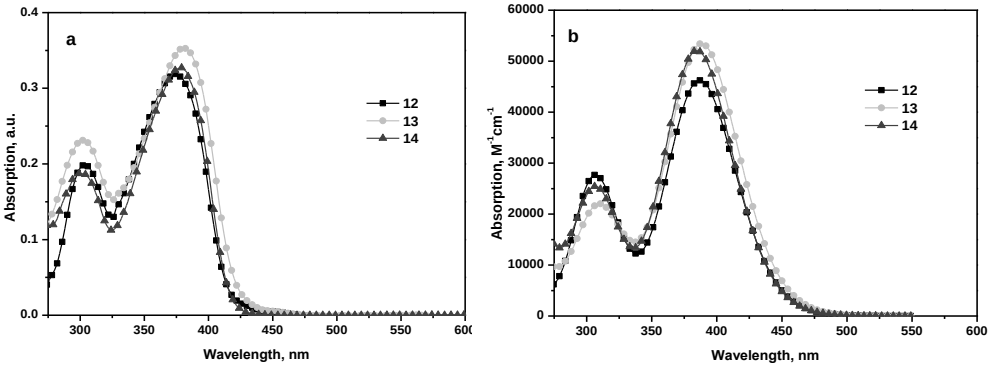

Figure 13. Experimental (**a**) and theoretical in gas phase (**b**) absorption spectra of hydrazones **12-14**

The absorption spectra of dilute tetrahydrofuran solutions of hydrazones **12-14** are characterized by two absorption bands with peaks in the range from 300 nm to 380 nm.

Table 8. Optical characteristics of compounds **12-14**

Compound	Electron transition	λ [a], nm	f [b]	Main transition configuration (%)	λ_{ab} [c], nm	λ_{fl} [d], nm
12	$S_0 \rightarrow S_1$	386	0.8470	H→L (97%)	374	434
	$S_0 \rightarrow S_5$	306	0.2369	H→L+4 (95%)	304	
13	$S_0 \rightarrow S_1$	388	0.9246	H→L (95%)	380	458
	$S_0 \rightarrow S_6$	310	0.2180	H→L+4 (95%)	302	
14	$S_0 \rightarrow S_2$	384	0.9290	H→L+1 (98%)	378	448
	$S_0 \rightarrow S_7$	308	0.2239	H→L+4 (94%)	300	

[a] theoretical lowest energy band of absorption and [b] oscillator strength (gas phase); [c] experimental bands of absorption, [d] experimental maximum band of fluorescence emission (λ_{ex} = 310 nm)

The lowest absorption bands of hydrazones correspond to the electron transition from HOMO to LUMO for **12** and **13**, while for compound **14** from HOMO to LUMO+1 (**Table 8**). The replacement of the methyl group in compound **12** by phenyl and 1-methyl-4-vinylbenzene fragments in **12** and **13**, respectively, leads to a slightly bathochromic shift of 6 nm and 4 nm. The addition of phenyl and 1-methyl-4-vinylbenzene units in hydrazones makes the second phenyl ring planar with N=N, hence determines the slightly larger conjugated π-electron system. The theoretical results revealed that peaks at 300-304 nm are caused by absorption localized in the TPA moiety, which are attributed to the electron transitions from HOMO to LUMO+4. The LUMO+4 is localized on diphenylamine unit of TPA

fragment for all analyzed hydrazones (as an example the molecular orbitals of compound **14** are shown in **Figure 14**). Synthesized hydrazones **12-14** might be good HTM candidates for DSSCs, because they absorb light only in UV part, and all visible light falls to dye.

Electron transition $S_0 \rightarrow S_2$

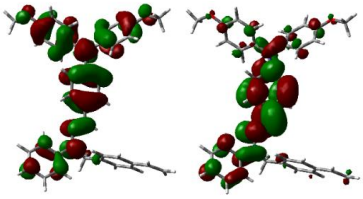

Electron transition $S_0 \rightarrow S_7$

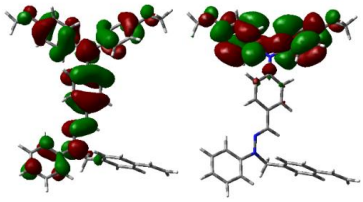

Figure 14. Molecular orbitals of electron transitions of hydrazone **14** (B3LYP/6-31G(d,p) level)

The compounds **12-14** exhibit blue fluorescence when excited with UV irradiation. Their fluorescence maxima appear in the range from 434 nm to 458 nm.

4.2.4. Electrochemical and photoelectrical properties

The electrochemical properties of the solutions of hydrazones in dichloromethane were studied by CV. The cyclic voltammograms of compound **13** are shown in **Figure 15**.

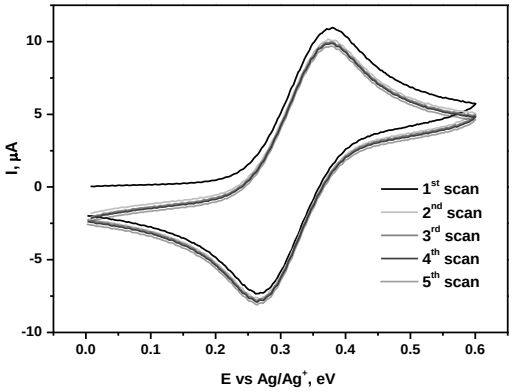

Figure 15. Cyclic voltammograms of compound **13**

The electrogenerated cation radical of triphenylamine is not electrochemically stable and form *tetra*-phenylbenzidine. However, when three phenyl rings of

triphenylamine are substituted at the *para* position the coupling reactions can be avoid. [157,158] The synthesized hydrazones **12-14** form stable cations and their oxidation is reversible. The same values of anodic and cathodic peaks were observed for each compound for five times repeated cycles (**Figure 15**).

The electrochemical data and calculated HOMO, LUMO and IP values are presented in **Table 9**.

Table 9. Values of electron affinity, ionization potentials, optical band gap and HOMO/LUMO energies of compounds **12-14**

Compound	IP_{CV} [a], eV	E_g^{opt} [b], V	EA_{CV} [a], eV	HOMO [c], eV	LUMO [c], eV	IP [c], eV
12	4.88	2.97	1.91	-4.40	-0.80	5.40
13	4.90	2.94	1.96	-4.42	-0.85	5.42
14	4.93	2.97	1.97	-4.45	-0.94	5.45

[a] determined by cyclic voltamperometry; [b] calculated from absorption spectra; [c] calculated theoretical at B3LYP/6-31G(d,p) level

The oxidation potentials of hydrazones were calculated as the average of the anodic and cathodic peak potentials. The IP_{CV} values determined from the oxidation potential values of compounds with respect to ferrocene are considerably close and range from 4.88 eV to 4.93 eV. The IP_{CV}, IP and HOMO values of compounds **12-14** have the same trend and increase in the order **12** < **13** < **14**. The EA_{CV} values calculated from IP_{CV} and optical band gap (E_g^{opt}) values are in the range 1.91-1.97 eV.

The hole drift mobilities of hydrazones **12-14** were measured by TOF technique. It is worth mentioning, that compounds **12** and **13** formed amorphous layers but they were uneven. Therefore, layers of bisphenol Z polycarbonate (PC-Z) containing 50 wt. % of hydrazone **12** or **13** were made for experiment. Hole drift mobility versus the square root of applied electric field curves are shown in **Figure 16**.

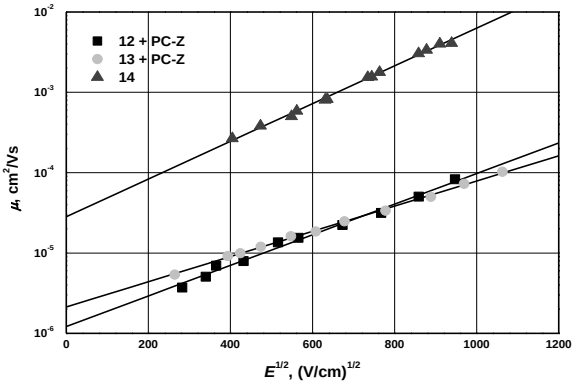

Figure 16. Electric field dependencies of hole-drift mobilities in the films of the 50% solid solutions of compounds **12**,**13** in PC-Z and in the pure layer of compound **14**

Molecularly doped PC-Z containing **12** or **13** show hole drift mobilities approaching 10^{-4} cm^2/Vs at high electric fields. These values are high keeping in mind that charge mobilities larger by at least one order of magnitude can be predicted for the amorphous layers of pure materials. Hole drift mobility in the pure layer of **14** reached $2.2 \cdot 10^{-3}$ cm^2/Vs at an electric field of $6.4 \cdot 10^5$ cm^2/Vs.

4.2.5. Solid state dye sensitized solar cells

In DSSCs, HTM can be deposited by various methods, including thermal evaporation and from solution. Studies have indicated that for solution deposited spiro-OMeTAD the pore filling fraction is never more than 70%. [52] This poor pore filling limits the photocurrent available from these cells. An alternative approach that could circumvent the pore filling problem would be the use of a solvent free, melt processable hole conductors to infiltrate the mesoporous TiO_2. [159] The hydrazone **12** was used as HTM for preparation of DSSC devices by melt process. The structure of prepared DSSCs is shown in **Figure 17**.

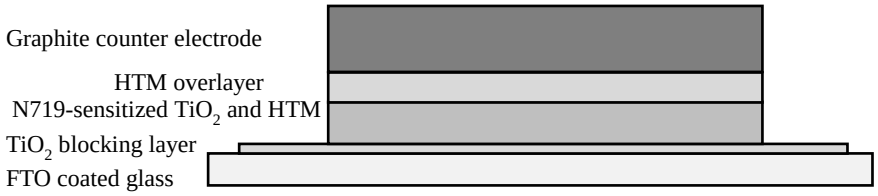

Figure 17. The DSSC structure (compound **12** was used as hole transporting material)

The hydrazone **12** powder was added into the space between glass plate and N719-sensitized TiO_2 film and heated at a temperature slightly higher than T_m of **12** in the nitrogen atmosphere. In several minutes the whole TiO_2 active area was covered. Then, the substrate was compressed, to minimize the overlayer of hydrazone **12**, and was cooled down. In order to *p*-dope compound **12**, the glass plate was removed and the substrate was transferred into a vial containing iodine crystals. After doping a graphite electrode was applied to the hydrazone **12** overlayer to complete the DSSC. In some cases LiTFSI in acetonitrile was drop-cast on top of dye-sensitized TiO_2 prior the melting process.

An energy level diagram of the DSSC components and the fundamental charge transfer processes are presented in **Scheme 6**. Upon light absorption, an electron is excited from HOMO to LUMO of the dye molecule. The electron is then injected (1) from excited state of dye into the conduction band of TiO_2. The resulting photo-oxidized dye can be regenerated (2) by HTM or it can recombine with the injected electron (3). After dye regeneration, charge transport is competing against electron recombination (4) with a hole in the HTM layer. [160] The energy values of TiO_2 conduction band edge and dye HOMO/LUMO levels were recently summarized by Zhang et al. [161]. Meanwhile, ionization potential of hydrazone **12** was measured from compound film by electron photoemission in air method (5.26 eV).

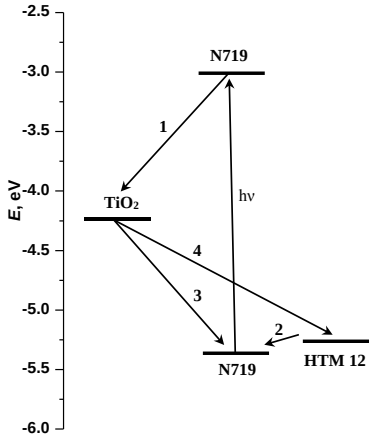

Scheme 6. Energy levels of the DSSC components and charge transfer processes

The photovoltaic characteristics of DSSCs are summarized in **Table 10** and current–voltage curves of the corresponding cells at approximately 1 sun illumination are given in **Figure 18a**.

Table 10. The parameters of solar cells **A**-**D**

Device	J_{SC}, mA/cm^2	V_{OC}, V	FF	η, %	LiTFSI	Iodine vapour exposure time, min
A	0.02	0.35	0.26	0.002	No	2
B	0.13	0.56	0.34	0.025	Yes	5
C	0.33	0.52	0.43	0.075	Yes	15
D	0.47	0.27	0.33	0.042	No	80

DSSC **A** showed very low J_{SC} and small η. After iodine vapour exposure for 80 minute, current increased to 0.47 mA/cm^2 and efficiency to 0.042 %. Supposedly, the effect of iodine doping is due to increasing conductivity of the compound **12** overlayer. Device **C** doped with iodine for 15 min and having LiTFSI had the best photovoltaic parameters with η of 0.075 %.

TAS was employed to study photoinduced charge transfer kinetics in DSSCs (**Figure 18b**). In the FTO/TiO_2/N719/CM (coumarin (CM) was used as inert meltable material that would not generate dye) spectrum the strong absorption at 700-900 nm, centered at 810 nm, is attributed to the oxidized dye [162,163] and absorption at 700-990 nm contribute to electrons in the TiO_2 [164]. The presence of oxidized dye and TiO_2 electrons, and the magnitudes of the signals, indicate that excited state electron injection from the dye into TiO_2 is not strongly reduced by the melt infiltration procedure. Replacing the inert coumarin with hydrazone **12** strongly reduce the absorption centered at 810 nm compared to N719/CM case. In addition, strong absorption at 460-590 nm appears which is assigned to the compound **12** cation. It was determined that the regeneration of oxidized N719 by hydrazone **12** is complete by 3 μs. Results show good TiO_2 pores filling or at least good surface

coverage of the pores but this does not ensure good DSSCs performance. Fast recombination and slow charge transfer may be the main performance limiting factors. However, melt processing HTMs is an alternative option to infiltrate mesoporous nanocrystalline electrodes with compounds which otherwise might not be available for deposition from solution or thermal evaporation.

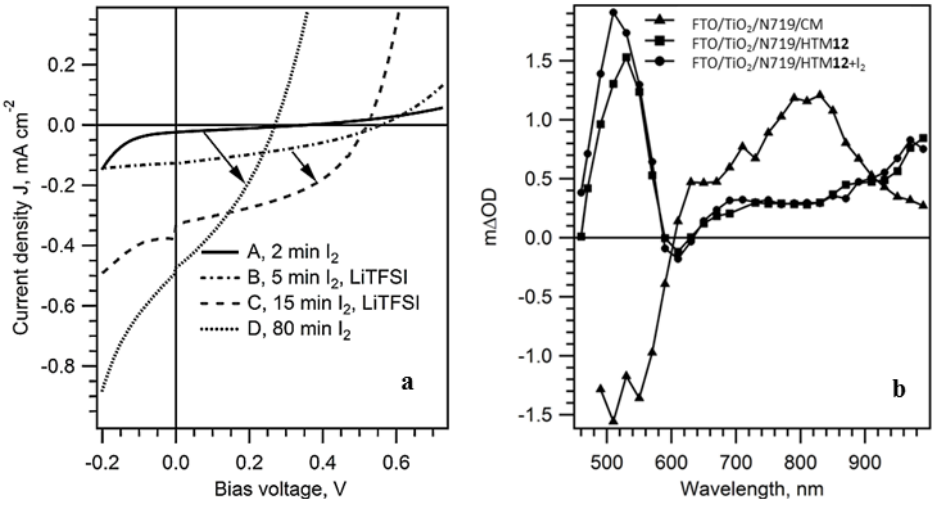

Figure 18. Current-voltage characteristics of the DSSCs (**a**) and transient absorption spectra recorded 3μs after laser pulse of 460 nm of devices (**b**)

4.3. Carbazole-imidazole compounds

PHOLEDs having carbazole-imidazole based materials as hosts showed high quantum efficiency. [84,85] Among the large bandgap materials carbazole is the most widely used hole transport moiety because of a high triplet energy and rigid molecular framework, and can be easily substituted with various electron transport units such imidazole. [165,166]

Based on previous arguments compounds **15**,**16** and **19**,**20** were designed and reported in this chapter. The target compound **15** was synthesized from commercial 9-ethyl-9*H*-carbazole-3-carbaldehyde (**CrC**), 9-ethyl-9*H*-carbazol-3-amine (**CrA**) and benzil. During the condensation reaction *tetra*-substituted imidazole ring was obtained. At next step, *tetra*-butyl groups were attached to carbazole units getting **16**. Compound **17** was prepared from carbazole and 2-ethylhexyl bromide and used for synthesis of di-aminocarbazole **18**. At the last steps compounds **19** and **20** were obtained according the procedures as **15** and **16**, respectively. The synthetic routes for preparation of carbazole-imidazole compounds is presented in **Scheme 7**.

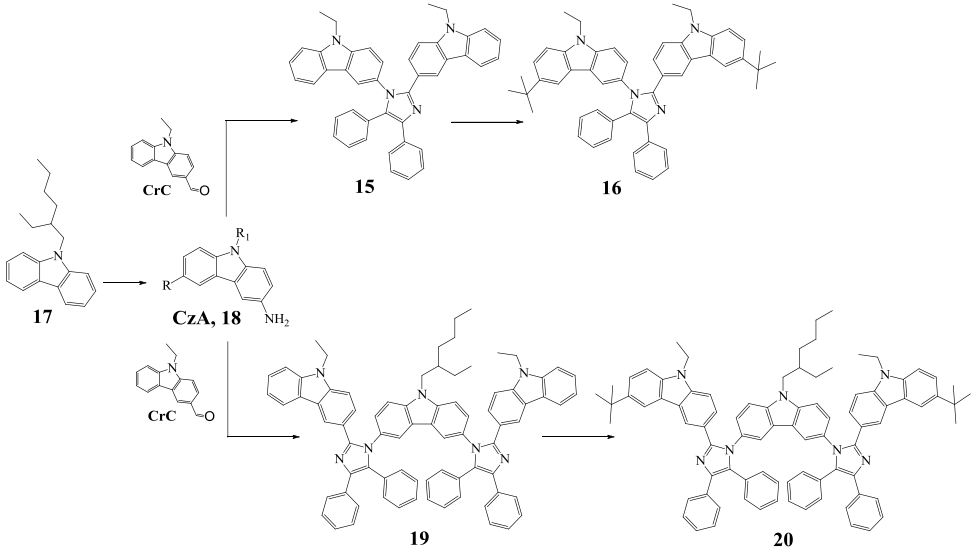

	CzA	18
R	H	NH_2
R_1	ethyl	ethylhexyl

Scheme 7. Synthesis of carbazole-imidazole compounds

4.3.1. Thermal properties

The behavior of synthesized compounds **15**,**16** and **19**,**20** under heating was studied. The results obtained by TGA and DSC are summarized in **Table 11**.

Table 11. Thermal characteristics of compounds **15**,**16** and **19**,**20**

Compound	T_D, °C	T_m, °C	T_g, °C	T_{cr}, °C
15	399	270	134	236
16	400	-	147	-
19	477	-	151	-
20	487	-	172	-

The high thermal stability and formation an amorphous layers are required for host materials to improve characteristics of device. [167] The synthesized compounds **15**,**16** and **19**,**20** show high thermal stability as confirmed by TGA. The T_D of compounds with one imidazole ring is about 400 °C while compounds with two imidazole units show T_D higher than 477 °C. Furthermore, compounds **19** and **20** demonstrate larger residue at the end of experiment comparing that with **15** and **16** (**Figure 19a**).

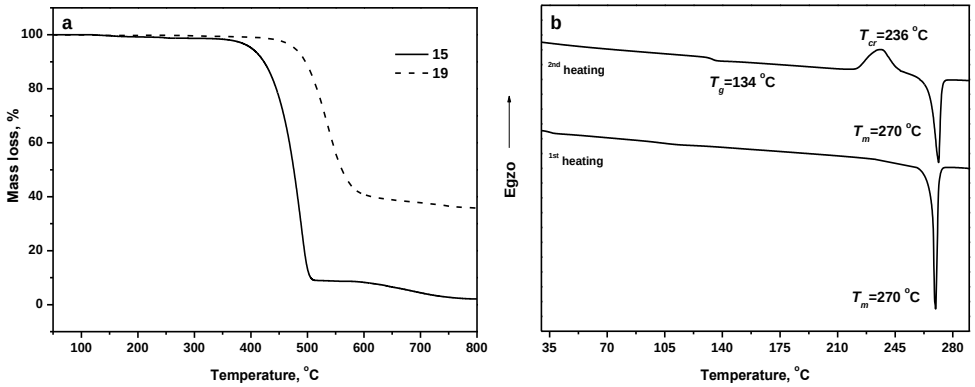

Figure 19. TGA curves of compounds **15** and **19** (**a**), DSC curves of compound **15** (**b**)

Compound **15** was isolated as crystalline material. In the first heating scan of **15** endothermic melting signal was observed at 270 °C. The second heating scan revealed T_g at 134 °C and the further heating showed crystallization and melting signals. The DSC curves of compound **15** are presented in **Figure 19b**. The compounds **16**, **19** and **20** were isolated as amorphous materials with T_g at 146 °C, 151 °C and 172 °C, respectively, in the heating and cooling scans. Therefore DSC results demonstrate that the additional carbazole-imidazole moiety or *tert*-butyl groups increase temperature of glass transition.

4.3.2. Geometrical structure and molecular orbitals

Analysis of the geometrical structure of compounds **15**,**16** and **19**,**20** suggest that the lone pair electrons of nitrogen atom will extend π-conjugation through carbazole and imidazole moieties. However, large dihedral angles **b** from 61.68° to 64.81° between these fragments were found. Otherwise twice lower dihedral angles **a** (33.08-34.49°) compared with dihedral angles **b** causes strengthened conjugated interaction and more planar structure between moieties connected through a carbon atom. Geometrical structures of compounds **15** and **16** are presented in **Figure 20**.

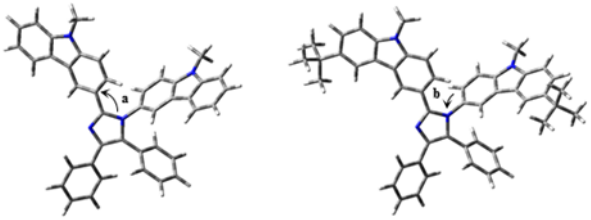

Figure 20. The theoretical geometrical structures of compounds **15** and **16** calculated at B3LYP/6-31G(d,p) level

Because of this molecule structure the compounds **15**,**16** and **19**,**20** have clearly localized frontier orbitals (**Figure 21**).

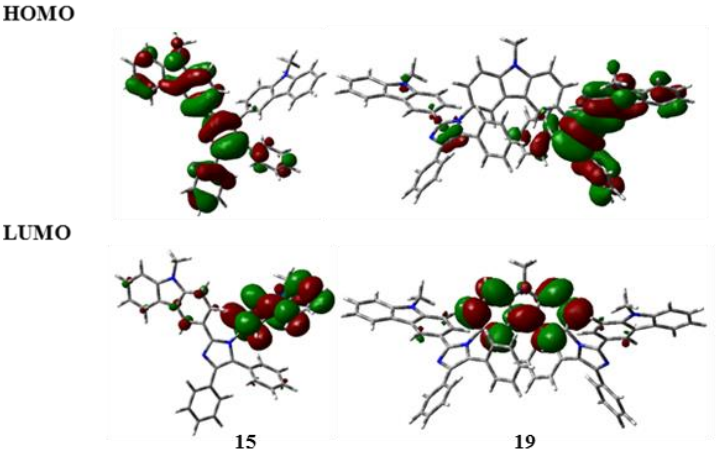

Figure 21. Frontier orbitals of compounds **15** and **19** (B3LYP/6-31G(d,p) level)

The electronic cloud distribution is localized on the conjugated carbazole-imidazole fragment in the HOMO. While for the LUMO, electronic cloud is localized on the carbazole unit. The separation in the spatial distributions between HOMO and LUMO at compounds different moieties is preferable for efficient hole and electron transport. [168]

4.3.3. Mixed valence character of compounds

Mixed valence systems usually consist of two or more redox centres with different oxidation states that are connected by bridge. [169] The cations of compounds **19** and **20**, containing two identical carbazole-imidazole substituents connected by carbazole, have electronic cloud distribution passing from one fragment to the other. **Figure 22** present SOMO-1 and SOMO orbitals of compound **19** cation.

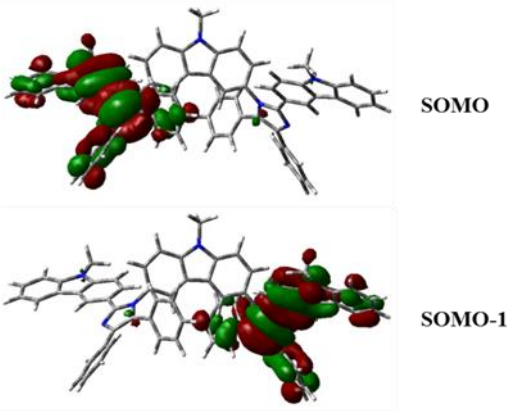

Figure 22. SOMO and SOMO-1 orbitals of compound **19** calculated by B3LYP

Additional calculations of the cations of compounds **19** and **20** were made by restricted open-shell Hartree-Fock (ROHF) functional with the 6-31G* basis set.

Natural population analysis (NPA) and Mulliken population analysis (MPA) were used to obtain the charges for each of the fragments.

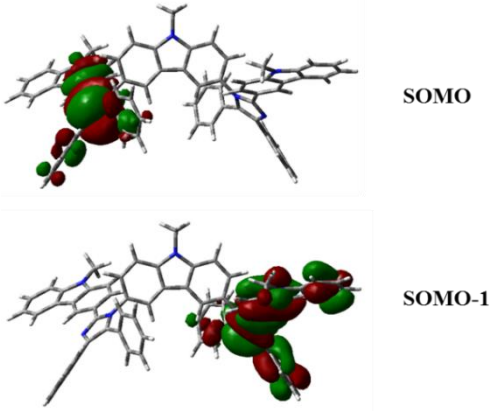

Figure 23. SOMO and SOMO-1 orbitals of compound **19** calculated by ROHF

ROHF calculations revealed that cations of compounds **19** and **20** have two redox centres at first oxidation state. The electron density of SOMO of cation **19** and **20** is predominantly localized on the imidazole part extending to the carbazole and phenyl moieties with a small portion. The SOMO-1, located on the another identical moiety, is densely distributed on whole fragment. SOMO and SOMO-1 orbitals of compound **19** cation is shown in **Figure 23**. NPA and MPA calculations proved that charge excess (+0.7 and +0.6, respectively) is localized only on one carbazole-imidazole fragment. The mixed valance character of these compounds will be shown in the following to impact on their optical and electrochemical properties.

4.3.4. Optical properties

The theoretical and experimental absorption spectra and optical properties of compounds **15**,**16** and **19**,**20** are presented in **Figure 24a,b** and **Table 12**.

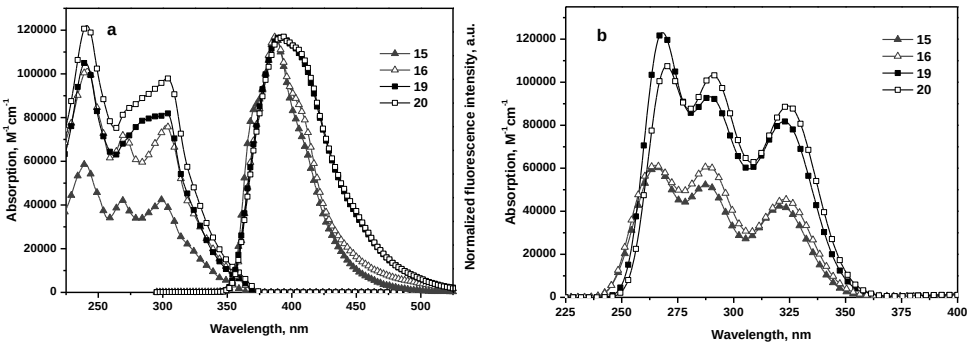

Figure 24. Experimental absorption and steady-state fluorescence emission (λ_{ex}=310 nm) spectra of dilute solutions (**a**) and theoretical absorption spectra in gas phase (**b**)

The absorption spectra of compounds **15** and **19** show three absorption signals in the range from 225 nm to 375 nm. In the case of derivatives **16** and **20**, the lowest

energy two absorption bands are overlapped. The additional carbazole-imidazole fragment connected to carbazole bridge does not contribute to the extension of the conjugated π-electrons system, because the shifts of maxima of compounds are almost identical. The experimental spectra of compounds **15**,**16** and **19**,**20** are therefore in agreement with the calculated theoretical spectra (**Figure 24a,b**), both being consistent with HOMO and LUMO localizations and the mixed valence character discussed in the previous section.

Table 12. Optical properties of compounds **15**,**16** and **19**,**20**

Compound	Electron transition	λ [a], nm	f [b]	Main transition configuration (%)	λ_{ab} [c], nm	λ_{fl} [d], nm	E_T [e], eV
15	$S_0 \rightarrow S_3$	322	0.4126	H→L+2 (96%)	299	398	3.18
16	$S_0 \rightarrow S_3$	324	0.4314	H→L+2 (94%)	303	398	3.16
19	$S_0 \rightarrow S_6$	324	0.6501	H→L+3 (51%)	303	402	3.08
20	$S_0 \rightarrow S_7$	326	0.5950	H-1→L+2 (41%)	304	403	3.05

[a] theoretical lowest energy band of absorption and [b] oscillator strength (gas phase); [c] experimental lowest energy band of absorption; [d] experimental maximum band of fluorescence emission; [e] triplet energy determined from experimental phosphorescence spectrum.

The lowest energy absorption peaks of derivatives **15** and **16** assigned to $S_0 \rightarrow S_3$ are mainly ascribed electron transfer from HOMO to LUMO+2 (**Figure 25**).

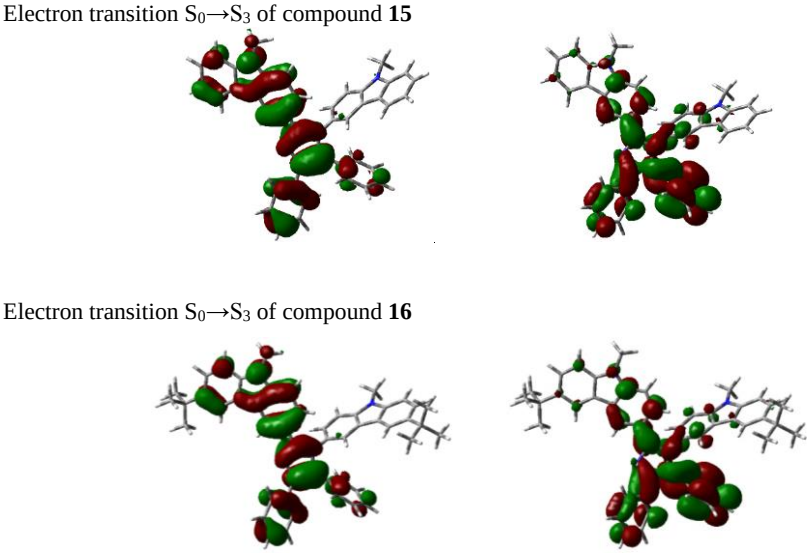

Figure 25. HOMO (left) and LUMO+2 (right) of compounds **15** and **16** (B3LYP/6-31G(d,p) level)

The transitions $S_0 \rightarrow S_6$ and $S_0 \rightarrow S_7$ of compounds **19** and **20**, respectively, were mixture of different electron transitions. In order to analyse the nature of transitions, the corresponding natural transition orbitals (NTO) [170] were calculated. The hole and electron localizations corresponding to $S_0 \rightarrow S_6$ and $S_0 \rightarrow S_7$ transitions as deduced

from NTOs are shown in **Figure 26**. According to these results, the lowest energy absorption peaks of derivatives **19** and **20** are characterized as electron transfer from carbazole-imidazole fragment to carbazole bridge.

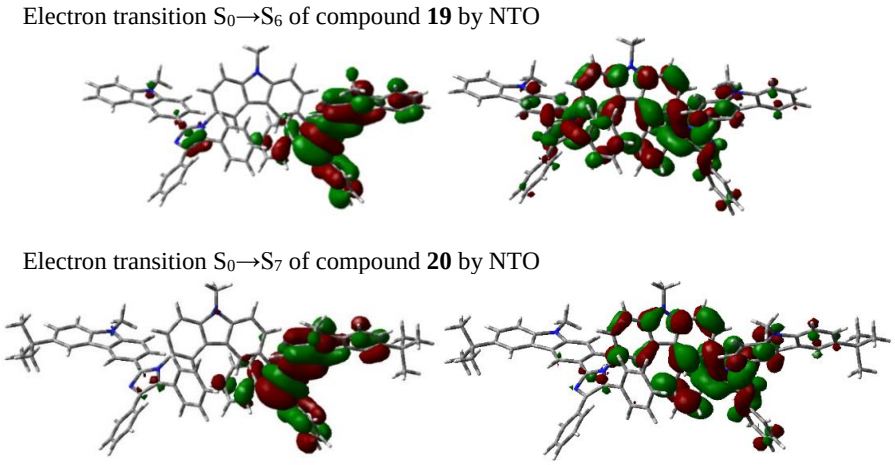

Figure 26. Natural transition orbitals corresponding to hole (left) and electron (right) distributions of transitions $S_0 \rightarrow S_6$ and $S_0 \rightarrow S_7$ of compounds **19** and **20**, respectively (B3LYP/6-31G(d,p) level)

Synthesized materials **15**,**16** and **19**,**20** emit violet light with the fluorescence emission bands in the range 398-403 nm (**Figure 24a**). The maxima bands of phosphorescence emission of these compounds in tetrahydrofuran at 77 K range from 533 nm to 537 nm. However, the phosphorescence spectra have broad peak in the higher energy region, therefore, the triplet energies (E_T) of materials were determined from the onset of the phosphorescence spectra (**Figure 27**). Material **20** presents the highest E_T of 3.18 eV, while compounds **15**, **16** and **19** exhibit slightly smaller energy levels 3.16 eV, 3.08 eV and 3.05 eV, respectively.

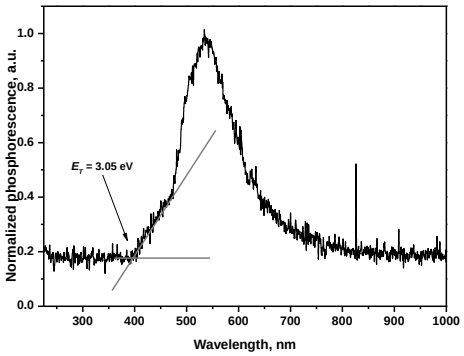

Figure 27. Phosphorescence emission spectrum of dilute solution of compound **19** (λ_{ex}=310 nm)

4.3.5. Electrochemical and photoelectrical properties

The values estimated by cyclic voltamperometry, photoemission in air method and calculated theoretical are presented in **Table 13.** The IP_{CV} of the compounds were estimated from the half wave potential of the first oxidation relative to ferrocene. The IP_{CV} values of **15**, **16**, **19** and **20** are 5.25, 5.21, 5.26 and 5.25 eV, respectively. The almost constant values of the IP_{CV} are due to their almost similar shape of electron localization of HOMO orbital on the carbazole-imidazole fragment for all compounds. This is consistent with the mixed valence character of compounds **19** and **20** discussed previously, in turn being due to the weakly efficient bridging between the two carbazole-imidazole moieties. The small range (1.81-1.94 eV) of the EA_{CV} values can be explained by the same argument, the electronic cloud of the LUMO is localized on the carbazole unit for **15**, **16**, **19** and **20**.

Table 13. Values of electron affinity, HOMO/LUMO energies and ionization potentials of compounds **15**,**16** and **19**,**20**

Compound	IP_{CV} [a], eV	EA_{CV} [a], eV	HOMO [c], eV	LUMO [c], eV	IP_{PE} [b], eV	IP [c], eV
15	5.25	1.81	-4.83	-1.02	5.35	5.77
16	5.21	1.87	-4.79	-0.97	5.18	5.71
19	5.26	1.92	-4.93	-1.31	5.29	5.65
20	5.25	1.94	-4.89	-1.29	5.22	5.60

[a] determined by cyclic voltamperometry; [b] measured by photoemission in air method; [c] calculated theoretical at B3LYP/6-31G(d,p) level

The IP_{PE} spectra of the solid amorphous samples of the materials are presented in **Figure 28**.

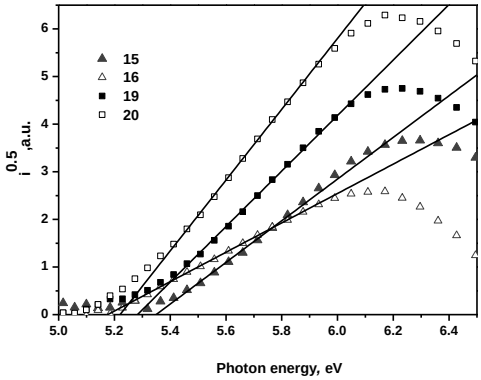

Figure 28. Photoemission in air spectra of the layers of compounds **15**,**16** and **19**,**20**

The IP_{PE} values of compounds are in the larger range from 5.18 eV to 5.35 eV comparing with IP_{CV}. This can be explained due to different environments in solution and solid layers of compounds. However, IP_{CV}, IP_{PE} and calculated IP values of compounds **16** and **20**, bearing *tret*-butyl groups, are slightly lower than

their counterparts **15** and **19**, respectively. This trend coincide with the trend of HOMO energies of compounds.

The TOF technique was used to study charge transport properties of synthesized compounds. The electric field dependencies of hole and electron mobilities of the layers of compounds **15**,**16** and **19**,**20** is shown in **Figure 29**.

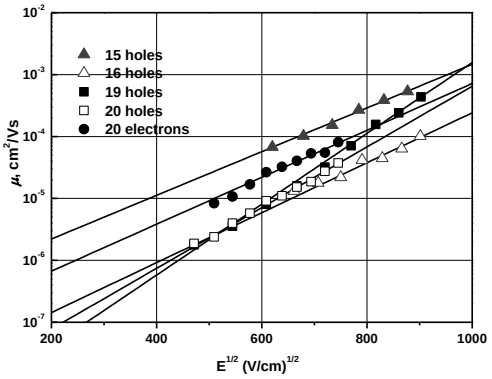

Figure 29. Electric field dependencies of hole and electron mobilities in the layers of compounds **15**,**16** and **19**,**20**

The layers of compounds demonstrate hole drift mobilities ranging from 10^{-6} cm^2/Vs to 10^{-3} cm^2/Vs at moderate electric fields. Unfortunately, electron mobility was detected only in the layer of compound **20** which reaches 10^{-4} cm^2/Vs. Therefore, there is only one order of magnitude between hole and electron mobility in the layer of compound **20**. To achieve high efficiency PHOLED, host materials with a balanced charge transport feature to generate broad charge recombination zones in the emissive layer are desirable. [62,64]

4.3.6. Performance in phosphorescent light emitting diodes

To study the performance of compounds **15**,**16** and **19**,**20** as hosts, the simple PHOLEDs **E-H** were fabricated. The energy levels of the materials used in the devices are shown in **Figure 30**.

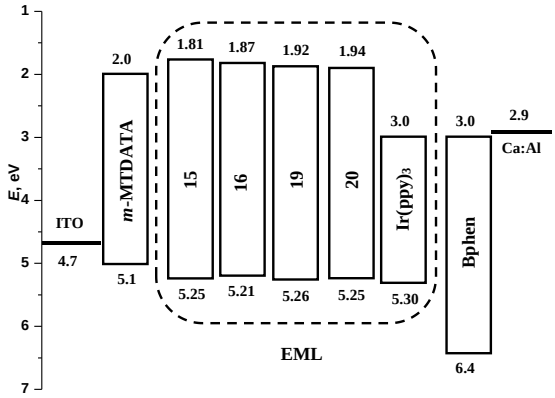

Figure 30. Energy level diagram of used materials in the PHOLEDs

To prepare the emitting layers for the devices **E**-**H** the hosts were doped with $Ir(ppy)_3$ which was used as green phosphorescent emitter. Efficient exciton confinement on the dopant $Ir(ppy)_3$ was expected due to relatively high triplet levels of **15**,**16** and **19**,**20** compounds. While *m*-MTDATA and Bphen were used for the preparation of hole- and electron-transporting layers, respectively. The molecular structures of the materials used in the PHOLEDs are shown in **Figure 31**.

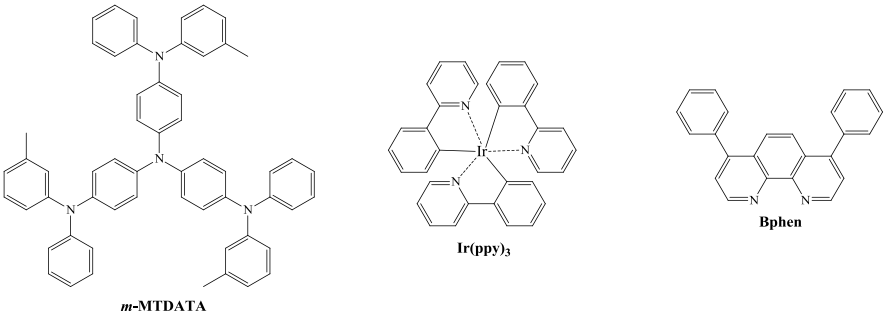

Figure 31. The molecular structures of m-MTDATA, $Ir(ppy)_3$ and Bphen

The electroluminescence (EL) spectra of the devices are shown in **Figure 32**. Despite application of the green phosphorescent emitter $Ir(ppy)_3$, most of the fabricated PHOLEDs were not characterized by green emissions. Only Devices **F** and **G** were characterized by green emissions with the intensity maxima at ca. 510 nm, confirming the radiative recombination of excitons on $Ir(ppy)_3$. Low intensity violet emissions were observed in EL spectra of all PHOLEDs. The wavelengths of these emissions were close to that of fluorescence of pure **15**,**16** and **19**,**20** showing that the recombination of excitons occurred not only on the emitter but also on hosts. According to this observation, it can be concluded that compounds **15** and **20** could be used as emitters themselves.

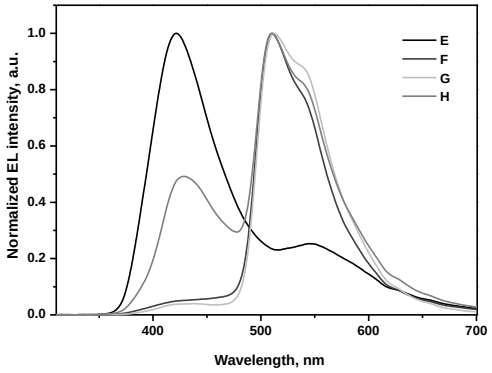

Figure 32. Electroluminescence spectra of PHOLEDs **E**-**H** recorded at applied voltage of 10 V

The luminance and efficiency characteristics of the devices **E-H** are given in **Table 14** and **Figure 33**.

Table 14. Electroluminescence characteristics of the devices **E-H**

Device	Emitting layer	V_{on}, V	Max. brightness, cd/m^2	Max. current efficiency, cd/A	Max. power efficiency, lm/W	Max. external quantum efficiency, %
E	**15**:Ir(ppy)$_3$	5.2	5580	2.7	1.1	2.5
F	**16**:Ir(ppy)$_3$	3.7	4630	3.5	1.6	0.97
G	**19**:Ir(ppy)$_3$	3.1	24600	31	13.7	8.3
H	**20**:Ir(ppy)$_3$	3.9	5800	1.9	1.1	0.74

PHOLEDs were characterized by the relatively low values (3.1-5.2 V) of the turn-on voltage (V_{on}), confirming the very efficient injection from the electrodes and transport of holes and electrons to the emission layer. The highest brightness of 24600 cd/m^2 and lowest turn-on voltage of 3.1 V observed for the device **G** compared to those recorded for the other devices shows more effective exciton recombination and radiative transition in the emitting layer with the host **19**.

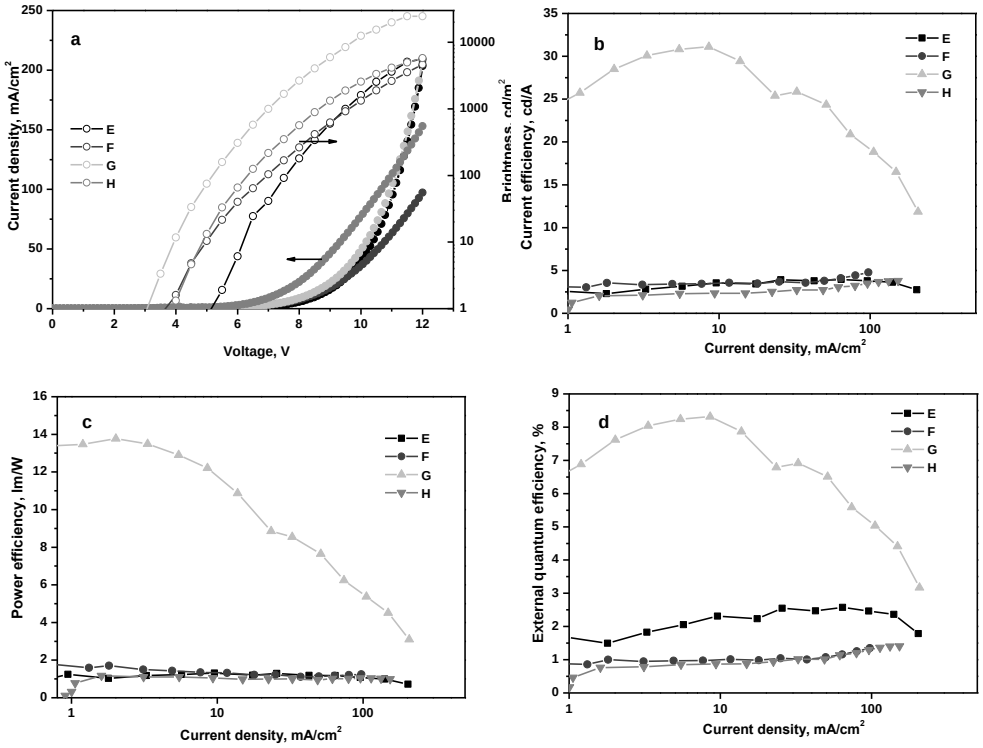

Figure 33. Electroluminescence characteristics of PHOLEDs **E-H**: current density and luminance versus voltage (**a**), current efficiency versus current density (**b**), power efficiency versus current density (**c**), external quantum efficiency versus current density (**d**)

Compound **19** can be recognized as effective host for PHOLED. The best device **G** with **19** exhibited the maximum current, power, and external quantum efficiencies of 31 cd/A, 13.7 lm/W, 8.3 %, respectively, in the absence of light outcoupling enhancement. It has to be noted, that the simple and unoptimized PHOLED based on host **19** was fabricated, therefore, the maximum efficiency of device was lower compared to those reported for PHOLEDs containing $Ir(ppy)_3$. The better performance of the device based on the host **19** can apparently be reached either after introduction of the additional layers, after the additional optimization of the concentration of dopant $Ir(ppy)_3$ in the host, or after the additional optimization of the thicknesses of the layers of the device.

4.4. Triphenylamine-twin compounds*

Photoelectrical and other properties of the compounds are considerably influenced by the nature and the number of the substituents. Recent studies [152,171,172] have reported on methoxy or methyl substituted compounds exhibiting larger hole mobilities as compared to the non-substituted ones. The improvement of hole transporting properties upon methoxy or methyl substitutions has been suggested to partly stem from the additional hydrogen bond induced by methoxy or methyl. [152,173] In this chapter the influence of methoxy and methyl substituents on triphenylamine-twin compounds is discussed.

The synthetic routes to the compounds are illustrated in **Scheme 8.** The intermediates **21-23** were prepared by the modified Ullmann reaction [153] between 4 4'-diaminobenzophenone and the corresponding aryl iodide. The target compounds **24-28** were obtained by Wittig-Horner method using the synthesized triphenylamine-based ketones and different benzylphosphonates.

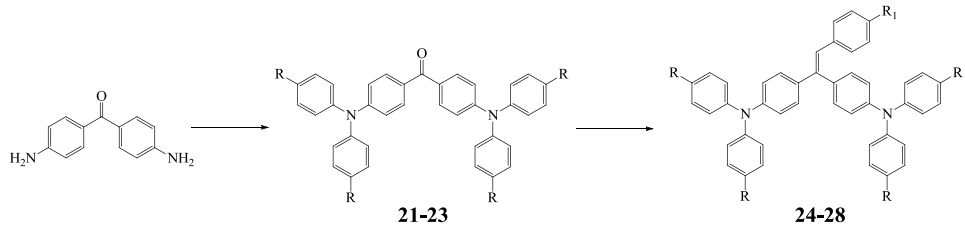

	21	22	23	24	25	26	27	28
R	H	OCH_3	CH_3	H	OCH_3	OCH_3	CH_3	CH_3
R_1	-	-	-	H	H	OCH_3	H	CH_3

Scheme 8. Synthesis of triphenylamine-twin compounds

* Dr G. Sini from Cergy-Pontoise University is thanked for the support of this work with the valuable ideas and the help in the interpretation of the results of the theoretical investigations.

4.4.1. Thermal properties

The thermal characteristics of triphenylamine-twin compounds are summarized in **Table 15**. Compounds **24**-**28** demonstrate high thermal stability. The T_D values of compounds are comparable and range from 426 °C to 436 °C.

Table 15. Thermal characteristics of compounds **24**-**28**

Compound	T_D, °C	T_m, °C	T_g, °C
24	426	160	77
25	434	181	76.5
26	436	-	74
27	429	-	71
28	430	-	73

The DSC investigations revealed that compounds **24** and **25** can exist both in crystalline and amorphous state. Derivatives **24** and **25** were obtained as crystalline materials. In the first DSC heating scan they showed endothermic melting signals at 160 °C and 181 °C, respectively. The cooling and second heating scans revealed only a glass transition of 77 °C for both the compounds. **Figure 34a** shows DSC heating and cooling curves for compound **24**.

Compounds **26**, **27** and **28** were isolated as amorphous materials and exhibited only glass transitions at 74 °C, 71 °C and 73 °C, respectively, in the first and the following DSC scans. Neither melting nor crystallization signals were observed in the DSC curves. As an example the DSC curves of compound **26** are shown in **Figure 34b**.

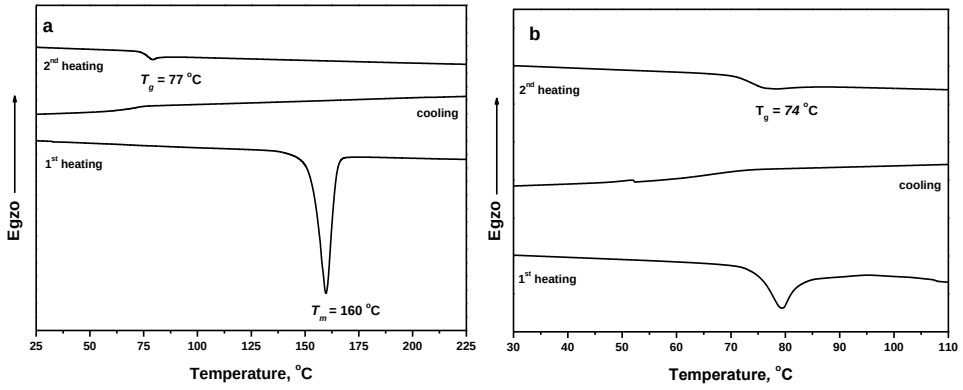

Figure 34. DSC curves of compounds **24** (**a**) and **26** (**b**)

4.4.2. Optical properties

The experimental and theoretical absorption spectra of compounds **24**-**28** are shown in **Figure 35a,b**, respectively.

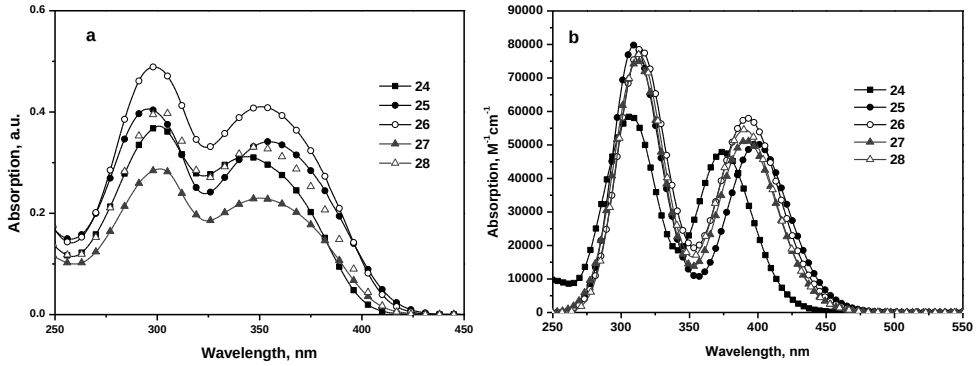

Figure 35. Experimental absorption spectra of dilute solutions of compounds (**a**) and theoretical absorption spectra in gas phase (**b**)

Theoretical absorption spectra and HOMO and LUMO plots revealed that the absorption bands located around 300 nm can be attributed to the transitions from HOMO to LUMO+2 which are associated with local electronic transitions in the triphenylamine fragments. The absorption band around 350 nm are due to transitions from HOMO-1 or HOMO to LUMO, basically corresponding to a transition from a mixture of extended TPA-ethenyl π-electron orbitals toward the orbital of the ethenyl fragment. Molecular orbitals of the main transitions are shown in **Figure 36**.

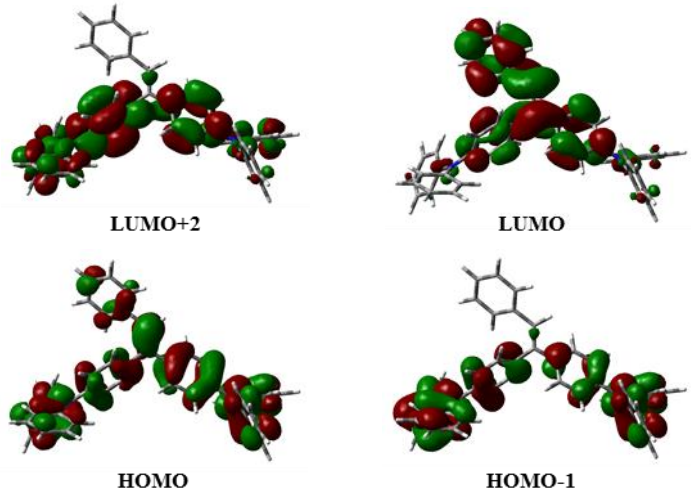

Figure 36. Molecular orbitals of compound **24** of the main electron transitions ((B3LYP/6-31G(d,p) level)

The maxima of the lowest energy absorption bands of compounds **25**-**28** having electron-donating methyl or methoxy substituents are slightly red shifted with respect of that of compound **24** without substituents, which is basically due to the σ and π donor effect in the order H < CH_3 < OCH_3.

Compounds **24**-**28** exhibit absorption bands in the wavelength range from 200 nm to 425 nm, the corresponding wavelengths are collected in **Table 16**.

Table 16. Optical properties of compounds **24-28**

Compound	Electron transition	λ [a], nm	*f*	Main transition configuration	λ_{ab} [b], nm	λ_{fl} [c], nm
24	$S_0 \rightarrow S_1$	375	0.3437	H→L (97%)	344	445
	$S_0 \rightarrow S_2$		0.3903	H-1→L (96%)		
	$S_0 \rightarrow S_5$	306	0.3815	H→L+2 (94%)	301	
25	$S_0 \rightarrow S_1$	399	0.3469	H→L (95%)	355	495
	$S_0 \rightarrow S_2$		0.4130	H-1→L (95%)		
	$S_0 \rightarrow S_5$	310	0.4621	H→L+2 (88%)	295	
26	$S_0 \rightarrow S_1$	393	0.5242	H→L (99%)	352	482
	$S_0 \rightarrow S_2$		0.3735	H-1→L (98%)		
	$S_0 \rightarrow S_5$	315	0.4239	H→L+2 (90%)	298	
27	$S_0 \rightarrow S_1$	392	0.3978	H→L (98%)	350	466
	$S_0 \rightarrow S_2$		0.3829	H-1→L (97%)		
	$S_0 \rightarrow S_5$	312	0.4321	H→L+2 (91%)	301	
28	$S_0 \rightarrow S_1$	390	0.4930	H→L (99%)	348	461
	$S_0 \rightarrow S_2$		0.3666	H-1→L (98%)		
	$S_0 \rightarrow S_5$	313	0.4146	H→L+2 (90%)	302	

[a] theoretical bands of absorption (gas phase); [b] experimental bands of absorption; [c] experimental maximum band of fluorescence emission (λ_{ex} = 310 nm)

Compounds **25-28** exhibit blue fluorescence with fluorescence emission intensity maxima being in the range from 461 nm to 495 nm, while compound **24** show the emission maximum at 445 nm.

4.4.3. Electrochemical and photoelectrical properties

The electrochemical and photoelectrical characteristics of compounds **24-28** are presented in **Table 17**.

Table 17. Values of electron affinity, HOMO/LUMO energies and ionization potentials of compounds **24-28**

Compound	IP_{CV} [a], eV	EA_{CV} [a], eV	HOMO [c], eV	LUMO [c], eV	IP_{PE} [b], eV	IP [c], eV
24	5.19	2.11	-4.85	-1.25	5.56	5.68
25	4.98	1.99	-4.52	-1.05	5.25	5.33
26	4.96	1.95	-4.43	-0.91	5.23	5.22
27	5.10	2.07	-4.70	-1.16	5.40	5.53
28	5.08	2.04	-4.66	-1.12	5.35	5.35

[a] determined by cyclic voltamperometry; [b] measured by photoemission in air method; [c] calculated theoretical at B3LYP/6-31G(d,p) level

The cyclic voltamperograms of **24**, **26** and **28** are shown in **Figure 37**. The IP_{CV} values of **24-28** were calculated from the onset potentials after calibration of the measurements against ferrocene. The onset values were estimated from the first

oxidation event by taking the intersection between the baseline and the tangent line drawn to the increasing part of the current.

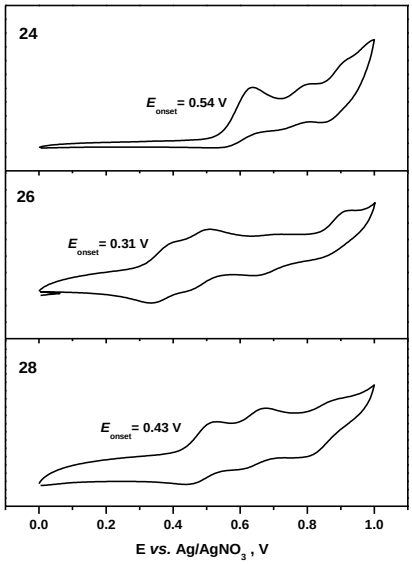

Figure 36. Cyclic voltammograms of compounds **24**, **26** and **28**

The IP_{CV} values range in a very small window of 4.96-5.19 eV. Incorporation of methoxy and methyl groups in to the structures of triphenylamine-twin compounds leads to a decrease of IP_{CV}. The EA_{CV} were obtained from the IP_{CV} values and the optical band gaps, which were deduced from the edges of the absorption spectra. The EA_{CV} values of **24-28** were found to be in the range from 1.95 eV to 2.11 eV.

The IP_{PE} of the amorphous films of compounds were found to spread over a larger range (5.23 to 5.56 eV) as compared to the IP_{CV} values. The difference between IP_{CV} and IP_{PE} values is apparently due to the different polarisation due to different environments in dilute solutions and solid layers of the compounds. However, IP_{PE}, IP_{CV}, and the theoretical IP values **(Table 17)** provide similar trends, which is consistent with the trend of the HOMO energies. This trend can be explained by the σ and π donor effect of methyl and methoxy groups, respectively. The donor effect of methyl and methoxy groups increases with the number of substituents in the molecules, explaining the increasing HOMO energy from **25** to **26** and from **27** to **28**.

4.4.4. Hole-transport properties

The room temperature electric field dependencies of hole drift mobility for the layers of compounds **24-28** are presented in **Figure 38**. Compounds **27** and **28** having methyl substituents exhibited better charge-transporting properties than the corresponding derivatives **25** and **26** having methoxy substituents. Non-substituted

compound **24** shows lowest hole mobility as compared to the substituted compounds. Hole drift mobility of ca. $1.5 \cdot 10^{-2}$ cm^2/Vs were recorded in the layers of **27** and **28** at an electric field of $3.6 \cdot 10^5$ V/cm, which are very high values as for disordered organic materials.

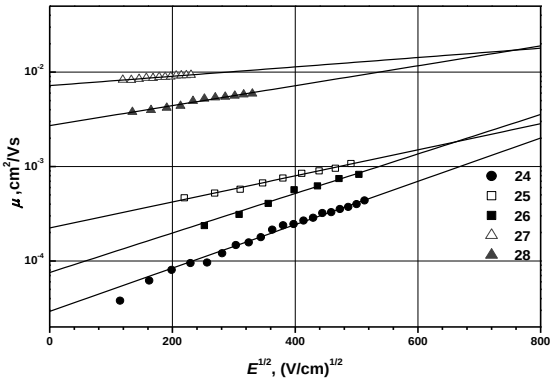

Figure 38. Electric field dependencies of hole drift mobility in the layers of compounds **24-28**

In order to obtain some insight on the factors influencing the hole mobility in these compounds, intramolecular reorganization energies (λ_i) for the isolated molecules were calculated according equation [174]:

$$\lambda_i = \left(E_M^{geom(M^+)} - E_M^{geom(M)}\right) + \left(E_{M^+}^{geom(M)} - E_{M^+}^{geom(M^+)}\right); \quad (11)$$

In this equation the quantity $E_M^{geom(M^+)}$ for instance corresponds to the energy of neutral molecule (M) in the geometry of the cationic species (M^+). Additionally, six model dimers were optimized for each of compounds **24-28** using ωB97X-D/6-31G(d,p) level, global view of optimized geometry of selected model dimers corresponding to compound **24** is presented in **Figure 39a,b**.

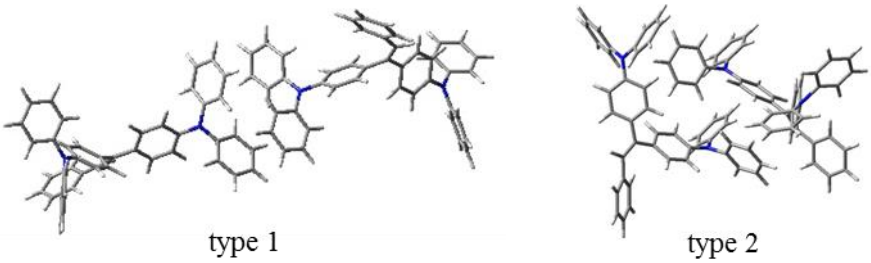

Figure 39a. Global view of model dimers (types 1 and 2) of compound **24** calculated at ωB97X-D/6-31G(d,p) level

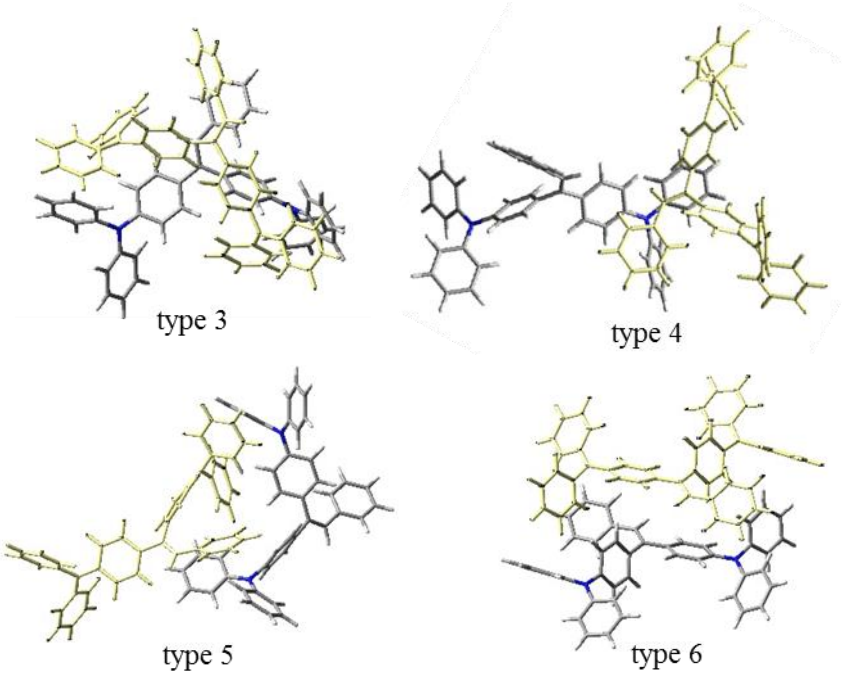

Figure 39b. Global view of model dimers (types 3-6) of compound **24** calculated at ωB97X-D/6-31G(d,p) level

The HOMO-HOMO electronic couplings (*t*) of the dimers were calculated. The results of calculations of compounds **24-28** and their dimers are presented in **Table 18**.

Table 18. Hole mobilities, intramolecular reorganization energies, HOMO-HOMO electronic couplings, dipole moments, energetic disorder parameter, dipole components and van der Waals components of compounds **24-28**

Compound	μ [a], cm^2/Vs	λ_i, eV	t [b], eV	p, D	σ, eV	σ_{dip}, eV	σ_{vdW}, eV
24	$7\cdot10^{-4}$	0.201	0.012	0.8	0.145	0.025	0.143
25	$1.7\cdot10^{-3}$	0.129	0.014	0.8-3.8	0.133	0.083	0.104
26	$1.4\cdot10^{-3}$	0.184	0.015	1.1-3.3	0.133	0.067	0.115
27	$1.5\cdot10^{-2}$	0.145	0.004	1.4	0.087	0.040	0.077
28	$1.2\cdot10^{-2}$	0.172	0.010	1.3	0.11	0.037	0.104

[a] TOF hole mobilities at $3.6\cdot10^5$ V/cm; [b] average values, calculated over six different dimer types for each compound.

Globally, the λ_i and the average t for compounds **24-28** range in small windows (0.13-0.20 eV and 0.005-0.015 eV respectively), thus suggesting small variations in hole mobility across the series. However, several discrepancies can be observed. Indeed the best hole transporting compound **27** presents the lowest

electronic coupling values, whereas the best combination of the lowest λ_i and almost the highest electronic coupling corresponds to compound **25** (0.129 eV and 0.014 eV respectively), for which a smaller hole mobility by one order of magnitude as compared to **27** is measured. Additionally, significant differences between these compounds concern the correlation of hole mobilities with the dipole moments. The increase in dipole moments by roughly 3 D between **24** and **25**,**26** suggests important decreasing hole mobilities in the same order, which is in opposite agreement with the experimental observations.

Results suggest that the differences in the hole mobilities of compounds **24**-**28** are dominated by disorder phenomena. In terms of disorder models, the increasing width of the energetic-disorder distribution (σ) of the states involved in the charge-transport impacts negatively the charge mobility. The energetic disorder parameter (σ) was deduced within the Gaussian disorder model, according to the following equation [175]:

$$\mu = \mu_0 \exp\left[-\left(\frac{2\hat{\sigma}}{3}\right)^2\right] \exp\left[C(\hat{\sigma}^2 - \sum^2)E^{1/2}\right]; \quad (12)$$

Here, σ - the energy width of the hopping site manifold, Σ - the positional disorder, C - constant, and $\hat{\sigma} = \sigma/kT$. At first electric field dependencies of the mobility for the layers of compounds **24**-**28** at different temperatures were measured. Then temperature dependencies of the zero-field mobility were plotted semilogarithmically versus $(1000/T)^2$ (**Figure 40a**). The values of $\hat{\sigma}$ were determined from the slope of a plot of log $\mu_{(E=0)}$ versus T^{-2}. **Figure 40b** shows the field dependence of the mobility at the different temperatures. The results were plotted as $\beta = d \ln \mu / dE^{0.5}$ versus $\hat{\sigma}^2$. The values of ∑ and C were determined from the slope and intercept of a plot of β versus $\hat{\sigma}^2$.

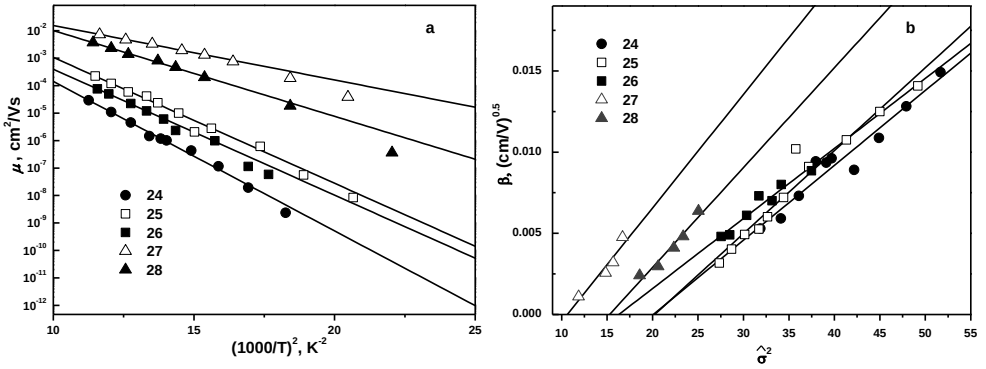

Figure 40. The logarithm of the zero-field mobility in the layers of compounds **24**-**28** versus $(1000/T)^2$ (**a**) and the field dependence of the mobility in the layers of compounds **24**-**28** at different temperatures (**b**)

The values of the energetic disorder parameter decrease significantly from 0.145 eV to 0.087 eV in the order **24** > **25** = **26** > **28** > **27**, which is consistent with

the increasing of hole mobilities in the same order (**24** < **25** < **26** < **28** < **27)**. The hole transport properties of compounds **24-28** are dominated by disorder phenomena, exhibiting decreasing energetic disorder parameter σ upon substitutions in the order H > OCH_3 > CH_3. Based on disorder models [176], the increasing width of the energetic disorder distribution (σ) of the states involved in the charge-transport impacts negatively the charge mobility. Following Borsenberger et al. [177] σ was expressed as sum of two contributions:

$$\sigma^2 = \sigma_{dip}^2 + \sigma_{vdW}^2; \quad (13)$$

The first term σ_{dip} is related to the fluctuations in electrostatic potential due to charge-dipole interactions, and is proportional to the dipole moment of the molecules. The second term σ_{vdW}, called the van der Waals term, is related to fluctuations of the electrostatic potential stemming from charge-induced dipole interactions and other permanent- and/or induced dipole-dipole interactions. In order to get some insight, the contributions for synthesized compounds **24-28** were calculated. The σ_{dip} values were evaluated by using Dieckmann's [178] and Yang's [179] relation:

$$\sigma_{dip} = \frac{k_0 c^n p}{d^2 \varepsilon} \quad (14)$$

Where c - the fraction of lattice sites occupied by the molecules (1 in the case of our pure film compounds), p - the dipole moment, d - the distance between two charge-transport molecules (Å), ε - the relative dielectric constant. Values of k_0 =3.06 and n =2/3 were used in estimations. Meanwhile, the σ_{vdW} values were deduced from **Equation 13**. The absolute values of σ, σ_{dip} and σ_{vdW} across the series of compounds **24-28** are given in **Table 18**. The values of σ_{dip} principally depend on the dipole moments of compounds. The dipole moments increase importantly upon substitution (by up to 2-3 D) in the order H < CH_3 < OCH_3. However, the contribution of σ_{dip} to the total σ is found to be of minor importance, because values of σ_{dip} are lower comparing that with σ_{vdW}. The σ_{vdW} is the dominant contribution to the total σ of compounds **24-28** and both σ and σ_{vdW} decrease upon methyl or methoxy substitutions.

4.4.5. Hole-mobility improved by hydrogen bonds

In order to understand the factors influencing σ, the interaction energies (*IE*) of dimers of compounds **24-28** were calculated (**Table 18**). It was determined that intermolecular interactions are strengthened upon methoxy and methyl substitutions from 15.4 kcal/mol of *IE* for compound **24** to 17.6-20.4 kcal/mol of *IE* for **25-28**. The increasing *IE* in the order **24** < **27** < **28** < **25** < **26** are due to additional -CH$\cdots\pi$, O hydrogen bonds (H-bonds) established by methoxy and methyl groups (**Figure 41**). The trend in *IE* across the series is explained by the stronger H-bonds established by the methoxy groups as compared to the methyl ones and by number of H-bonded groups (three groups for **26** and **28**, versus two for **25** and **27**).

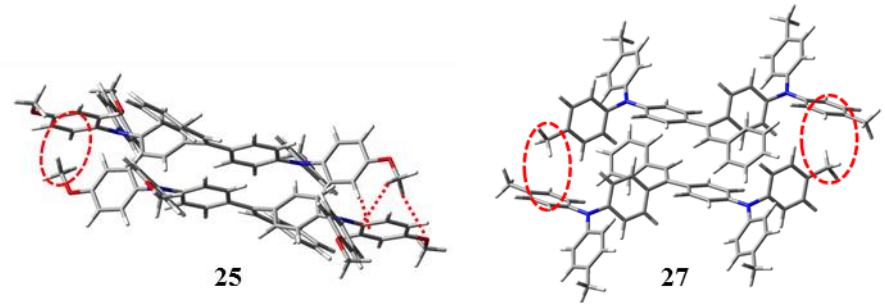

Figure 41. H-bonds established by means of methoxy and methyl and groups in compounds **25** and **27** are highlighted by dashed circles (ωB97X-D 6-31G(d,p) level)

A deeper insight into the nature of intermolecular interactions in the compounds **24-28** was made to understand impact of methoxy and methyl groups to the *IE*. We focus on geometrical randomness at the molecular level only, which is in direct correlation to *IE*. In case of non-rigid molecules containing rotating substituents, random packing patterns in amorphous films induce variations in molecular geometry that enlarge the distribution of the HOMO energies, subsequently increasing the width of the density of states (DOS). [180] Twelve HOMO energy values for compounds **24-28** were obtained by calculating the HOMO energy of each isolated fragment at the geometry of the six dimer types. The width of the HOMO energies ($\Delta\varepsilon_{HOMO\text{-}geom}$) for each compound was estimated by calculating differences between largest and smallest HOMO energies (**Table 19**). The calculated $\Delta\varepsilon_{HOMO\text{-}geom}$ values are found to decrease in the order **24** (0.247 eV) > **28** (0.153 eV) > **27** (0.138 eV) > **26** (0.124 eV) > **25** (0.093 eV). The decreasing width of the HOMO energy in the order H > CH_3 > OCH_3 correlate with the increasing values of *IE* in the same order. It can be concluded that the establishment of H-bonds by means of methoxy and methyl groups decrease the geometrical randomness and energetic distribution at the same time.

Table 19. Interaction energies, width of HOMO energies and static isotropic polarizabilities of compounds **24-28**

Compound	*IE* , kcal/mol	$\Delta\varepsilon_{HOMO\text{-}geom}$, eV	$\Delta\varepsilon_{HOMO}$, eV	α, bohr^3
24	15.4	0.247	0.241	506
25	18.9	0.093	0.185	587
26	20.4	0.124	0.182	610
27	17.6	0.138	0.153	566
28	19.0	0.153	0.161	582

Next the width of HOMO energies ($\Delta\varepsilon_{HOMO}$) of compounds **24-28** was calculated for each fragment at the dimers geometry in the presence of second fragment. This means that, with respect to the influence of *IE* factor on the geometrical randomness, the influence of polarization due to the presence of second

fragment was added. In the balance between attractive and repulsive terms impacting the HOMO energy, the attractive interactions seem to dominate in the case of compounds **25** and **26**, very probably due to the large dipole moments up to 3.8 D and 3.3 D, respectively. In the case of compounds **24**, **27** and **28**, these interactions roughly cancel out (dipole moments range from 0.8 D to 1.4 D), and become slightly repulsive. The $\Delta\varepsilon_{HOMO}$ calculated by taking into account both geometrical randomness and polarization effects varies in the order **24** (0.241 eV) > **25** (0.185 eV) > **26** (0.182 eV) > **28** (0.161 eV) > **27** (0.153 eV). Interestingly, the calculated $\Delta\varepsilon_{HOMO}$ values have a quite similar trend of the experimental σ values (**24** > **25** ~ **26** > **28** > **27**), comforting the pertinence of this model.

Additional factors may influence larger width of DOS of methoxy versus methyl substituted compounds. Conformational freedom of the methoxy groups around the C-O bonds increases number of molecular conformations. Previously, different degrees of conformational freedom in polymer chains have been found to explain differences in their σ. [181] Furthermore, larger propensity to polarization of electronic clouds of the methoxy substituted compounds as compared to the methyl ones give rise to a larger distribution of site energies, hence larger σ values. To check this effect the static isotropic polarizabilities (α) of compounds were calculated (**Table 19**). The results indicate increasing molecular polarizabilities in the order **24** < **27** < **28** < **25** < **26**.

The *IE* between adjacent molecules, presence of dipole moments, conformational degree of freedom, and molecular polarizability are in competition. The smaller σ and σ_{vdW} values of compounds **25**-**28** as compared to **24** suggest that, in the balance between these four contributions, the *IE* factor is dominant. Methoxy and methyl groups in compound **24** decrease geometrical disorder between molecules due to the potential of these groups to establish efficient H-bonds. Formation of H-bonds improve hole mobility of the substituted compounds **25**-**28** as compared to the non-substituted one **24**.

5. CONCLUSIONS

1. Carbazole derivatives with cyano moieties were synthesized and characterized as dyes for dye sensitized solar cells. It was determined that:

1.1. The extension of π-linker between carbazole fragment and cyano units lowers ionization potential of dyes and improves their light-harvesting ability.

1.2. Dyes, having additional methine unit in the π-linker, have faster intermolecular charge transfer rates than compounds with shorter π-linker.

1.3. Dye with one carbazole unit and extended π-linker is more suitable for dye sensitized solar cells than the other synthesized dyes.

2. Triphenylamine-based hydrazones were analysed as hole transporting materials and one compound was tested in the structure of dye sensitized solar cells. It was established that:

2.1. The synthesized compounds exhibit high thermal stability and form glasses with glass transition temperatures ranging from 32 °C to 56 °C.

2.2. Hydrazone with 1-methyl-4-vinylbenzene unit can be subjected to self-polymerization.

2.3. Triphenylamine-based hydrazones exhibit hole-transporting properties. The best hole drift mobility, exceeding $2.2 \cdot 10^{-3}$ cm^2/Vs at an electric field of $6.4 \cdot 10^5$ cm^2/Vs, was observed for the film of compound having 1-methyl-4-vinylbenzene substituent.

2.4. Hydrazone having methyl-phenyl substituent was used as hole transporting material for preparation of dye sensitized cells by melt process. The highest power conversion efficiency of device reached 0.075 %.

3. Carbazole derivatives with imidazole units were synthesized and characterized. It was determined that:

3.1. The synthesized compounds exhibit high thermal stability reaching 399-487 °C and glass transition temperatures ranging from 134 °C to 172 °C which are required for host materials to improve characteristics of the device.

3.2. Carbazole-imidazole derivatives have clearly localized frontier orbitals because of the structural distortion between carbazole and imidazole moieties.

3.3. The triplet energies of compounds range from 3.05 eV to 3.18 eV.

3.4. The layers of the derivatives demonstrate hole drift mobilities ranging from 10^{-6} cm^2/Vs to 10^{-3} cm^2/Vs at moderate electric fields.

3.5. Compound having two imidazole fragments and *tert*-butyl groups show bipolar charge transport. The electron mobility in the layer of this compound reaches 10^{-4} cm^2/Vs.

3.6. The compounds were used as host materials for fabrication of phosphorescent light emitting diodes. The best device exhibited the quantum efficiency of 8.3 %.

4. Triphenylamine-twin compounds were synthesized and investigated as hole transporting materials. It was established that:

4.1. Compounds exhibit high thermal stability and form glasses with glass transition temperatures ranging from 71 °C to 77 °C.

4.2. The σ and π donor effect of methyl and methoxy groups respectively, reduces the values of ionization potentials of triphenylamine-twin compounds.

4.3. Triphenylamine derivatives containing methyl groups demonstrate high hole mobilities, exceeding 10^{-2} cm^2/Vs.

4.4. Methoxy and methyl groups in the amorphous layers of compounds decrease the energetic disorder parameter due to the potential of these groups to establish efficient H-bonds.

4.5. With the decrease of the value the energetic disorder parameter of triphenylamine-twin compounds, their hole mobilities are increasing.

6. REFERENCES

1. STROHRIEGL, P., and GRAZULEVICIUS, J.V. Charge-transporting molecular glasses. *Advanced Materials*. 2002, 14(20), 1439-1452, ISSN 1521-4095.

2. COROPCEANU, V., and et al. Charge transport in organic semiconductors. *Chemical Reviews*. 2007, 107(4), 926-952, ISSN 0009-2665.

3. SHIROTA, Y., and KAGEYAMA, H. Charge carrier transporting molecular materials and their applications in devices. *Chemical Reviews*. 2007, 107(4), 953-1010, ISSN 0009-2665.

4. WEISS, D.S., and ABKOWITZ, M. Advances in organic photoconductor technology. *Chemical Reviews*. 2010, 110(1), 479-526, ISSN 0009-2665.

5. SHIROTA, Y. Organic materials for electronic and optoelectronic devices. *Journal of Materials Chemistry*. 2000, 10(1), 1-25, ISNN 1364-5501.

6. GRAZULEVICIUS, J.V. Charge-transporting polymers and molecular glasses for optoelectronic applications. *Polymers for advanced technologies*. 2006, 17(9-10), 694-696, ISSN 1099-1581.

7. NAZEERUDDIN, M.D.K., et al. Dye-sensitized solar cells: A brief of overview. *Solar Energy*. 2011, 85(6), 1172-1178, ISSN 0038-092X.

8. GRATZEL, M. Solar energy conversion by dye-sensitized photovoltaic cells. *Inorganic Chemistry*. 2005, 44(20), 6841-6851, ISSN 0020-1669.

9. NAICHIA, Y., and PULIN, Y. Organic solar cells: Their developments and potentials. *Renewable and Sustainable Energy Reviews*. 2013, 21(), 421-431 ISSN 1364-0321.

10. KATANO. M., et al. D-π-a dye system containing cyano-benzoic acid as anchoring group for dye-sensitized solar cells. *Langmuir*. 2011, 27(23), 14248-14252, ISSN 1520-5827.

11. ZHANG, L., and COLE, J.M. Anchoring groups for dye-sensitized solar cells. *Applied Materials & Interfaces*. 2015, 7(6), 3427-3455, ISNN 1944-8244.

12. CAHEN, D., et al. Nature of photovoltaic action in dye-sensitized solar cells. *Journal of Physical Chemistry B*. 2000, 104(9), 2053-2059, ISNN 1520-6106.

13. LUO, Y., et al. Towards optimization of materials for dye-sensitized solar cells. *Advanced Materials*. 2009, 21(5), 1-5, ISSN 1521-4095.

14. GRATZEL, M. Dye-sensitized solar cells. *Journal of of Photochemistry and Photobiology C: Photochemistry Reviews*. 2003, 4(2), 145-153, ISSN 1389-5567.

15. HAGFELDT, A., et al. Dye-sensitized solar cells. *Chemical Reviews*. 2010, 110(11), 6595-6663, ISSN 0009-2665.

16. LI, W., et al. Planar amine-based dye features the rigidified O-bridged dithiophene π-spacer: A potential high-efficiency sensitizer for dye-sensitized solar cells application. *Journal of Power Sources*. 2015, 275, 207-216, ISSN 0378-7753.

17. SNAITH, H.J., et al. Efficiency enhancements in solid-state hybrid solar cells via reduced charge recombination and increased light capture. *Nano Letters*. 2007, 7(11), 3372-3376, ISSN 1530-6984.

18. WIELOPOLSKI, M., et al. Position-dependent extension of π-conjugation in D-π-A dye sensitizers and the impact on the charge-transfer properties. *Journal of Physical Chemistry C*. 2013, 17(27), 13805-13815, ISSN 1932-7447.

19. KAI, P., et al. Dye-sensitized solar cells based on quinoxaline dyes: effect of π-linker on absorption, energy levels, and photovoltaic performances. *Journal of Physical Chemistry C*. 2014, 118(30), 16552-16561, ISSN 1932-7447.

20. ZHAO, J., et al. Effect of different numbers of -CH_2- units on the performance of isoquinolinium dyes. *Applied Materials & Interfaces*. 2014, 6(6), 3907-3914, ISNN 1944-8244.

21. LUO, C., et al. Indolo[3,2,1-jk]carbazole derivatives-sensitized solar cells: effect of π-bridges on the performance of cells. *Journal of Physical Chemistry C*. 2014, 118(26), 14211-14217, ISSN 1932-7447.

22. O'ROURKE, C., and BOWLER, D.R. Adsorption of thiophene-conjugated sensitizers on TiO2 anatase (101). *Journal of Physical Chemistry C*. 2010, 114(47), 20240-20248, ISSN 1932-7447.

23. BARPUZARY, D., et al. Highly efficient One-Dimensional ZnO nanowire-based dye-sensitized solar cell using a metal-free, D−π−A type, carbazole derivative with more than 5% power conversion. *Applied Materials & Interfaces*. 2014, 6(15), 12629-12639, ISNN 1944-8244.

24. MISHRA, A., et al. Metal-free organic dyes for dye-sensitized solar cells: from structure: property relationships to design rules. *Angewandte Chemie International Edition*. 2009, 48(14), 2474-2499, ISSN 1521-3773.

25. THAVASI, V., et al. Controlled electron injection and transport at materials interfaces in the dye sensitized solar cells. *Materials Science and Engineering R*. 2009, 63(3), 81-99, ISSN 0927-796X.

26. GUPTA, K.S.V., et al. Carbazole based A-π-D-π-A dyes with double electron acceptor for dye-sensitized solar cell. *Organic Electronics*. 2014, 15(1), 266-275, ISSN 1566-1199.

27. GUDEIKA, D., et al. Structure-properties relationship of the derivatives of carbazole and 1,8-naphthalimide: effects of the substitution and the linking topology. *Dyes and Pigments*. 2015, 114, 239-252, ISSN 0143-7208.

28. KEERTHI, A., et al. Architectural influence of carbazole push-pull-pull dyes on dye sensitized solar cells. *Dyes and Pigments*. 2013, 99, 787-797, ISSN 0143-7208.

29. LI, T., et al. Novel D-π-A carbazole sensitizers with 4-phenyl-2-(thiophen-2-yl) thiazole as π-bridge for dye-sensitized solar cells. *Journal of Photochemistry and Photobiology A: Chemistry*. 2015, 303-304, 91-98, ISSN 1010-6030.

30. THOMAS, K.R.J., et al. 2,3-Disubstituted thiophene-based organic dyes for solar cells. *Chemistry of Materials*. 2008, 20(5), 1830-1840, ISSN 0897-4756.

31. HAID, S., et al. Significant improvement of dye-sensitized solar cell permormance by small structural modification in π-conjugated donor-acceptor dyes. *Advanced Functional Materials*. 2012, 22(6), 1291-1302, ISSN 1616-3028.

32. ROBERTSO, N. Optimizing dyes for dye-sensitized solar cells. *Angewandte Chemie International Edition.* 2006, 45(15), 2338-2345, ISSN 1521-3773.

33. VENKATESWARARAO, A., et al. Organic dyes containing carbazole as donor and π-linker: optical, electrochemical, and photovoltaic properties. *Applied Materials & Interfaces*. 2014, 6(4), 2528-2539, ISNN 1944-8244.

34. SU, J.Y., et al. Indolo[2,3‑b]carbazole synthesized from a double-intramolecular Buchwald−Hartwig reaction: its application for a dianchor DSSC organic dye. *Organic Letters*. 2014, 16(12), 3176-3179, ISSN 1523-7060.

35. GUPTA, K.S.V., et al. Effect of the anchoring group in the performance of carbazolephenothiazine dyads for dye-sensitized solar cells. *Dyes and Pigments.* 2015, 113, 536-545, ISNN 0143-7208.

36. MAROTTA, G., et al. Novel carbazole-phenothiazine dyads for dye-sensitized solar cells: A combined experimental and theoretical study. *Applied Materials & Interfaces*. 2013, 5(19), 9635-9647, ISNN 1944-8244.

37. TAIN, H., et al. Effect of different dye baths and dye-structures on the performance of dye-sensitized solar cells based on triphenylamine dyes. *Journal of Physical Chemistry C*. 2008, 112(29), 11023-11033, ISSN 1932-7447.

38. WIBERG, J., et al. Effect of anchoring group on electron injection and recombination dynamics in organic dye-sensitized solar cells. *Journal of Physical Chemistry C*. 2009, 113(9), 3881-3886, ISSN 1932-7447.

39. RAMKUMAR, S., et al. Synthesis of D-(π-A)$_2$ organic chromophores for dye-sensitized solar cells. *Dyes and Pigments.* 2012, 94, 503-511, ISNN 0143-7208.

40. KROEZE, J.E., et al. Alkyl chain barriers for kinetic optimization in dye-sensitized solar cells. *Journal of American Chemical Society*. 2006, 128(50), 16376-16383, ISSN 0002-7863.

41. HHUANG, J.F., et al. Novel carbazole based sensitizers for efficient dye-sensitized solar cells: Role of the hexyl chain. *Dyes and Pigments.* 2015, 114, 18-23, ISNN 0143-7208.

42. KOUMURA, N., et al. Alkyl-functionalized organic dyes for efficient molecular photovoltaics. *Journal of American Chemical Society*. 2006, 128(44), 14256-14257, ISSN 0002-7863.

43. ZAFER, C., et al. Carbazole-based organic dye sensitizers for efficient molecular photovoltaics. *Solar Energy Materials & Solar Cells*. 2010, 94, 655-651, ISSN 0927-0248.

44. KOUMURA, N., et al. Substituted carbazole dyes for efficient molecular photovoltaics: long electron lifetime and high open circuit voltage performance. *Journal of Materials Chemistry*. 2009, 19, 4829-4836, ISSN 1364-5501.

45. HE, J., et al. Organic dyes incorporating a thiophene or furan moiety for efficient dye-sensitized solar cells. *Dyes and Pigments.* 2014, 104, 75-82, ISNN 0143-7208.

46. LI, B., et al. Review of recent progress in solid-state dye-sensitized solar cells. *Solar Energy Materials and Solar Cells*. 2006, 90(5), 549-573, ISNN 0927-0248.

47. YUM, J.H., et al. Recent developments in solid-state dye-sensitized solar cells. *Chemistry and Sustainability, Energy and Materials*. 2008, 1(8-9), 699-707, ISSN 1864-564X.

48. JIANG, X., et al. Highly efficient solid-state dye-sensitized solar cells based on triphenylamine dyes. *Advanced Functional Materials*. 2011, 21(15), 2944-2952, ISSN 1616-3028.

49. WANG, M., et al. Enhanced-light-harvesting amphiphilic ruthenium dye for efficient solid-state dye-sensitized solar cells. *Advanced Functional Materials*. 2010, 20(11), 1821-1826, ISSN 1616-3028.

50. BURSCHKA, J., et al. Tris(2-(1*H*-pyrazol-1-yl)pyridine)cobalt(III) as *p*-type dopant for organic semiconductors and its application in highly efficient solid-state dye-sensitized solar cells. *Journal of American Chemical Society*. 2011, 133(45), 18042-18045, ISSN 0002-7863.

51. POPLAVSKYY, D., and NELSON. J. Nondispersive hole transport in amorphous films of methoxy-spirofluorene-arylamine organic compound. *Journal of Applied Physics*. 2003, 93(1), 341-346, ISSN 1089-7550.

52. DING, I-K., et al. Pore-filling of spiro-OMeTAD in solid-state dye sensitized solar cells: quantification, mechanism, and consequences for device performance. *Advanced Functional Materials*. 2009, 19(15), 2431–2436, ISSN 1616-3028.

53. LEIJTENS, T., et al. Hole transport materials with low glass transition temperatures and high solubility for application in solid-state dye-sensitized solar cells. *ACS Nano*. 2012, 6(2), 1455-1462, ISSN 1936-0851.

54. ABATE, A., et al. Lithium salts as "redox active" p-type dopants for organic semiconductors and their impact in solid-state dye-sensitized solar cells. *Physical Chemistry Chemical Physics*. 2013, 15(7), 2572-2579, ISSN 1463-9084.

55. YANG, L., et al. Initial light soaking treatment enables hole transport material to outperform spiro-OMeTAD in solid-state dye-sensitized solar cells. *Journal of American Chemical Society*. 2013, 135(19), 7378-7385, ISSN 0002-7863.

56. PLANELLS, M., et al. Diacetylene bridged triphenylamines as hole transport materials for solid state dye sensitized solar cells. *Journal of Materials Chemistry A*. 2013, 1, 6949-6960, ISSN 2050-7496.

57. SNAITH, H.J., et al. Charge collection and pore filling in solid-state dye-sensitized solar cells. *Nanotechnology*. 2008, 19(42), 1-12, ISSN 1361-6528.

58. SNAITH, H.J., et al. Dye-sensitized solar cells incorporating a "liquid" hole-transporting material. *Nano Letters*. 2006, 6(9), 2000-2003, ISSN 1530-6984.

59. SEPEHRIFARD, A., et al. Siliconized triarylamines as redox mediator in dye-sensitized solar cells. *Applied Materials & Interfaces*. 2012, 4(11), 6211-6215, ISNN 1944-8244.

60. ZHOU, N., et al. Cross-linkable molecular hole-transporting semiconductor for solid-state dye-sensitized solar cells. *Journal of Physical Chemistry C*. 2014, 118(30), 16967-16975, ISSN 1932-7447.

61. SUNKOOK, K., et al. Low-power flexible organic light-emitting diode display device. *Advanced Materials*. 2011, 23(31), 3511-3516, ISSN 1521-4095.

62. YOOK, K.S., and LEE, J.Y. Organic materials for deep blue phosphorescent organic light-emitting diodes. *Advanced Materials*. 2012, 24(24), 3169-3190, ISSN 1521-4095.

63. PENG, T., et al. Highly efficient phosphorescent OLEDs with host-independent and concentration-insensitive properties based on a bipolar iridium complex. *Journal of Materials Chemistry C*. 2013, 1, 2920-2926, ISSN 2050-7534.

64. TAO, Y., et al. Organic host materials for phosphorescent organic light-emitting diodes. *Chemical Society Reviews*. 2011, 40, 2943-2970, ISSN 1460-4744.

65. XIU, M.B., et al. Molecular hosts for triplet emitters in organic light-emitting diodes and the corresponding working principle. *Science China Chemistry*. 2012, 53(8), 1679-1694, ISSN 1869-1870.

66. CHASKAR, A., et al. Bipolar host materials: A chemical approach for highly efficient electrophosphorescent devices. *Advanced Materials*. 2011, 23(34), 3876-3895, ISSN 1521-4095.

67. GANTENBEIN, M., et al. New 4,4′-bis(9-carbazolyl)−biphenyl derivatives with locked carbazole−biphenyl junctions: High-triplet state energy materials. *Chemistry of Materials*. 2015, 27(5), 1772-1779, ISSN 0897-4756.

68. LI, Q., et al. Asymmetric design of bipolar host materials with novel 1,2,4-oxadiazole unit in blue phosphorescent device. *Organic Letters*. 2014, 16(6), 1622-1625, ISSN 1523-7060.

69. LIU, X.K., et al. Novel bipolar host materials based on 1,3,5-triazine derivatives for highly efficient phosphorescent OLEDs with extremely low efficiency roll-off. *Physical Chemistry Chemical Physics*. 2012, 14(41), 14255-14261, ISSN 1463-9084.

70. BAN, X., et al. Bipolar host with multielectron transport benzimidazole units for low operating voltage and high power efficiency solution- processed phosphorescent OLEDs. *Applied Materials & Interfaces*. 2015, 7(13), 7303-7314, ISNN 1944-8244.

71. TAO, Y., et al. Tuning the optoelectronic properties of carbazole/oxadiazole hybrids through linkage modes: hosts for highly efficient green electrophosphorescence. *Advanced Functional Materials*. 2010, 20(2), 304-311, ISSN 1616-3028.

72**.** JIN, J., et al. Construction of high T_g bipolar host materials with balanced electron-hole mobility based on 1,2,4-thiadiazole for phosphorescent organic light-emitting diodes. *Chemistry of Materials*. 2014, 26(7), 2388-2395, ISSN 0897-4756.

73. CHO, M.J., et al. New bipolar host materials for realizing blue phosphorescent organic light-emitting diodes with high efficiency at 1000 cd/m^2. *Applied Materials & Interfaces*. 2014, 6(22), 19808-19815, ISNN 1944-8244.

74. HUANG, J.J., et al. Novel benzimidazole derivatives as electron-transporting type host to achieve highly efficient sky-blue phosphorescent organic light-emitting diode (PHOLED) device. *Organic Letters*. 2014, 16(20), 5398-5401, ISSN 1523-7060.

75. PAN, B., et al. A simple carbazole-*N*-benzimidazole bipolar host material for highly efficient blue and single layer white phosphorescent organic light-emitting diodes. *Journal of Materials Chemistry C*. 2014, 2, 2466-2469, ISSN 2050-7534.

76. HE, J., et al. Nonconjugated carbazoles: a series of novel host materials for highly efficient blue electrophosphorescent OLEDs. *Journal of Physical Chemistry C*. 2009, 113(16), 6761-6767, ISSN 1932-7447.

77. SCHROGEL, P., et al. A series of CBP-derivatives as host materials for blue phosphorescent organic light-emitting diodes. *Journal of Materials Chemistry*. 2011, 21, 2266-2273, ISSN 1364-5501.

78. WAGNER, D., et al. Triazine based bipolar host materials for blue phosphorescent OLEDs. *Chemistry of Materials*. 2013, 25(18), 3758-3765, ISSN 0897-4756.

79. LEE, C.W., et al. High quantum efficiency blue phosphorescent organic light-emitting diodes using 6-position-modified benzofuro[2,3-b]pyridine derivative. *Applied Materials & Interfaces*. 2013, 5(6), 2169-2173, ISNN 1944-8244.

80. SUN, J., et al. Synthesis and characterization of heteroatom substituted carbazole derivatives: potential host materials for phosphorescent organic light-emitting diodes. *New Journal of Chemistry*. 2013, 37(4), 977-985, ISSN 1369-9261.

81. BARONAS, P., et al. High-triplet-energy carbazole and fluorine tetrads. *Journal of Luminescence*. 2016, 169, 256-265, ISSN 0022-2313.

82. SALMAN, S., et al. Theoretical investigation of tricarbazole derivatives as host materials for blues electrophosphorescence: effects of topology. *Chemistry of Materials*. 2011, 23(23), 5223-5230, ISSN 0897-4756.

83. TSAI, M.H., et al. 3-(9-Carbazolyl)carbazoles and 3,6-di(9-carbazolyl)carbazoles as effective host materials for efficient blue organic electrophosphorescence. *Advanced Materials*. 2007, 19(6), 862-866, ISSN 1521-4095.

84. CHEN, Y.M., et al. Carbazole–benzimidazole hybrid bipolar host materials for highly efficient green and blue phosphorescent OLEDs. *Journal of Materials Chemistry*. 2011, 21, 14971-14978, ISNN 1364-5501.

85. HUNG, W.Y., et al. A carbazole–phenylbenzimidazole hybrid bipolar universal host for high efficiency RGB and white PHOLEDs with high chromatic stability. *Journal of Materials Chemistry*. 2011, 21, 19249-19256, ISNN 1364-5501.

86. BYEON, S.Y., et al. Carbazole-carboline core as a backbone structure of high triplet energy host materials. *Dyes and Pigments*. 2015, 120, 258-264, ISNN 0143-7208.

87. JEON, O. S., and LEE, J. Y. Phosphine oxide derivatives for organic light emitting diodes. *Journal of Materials Chemistry*. 2012, 22(10), 4233-4243, ISNN 1364-5501.

88. CHEN, D., et al. Nitrogen heterocycle-containing materials for highly efficient phosphorescent OLEDs with low operating voltage. *Journal of Materials Chemistry C*. 2014, 2(48), 9565-9578, ISSN 2050-7534.

89. SU, S.J., RGB phosphorescent organic light-emitting diodes by using host materials with heterocyclic cores: Effect of nitrogen atom orientations. *Chemistry of Materials*. 2011, 23(2), 274-284, ISSN 0897-4756.

90. SU, S.J., et al. Pyridine-containing bipolar host materials for highly efficient blue phosphorescent OLEDs. 2008, 20(5), 1691-1693, ISSN 0897-4756.

91. KIM, D., et al. Design of efficient ambipolar host materials for organic blue electrophosphorescence: theoretical characterization of hosts based on carbazole derivatives. *Journal of American Chemical Society*. 2011, 133(44), 17895-17900, ISSN 0002-7863.

92. XIAO, L., et al. Recent progresses on materials for electrophosphorescent organic light-emitting devices. *Advanced Materials*. 2011, 23(8), 926-952, ISSN 1521-4095.

93. LEI, G.T., et al. Highly efficient blue electrophosphorescent devices with a novel host material. *Synthetic Metals*. 2004, 144, 249-252, ISSN 0379-6779.

94. LEE, J., et al. Investigation of double emissive layer structures on phosphorescent blue organic light-emitting diodes. *Synthetic Metals*. 2009, 159, 1460-1463, ISSN 0379-6779.

95. NEOGI, I., et al. Amorphous host materials based on Tröger's base scaffold for application in phosphorescent organic light-emitting diodes. *Applied Materials & Interfaces*. 2015, 7(5), 3298-3305, ISNN 1944-8244.

96. YOOK, K.S., et al. The relationship between the host structure and optimum doping concentration in red phosphorescent organic light-emitting diodes. *Thin Solid Films*. 2011, 519, 4342-4346, ISSN 0040-6090.

97. CHEON, Y.R., et al. Bis(1-phenyl-1*H*-benzo[d]imidazole)phenylphosphine oxide interlayer for effective hole blocking in efficient phosphorescent organic light emitting diodes based on widely used charge transporting layers. *Synthetic Metals*. 2014, 190, 39-43, ISSN 0379-6779.

98. THIERY, S., et al. 4‑Pyridyl-9,9′-spirobifluorenes as host materials for green and sky-blue phosphorescent OLEDs. *Journal of Physical Chemistry C*. 2015, 119(11), 5790-5805, ISSN 1932-7447.

99. SUH, M.C., et al. Highly efficient green phosphorescent organic light emitting diodes with simple structure. *Organic Electronics*. 2013, 14(9), 2198-2203, ISSN 1566-1199.

100. KIM, M., et al. Donor–acceptor type material as a triplet host for high efficiency white phosphorescent organic light-emitting diodes. *Synthetic Metals*. 2015, 199, 105-109, ISSN 0379-6779.

101. JUANG, F.S., et al. Performance improvement of blue phosphorescent organic light-emitting diodes by using hole-buffer structure. *Thin Solid Films*. 2011, 519, 5260-5263, ISSN 0040-6090.

102. CHEN, Y., et al. High efficiency blue phosphorescent organic light-emitting diode based on blend of hole- and electron-transporting materials as a co-host. *Applied Physics Letters*. 2012, 100(21), 213301-213304, ISSN 1077-3118.

103. LEE, J., et al. Effects of interlayers on phosphorescent blue organic light-emitting diodes. *Applied Physics Letters*. 2008, 92(20), 203305-203307, ISSN 1077-3118.

104. CHO, Y.J., et al. Cyclopenta[def]fluorene based high triplet energy hole transport material for blue phosphorescent organic light-emitting diodes. *Organic Electronics*. 2012, 13(6), 1044-1048, ISSN 1566-1199.

105. PARK, M.S., et al. Indolo acridine-based hole-transport materials for phosphorescent OLEDs with over 20% external quantum Efficiency in deep blue and green. *Chemistry of Materials*. 2011, 23(19), 4338-4343, ISSN 0897-4756.

106. KIM, M., et al. Improved power efficiency in deep blue phosphorescent organic light-emitting diodes using an acridine core based hole transport material. *Organic Electronics*. 2012, 13(7), 1245-1249, ISSN 1566-1199.

107. LEE, C.W., et al. Improved power efficiency in blue phosphorescent organic light-emitting diodes using diphenylmethyl linkage based high triplet energy hole transport materials. *Organic Electronics*. 2013, 14(1), 370-377, ISSN 1566-1199.

108. BORSENBERGER, P.M., et al. The concentration dependence of the hole mobility of 1,1-bis(di-4-tolylaminophenyl)cyclohexane doped bisphenol-A-polycarbonate. *Journal of Applied Physics*. 1992, 72, 5283-5286, ISSN 1089-7550.

109. LEE, C.W., et al. A hole transport material with *ortho*- linked terphenyl core structure for high power efficiency in blue phosphorescent organic light-emitting diodes. *Organic Electronics*. 2014, 15(2), 399-404, ISSN 1566-1199.

110. HUNG, W.Y., et al. Efficient carrier- and exciton-confining device structure that enhances blue PHOLED efficiency and reduces efficiency roll-off. *Organic Electronics*. 2011, 12(4), 575-581, ISSN 1566-1199.

111. MIYAMOTO, Y., at al. Ionization potential of organic pigment film by atmospheric photoelectron emission analysis. *Electrophotography*. 1989, 28(4), 364-370. ISSN 1880-5108.

112. OKAMOTO, S., et al. Simple measurements of quantum efficiency in orgaic electroluminescent devices. *Japanese Journal of Applied Physics*. 2001, 40(2), 783-84. ISSN 1347-4065.

113. FRISCH, M.J., et al. *Gaussian 09, Revision B.01, Gaussian Inc*. Wallingford CT, 2010.

114. KOHN, W., and SHAM, L.J. Self-consistent equations including exchange and correlation effects. *Physical Review*. 1965, 140(4A), A1133-A1138, ISSN 1536-6065.

115. LEE, C.T., et al. *Physical Review B*. Development of the Colle-Salvetti correlation-energy formulainto a functional of the electron density. 1988, 37(2), 785-789, ISSN 2469-9969.

116. BECKE, A.D. Density-functional thermochemistry. III. The role of exchange. *Journal of Chemical Physics*. 193, 98(7), 5648-5652, ISSN 1089-7690.

117. CHAI, J.D., and HEAD-GORDON, M. Long-range corrected hybrid density functionals with damped atom-atom dispersion corrections. *Physical Chemistry Chemical Physics*. 2008, 10(44), 6615-6620, ISSN 1463-9084

118. GROSS, E.K.U, and KOHN, W. Time-dependent density-functional theory. *Advances in Quantum Chemistry*. 1990, 21, 255-291.

119. BAUERNSCHMITT, R., and AHLRICHS, R. Treatment of electronic excitations within the adiabatic approximation of time dependent density functional theory. *Chemical Physics Letters*. 1996, 256, 454-464, ISSN 0009-2614.

120. CASIDA, M.E, et al. Molecular excitation energies to high-lying bound states from time-dependent density-functional response theory: characterization and correction of the time-dependent local density approximation ionization threshold. *Journal of Chemical Physics*. 1998, 108(11), 4439-4449, ISSN 1089-7690.

121. KAUPP, M., et al. Computational and spectroscopic studies of organic mixed-valence compounds: where is the charge? *Physical Chemistry Chemical Physics*. 2011, 13(38), 16973-16986, ISSN 1463-9084.

122. BOYS, S.F., and BERNARDI, F. The calculation of small molecular interactions by the differences of separate total energies. Some procedures with reduced errors. *Molecular Physics*. 1970, 19(4), 553-566, ISSN 1362-3028.

123. VALEEV, E.F., et al. Effect of electronic polarization on charge-transport parameters in molecular organic semiconductors. *Journal of American Chemical Society*. 2006, 128(30), 9882-9886, ISSN 0002-7863.

124. WU, C.S., et al. Solution-processable hole-transporting material containing fluorenyl core and triple-carbazolyl terminals: synthesis and application to enhancement of electroluminescence. *Physical Chemistry Chemical Physics*. 2013, 15(36), 15121-15127, ISSN 1463-9084.

125. HERMERSCHMIDT, F., et al. 4*H*-1,2,6-Thiadiazin-4-one-containing small molecule donors and additive effects on their performance in solution-processed organic solar cells. *Journal of Materials Chemistry C*. 2015, 3(10), 2358-2365, ISSN 2050-7534.

126. HAGBERG, D.P., et al. Molecular engineering of organic sensitizers for dye-sensitized solar cell applications. *Journal of American Chemical Society*. 2008, 130(19), 6259-6266, ISSN 0002-7863.

127. SHI, D., et al. New organic sensitizer for stable dye-sensitized solar cells with solvent-free ionic liquid electrolytes. *Journal of Physical Chemistry C*. 2008, 112(44), 17478-17485, ISSN 1932-7447.

128. BIELIAUSKAS, A., et al. Synthesis of electroactive hydrazones derived from carbazolyl-based 2-propenals for optoelectronics. *Synthetic Metals*. 2013, 179, 27-33, ISSN 0379-6779.

129. CHEN, J.P. and NATANSOHN, A. Synthesis and characterization of novel carbazole-containing soluble polyimides. *Macromolecules*. 1999, 32(10), 3171-3177, ISNN 0024-9297.

130. PLATER, M., and JACKSON, T. Polyaromatic amines. Part 3: Synthesis of poly(diarylamino)styrenes and related compounds. *Tetrahedron*. 2003, 59(25), 4673-4685, ISSN 0040-4020.

131. MICHINOBU, T., et al. Novel design of organic donor-acceptor dyes without carboxylic acid anchoring groups for dye-sensitized solar cells. *Journal of Materials Chemistry C*. 2014, 2(17), 3367-3372, ISSN 2050-7534.

132. UNGER, E.L., et al. Excitation energy dependent charge separation at hole-transporting dye/TiO_2 hetero interface. *Journal of Physical Chemistry C*. 2012, 116(40), 21148-21156, ISSN 1932-7447.

133. JONO, R., et al. Theoretical study of the surface complex between TiO_2 and TCNQ showing interfacial charge-transfer transitions. *Journal of Physical Chemistry Letters*. 2011, 2(10), 1167-1170, ISSN 1948-7185.

134. XU, W., et al. New triphenylamine-based dyes for dye-sensitized solar cells. *Journal of Physical Chemistry C*. 2008, 112(3), 874-880, ISSN 1932-7447.

135. VILSMEIER, A., and HAACK, A. Über die einwirkung von halogenphosphor auf alkyl-formanilide. Eine neue methode zur darstellung sekundärer und tertiärer *p*-alkylamino-benzaldehyde. *Berichte der deutschen chemischen Gesellschaft*. 1927, 60(1), 119-122, ISSN 0365-9496.

136. BATTISTUZZI, G., et al. An efficient palladium-catalyzed synthesis of cinnamaldehydes from acrolein diethyl acetal and aryl iodides and bromides. *Organic Letters*. 2003, 5(5), 777–780, ISSN 1523-7060.

137. ABDELWARETH, A. O., and BOLM, C. Iron(III) chloride in oxidative C-C coupling reactions. *Chemical Society Reviews*. 2009, 38, 2730-2744, ISSN 1460-4744.

138. GAO, S., et al. Multifunctional Zn(II)/Cd(II) metal complexes for tunable luminescence properties and high efficient dye-sensitized solar cells. *RSC Advances*. 2015, 5(54), 43705-43716, ISSN 2046-2069.

139. KRISHNA, A., et al. Novel hole transporting materials based on triptycene core for high efficiency mesoscopic perovsike solar cells. *Chemical Science*. 2014, 5(7), 2702-2709, ISSN 2041-6539.

140. COROPCEANU, V., et al. The role of vibronic interactions on intramolecular and intermolecular electron transfer in *p*-conjugated oligomers. *Theoretical Chemistry Accounts*. 2003, 110(2), 59-69, ISSN 1432-2234.

141. CHANG, M.H., et al. Dynamics of excited-state conformational relaxation and electronic delocalization in conjugated porphyrin oligomers. *Journal of American Chemical Society*. 2008, 130(32), 10171-10178, ISSN 0002-7863.

142. HUANG, D., et al. Access to a large stokes shift in functionalized fused coumarin derivatives by increasing the geometry relaxation upon photoexcitation: An experimental and theoretical study. *Dyes and Pigments.* 2012, 95, 732-742, ISNN 0143-7208.

143. ZHAO, G.J., et al. Photoinduced intramolecular charge transfer and S_2 fluorescence in thiophene-π-conjugated donor-acceptor systems: Experimental and TDDFT studies. *Chemistry A European Journal*. 2008, 14(23), 6935-6947, ISSN 1521-3765.

144. MARCUS, R.A. On the theory of oxidation-reduction reactions involving electron transfer. *Journal of Chemical Physics*. 1956, 24(5), 966-978, ISSN 1089-7690.

145. MARCUS, R.A. Electron transfer reactions in chemistry. Theory and experiment. *Reviews of Modern Physics*. 1993, 65(3), 599-610, ISSN 1539-0756.

146. MARCUS, R.A. and SUTIN, N. Electron transfers in chemistry and biology. *Biochimica et Biophysica Acta*. 1985, 811(3), 265-322, ISSN 0005-2728.

147. GRATZEL, M. Recent advances in sensitized mesoscopic solar cells. *Accounts of Chemical Research*. 2009, 42(11), 1788-1798, ISSN 0001-4842.

148. ZHANG, J., et al. A promising anchor group for efficient organic dye sensitized solar cells with iodine-free redox shuttles: a theoretical evaluation. *Journal of Materials Chemistry A*. 2013, 1(44), 14000-14007, ISSN 2050-7496.

149. CHUNG, I., et al. All-solid-state dye-sensitized solar cells with high efficiency. *Nature*. 2012, 485, 486-489, ISSN 0028-0836

150. OGOMI, Y., et al. $CH_3NH_3Sn_xPb_{(1-x)}I_3$ perovskite solar cells covering up to 1060 nm. *The journal of Physical Chemistry Letters*. 2014, 5(6), 1004-1011, ISSN- 1948-7185.

151. LYGAITIS, R. et al. Hole-transporting hydrazones. *Chemical Society Reviews*. 2008, 37, 770-788, ISNN 1460-4744.

152. KERUCKAS, J., et al. Influence of methoxy groups on the properties of 1,1-bis(4-aminophenyl)cyclohexane based arylamines: Experimental and theoretical approach. *Journal of Materials Chemistry*. 2012, 22(7), 3015-3027, ISSN 1364-5501.

153. GAUTIER, S., and FRECHET, J.M.J. Phase-transfer catalysis in the Ullmann synthesis of substituted triphenylamines. *Synthesis*. 1987, 4, 383-385, ISSN 0039-7881.

154. HUANG, F., et al. Crosslinkable hole-transporting materials for solution processed polymer light-emitting diodes. *Journal of Materials Chemistry*. 2008, 18(38), 4495-4509, ISNN 1364-5501.

155. REVA, I., et al. Vibrational spectrum and molecular structure of triphenylamine monomer: A combined matrix-isolation FTIR and theoretical study. *Physical Chemistry Chemical Physics*. 2003, 5(18), 3844-3850, ISSN 1463-9084.

156. WANG, B.C., et al. Electronic structure and molecular orbital study of hole-transport material triphenylamine derivatives. *Journal of Luminescence*. 2007, 124, 333-342, ISSN 0022-2313.

157. CHIU, K.Y, et al. Novel trends of electrochemical oxidation of amino-substituted triphenylamine derivatives. *Journal of Electroanalytical Chemistry*. 2005, 575(1), 95-101, ISSN 1572-6657.

158 . YEH, S.J., et al. Electrochemical characterization of small organic hole-transport molecules based on the triphenylamine unit. *Electrochemistry Communications*. 2003, 5(5), 373-377, ISSN 1388-2481.

159. FREDIN, K., et al. Using a molten organic conducting material to infiltrate a nanoporous semiconductor film and its use in solid-state dye-sensitized solar cells. *Synthetic Metals*. 2009, 159, 166–170, ISSN 0379-6779.

160. KROEZE, J.E., et al. Parameters influencing charge separation in solid-state dye-sensitized solar cells using novel hole conductors. *Advanced Functional Materials*. 2006, 16(14), 1832-1838, ISSN 1616-3028.

161.ZHANG, J., et al. Energy barrier at the N719-dye/$CsSnI_3$ interface for photogenerated holes in dye-sensitized solar cells. *Scientific reports*. 2014, 4(6954), 1-6, ISSN 2045-2322.

162. MOSER, J.E. et al. Comment on "Measurement of ultrafast photoinduced electron transfer from chemically anchored Ru-dye molecules into empty electronic states in a colloidal anatase TiO_2 film". *Journal of Physical Chemistry B*. 1998, 102(18), 3649-3650, ISSN 1520-6106.

163. TACHIBANA, Y., et al. Subpicosecond interfacial charge separation in dye-sensitized nanocrystalline titanium dioxide films. *Journal Physical Chemistry*. 1996, 100(51), 20056-20062, ISSN 1089-5639.

164. REDMOND, G., and FITZMAIRICE, D. Spectroscopic determination of ftatband potentials for polycrystalline titania electrodes in nonaqueous solvents. *Journal Physical Chemistry*. 1993, 97(7), 1426-1430, ISSN 1089-5639.

165. HUNG, W.Y., et al. A new benzimidazole/carbazole hybrid bipolar material for highly efficient deep-blue electrofluorescence, yellow-green electrophosphorescence, and two-color-based white OLEDs. *Journal of Materials Chemistry*. 2010, 20(45), 10113-10119, ISNN 1364-5501.

166. BAN, X., et al. Bipolar host with multielectron transport benzimidazole units for low operating voltage and high power efficiency solution-processed phosphorescent OLEDs. *Applied Materials & Interfaces*. 2015, 7(13), 7303-7314, ISNN 1944-8244.

167. TSAI, M.H., et al. Triphenylsilyl- and trityl-substituted carbazole-based host materials for blue electrophosphorescence. *Applied Materials & Interfaces*. 2009, 1(3), 567-574, ISNN 1944-8244.

168. GU, X., et al. Bipolar host molecules for efficient electrophosphorescence: a quantum chemical design. *Journal of Physical Chemistry A*. 2010, 114(2), 965-972, ISSN 1520-5215.

169. HECKMANN, A., and LAMBERT, C. Organic mixed-valence compounds: a playground for electrons and holes. *Angewandte Chemie International Edition.* 2012, 51(2), 326-392, ISSN 1521-3773.

170. MARTIN, R. L. *Natural transition orbitals*. *Journal of Chemical Physics*. 2003, 118(11), 4775-4777, ISSN 1089-7690.

171. MALINAUSKAS, T., et al. Phenylethenyl-substituted triphenylamines: efficient, easily obtainable, and inexpensive hole-transporting materials. *Chemistry – A European Journal*. 2013, 19(44), 15044-15056, ISSN 1521-3765.

172. GUDEIKA, D., et al. New derivatives of triphenylamine and naphthalimide as ambipolar organic semiconductors: experimental and theoretical approach. *Dyes and Pigments*. 2014, 106, 58-70, ISNN 0143-7208.

173. NISHIO, M. The CH/π hydrogen bond in chemistry. Conformation, supermolecules, optical resolution and interactions involving carbohydrates. *Physical Chemistry Chemical Physics*. 2011, 13(31), 13873-13900, ISSN 1463-9084.

174. BREDAS, J.L., et al. Charge-transfer and energy-transfer processes in π-conjugated oligomers and polymers: a molecular picture. *Chemical Reviews*. 2004, 104(11), 4971-5004, ISSN 0009-2665.

175. BAASLER, H. Charge transport in disordered organic photoconductors a Monte Carlo simulation study. *Physica Status Solidi B - Basic Research*. 1993, 175(1), 15-56, ISSN 1521-3951.

176. BASSLER, H. Charge transport in disordered organic photoconductors a Monte Carlo simulation study. *Physica Status Solidi B*. 1993, 175(1), 15-56, ISSN 1521-3951.

177. BORSENBERGER, P.M., et al. Hole transport in tri-*p*-tolylamine doped polymers: the role of polymer dipole moment. *Chemical Physics*. 1995, 195(1-3), 435-442, ISSN 0301-0104.

178. DIECKMANN, A., et al. An assessment of the role of dipoles on the density-of-states function of disordered molecular solids. *Journal of Chemical Physics*. 1993, 99(10), 8136-8141, ISSN 1089-7690.

179. YOUNG, R.H. Dipolar lattice model of disorder in random media analytical evaluation of the Gaussian disorder model. *Philosophical Magazine B*. 1995, 72(4), 435-457, ISSN 1463-6417.

180. BORSENBERGER, P.M., and BASSLER, H. Concerning the role of dipolar disorder on charge transport in molecularly doped polymers. *Journal of Chemical Physics*. 1991, 95(7), 5327-5331, ISSN 1089-7690.

181. HOFFMANN, S.T., et al. What determines inhomogenous broadening of electronic transitions in conjugated polymers? *Journal of Chemical Physics B.* 2010, 114(51), 17037-17048, ISSN 1520-6106.

LIST OF PUBLICATIONS

Publications in the journals included into the database Web of Science (Thomson Reuters)

1. Mimaite, Viktorija; Grazulevicius, Juozas Vidas; Ostrauskaite, Jolita; Jankauskas, Vygintas. Synthesis and properties of triphenylamine-based hydrazones with reactive vinyl groups. *Dyes and Pigments*. 2012, 95(10), 47-52, ISSN 0143-7208.
2. Juozapavicius, Mindaugas; O'Regan, Brian; Anderson, Assaf Y.; Grazulevicius, Juozas Vidas; Mimaite, Viktorija. Efficient dye regeneration in solid-state dye-sensitized solar cells fabricated with melt processed hole conductors. *Organic Electronics*. 2012, 13(10), 23-30, ISSN 1566-1199.
3. Mimaite, Viktorija; Grazulevicius, Juozas Vidas; Laurinaviciute, Rasa; Volyniuk, Dmytro; Jankauskas, Vygintas; Sini, Gjergji. Can Hydrogen Bonds Improve the Hole-Mobility in Amorphous Organic Semiconductors? Experimental and Theoretical Insights. *Journal of Materials Chemistry C*. 2015, 3(44), 11660-11674, ISSN 2050-7534.

List of the presentations in the international scientific conferences

1. Mimaite, Viktorija; Grazulevicius, Juozas Vidas; Jankauskas, Vygintas. Glass-forming triphenylamine derivatives as hole transporting materials // Baltic Polymer Symposium 2013 : Trakai, Lithuania, September 18-21, 2013 : programme and abstracts / Vilnius University, Kaunas University of Technology. Vilnius : Vilnius University Publishing House, 2013, p. 95.
2. Mimaite, Viktorija; Grazulevicius, Juozas Vidas; Jankauskas, Vygintas. Triphenylamine-based semiconductors for application in optoelectronic devices // Solar energy for world peace : Istanbul, Turkey, August 17-19, 2013 / Johannes Kepler University Linz, p. 150.
3. Mimaite, Viktorija; Grazulevicius, Juozas Vidas; Ostrauskaite, Jolita; Jankauskas, Vygintas. Synthesis, characterization and self-polymerization of electro-active monomers // Baltic Polymer Symposium 2012 : Liepaja, Latvia, September 19-22 : program and abstracts. Riga : Riga Technical University, 2012. p. 69.
4. Mimaite, Viktorija; Grazulevicius, Juozas Vidas; Ostrauskaite, Jolita; Jankauskas, Vygintas. Triphenylamine-based hydrazones as organic semiconductors // International Symposium on Electronic/Optic Functional Molecules 2012 : Shanghai, China, March 11-13, 2012 / East China University of Science and Technology, p. P-31.
5. Mimaite, Viktorija; Ostrauskaite, Jolita; Grazulevicius, Juozas Vidas; Jankauskas, Vygintas. Triphenylamine-based hydrazone monomers with vinyl groups // Baltic Polymer Symposium 2011 : Pärnu, Estonia, September 21-24, 2011 : program and abstracts / Tallinn University of Technology, p. 85.

ACKNOWLEDGMENT

Prof. Juozas Vidas Gražulevičius is greatly acknowledged for the supervision of the work and opportunity to carry out the work at the Department of Polymer Chemistry and Technology.

Dr. Gjergi Sini is sincerely thanked for given knowledge in theoretical calculations and helpful discussions.

Dr. Jolita Ostrauskaitė is thanked for teaching first steps in synthesis and characterisation of the organic compounds.

Mindaugas Juozapavičius and other coworkers from Imperial College London are thanked for the fabrication of dye sensitized solar cells by melt process, investigation and study of the properties of these devices.

Dr. Dmytro Volyniuk and Dr. Vygintas Jankauskas are acknowledged for the measurements of charge carrier mobilities in the layers of synthesized compounds.

Marytė Krenevičienė and Dr. Greta Ragaitė are thanked for measurements of proton and carbon nuclear magnetic resonance.

The specialists of the Department of Polymer Chemistry and Technology are greatly thanked for optical, thermal, mass spectrometry and electroluminescence measurements.

Dr. Jūratė Simokaitienė, Rasa Laurinavičiūtė, Eglė Stanislovaitytė, Dr. Aušra Tomkevičienė and Dr. Jonas Keruckas are sincerely thanked for advices and pleasant discussions.

All the colleagues of laboratory and research group are kindly thanked for help and friendly working atmosphere.

Finally, my family is sincerely thanked for supporting me.

SL344. 2016-05-11, 13,75 leidyb. apsk. l. Tiražas 12 egz. Užsakymas 205.
Išleido Kauno technologijos universitetas, K. Donelaičio g. 73, 44249 Kaunas
Spausdino leidyklos „Technologija“ spaustuvė, Studentų g. 54, 51424 Kaunas